A STUDY OF THE DISSOCIATION REACTION $n+p \rightarrow p\pi^- + p$ FOR NEUTRON MOMENTA BETWEEN 50 GeV/c AND 300 GeV/c

by

Joseph Robert Biel

Submitted in Partial Fulfillment

of the

Requirements for the Degree

DOCTOR OF PHILOSOPHY

The University Of Rochester

Rochester, New York

February 1977

FERMILAB
LIBRARY

VITAE

The author was born in Toledo, Ohio. He attended Case Western Reserve University in Cleveland, Ohio, where he received a Bachelor of Science degree in Physics in June of 1971. He then enrolled at the University of Rochester as a graduate student in the Department of Physics and Astronomy. For the first two of his five years with the University the author was employed as a teaching assistant after which he held the position of research assistant. At present the author is employed at the Fermi National Accelerator Laboratory in Batavia, Illinois.

ACKNOWLEDGMENTS

As is the case with most high energy physics experiments, the material presented in this report represents years of effort and the participation of many individuals. I would first like to thank my collaborators on the experiment Edward Bleser, Thomas Ferbel, Dieter Freytag, Bruno Gobbi, Lawrence Kenah, Jerome Rosen, Randal Ruchti, Paul Slattery and David Underwood who, in addition to me, were principally responsible for the setup and operation of the experimental apparatus. Valuable assistance was also provided by David Chaney, Dennis Duke, Terrence Jensen, Joseph Keren, Ronald Lipton, Thomas Phillips, Howard Scott and Danny Spelbring. I wish to thank the staff of the Fermi National Accelerator Laboratory, its director Robert Wilson, and Richard Lundy and Peter Koehler, heads of the Meson Area during the setting up and execution of the experiment, for providing the resources and support required to complete our work. A great deal of computation was performed using the facilities of the computing department headed by Albert Brenner. I also wish to thank Frank Turkot for generously lending us a SAC digitizing system for testing our equipment.

I was assisted in the preparation of this thesis by Mrs. Edna Hughes who typed the manuscript and by Albert Covert, Alan Knapp and William Stinson who helped with the figures. My days as a graduate student at the University of Rochester were made more pleasant by the friendship shown to me by many other students and

university personnel. Among these I wish to express my special appreciation to Betty Cook and Brian Wormington. Finally I thank my thesis advisors, Tom Ferbel and Paul Slattery, with whom I have had the pleasure of working for my five years as a graduate student and who through their constant support have significantly contributed to the completion of this thesis.

ABSTRACT

We have studied the neutron dissociation reaction $n+p \rightarrow p\pi^- + p$ for incident neutron momenta between 50 and 300 GeV/c. Data were obtained using a wire spark chamber spectrometer located in the Meson Detector Building of the Fermi National Accelerator Laboratory. The integrated dissociation cross section was found to be nearly momentum independent over the momentum interval studied. A strong correlation was observed between the square of the four-momentum transfer (t) and the $p\pi^-$ rest mass (M), as well as between t and the $p\pi^-$ center of mass decay direction. The observed mass distribution consisted of both narrow resonance-like structure and a continuum. Moments of the decay angular distributions revealed a rich structure suggesting contributions from many partial waves. Reasonable success was achieved in explaining the data in terms of a Deck-type model.

TABLE OF CONTENTS

	Page
VITAE	ii
ACKNOWLEDGMENTS	iii
ABSTRACT	v
LIST OF TABLES	ix
LIST OF FIGURES	x
CHAPTER	
I. INTRODUCTION	1
A. General Introduction	1
B. Diffraction Dissociation	1
C. Experimental Goals	3
D. Description of Reaction	4
E. Outline	5
II. THE EXPERIMENT	7
A. Neutral Beam	7
B. Hydrogen Target	9
C. Vee Spectrometer	13
1. Counter System	13
2. Spark Chambers	14
3. Analyzing Magnet	19
4. Calorimeter	19
D. Event Trigger	21
E. Trigger Rates	22

Page

F. Data Acquisition 23

G. Summary of Data 23

III. ANALYSIS OF DATA 25

A. Reconstruction of Events 25

1. Check for Recoil Proton 25

2. Calculation of Spark Positions 25

3. Search for a Dissociation Event 26

a. Location of Tracks 26

b. Determination of the z Coordinate of the Vertex 28

c. Least Squares Fit 29

d. Elimination of Spurious Multiple Tracks 29

B. Correction for Geometric Efficiency 31

C. Corrections for Background 35

1. Calorimeter 35

2. Hydrogen Target 37

a. Recoil-Angle Distribution 37

b. Energy Loss of the Recoil Proton 38

c. Background Subtraction Using Recoil-Angle Distributions 43

d. Target-Empty Correction 48

3. Summary 48

D. Cross Section 50

1. Preliminary Normalization 50

2. Further Corrections 51

Page

a. Region of Negligible Geometric Acceptance 51

b. Events with $t < .02\ GeV^2$ 56

c. Final Cross Sections 56

IV. PRESENTATION OF RESULTS 58

A. General Features 58

B. Distributions in Momentum Transfer 60

1. Mass Dependence 60

2. Momentum Dependence 62

3. Decay Angle Dependence 67

C. Mass Distributions 73

1. Dependence on t 73

2. Decay Angle Dependence 73

3. High Mass Behavior 77

D. Decay Angle Distributions 77

V. DISCUSSION AND CONCLUSIONS 104

A. Comparison With Other Experiments 104

1. Other Results for the Reaction $n+p \rightarrow p\pi^- + p$ 104

2. Results from Other Dissociation Reactions 107

a. Final States Containing Two Nucleons and One Pion 107

b. Final States Containing Two Pions and One Nucleon 109

B. Comparison with a Model 112

C. Conclusions 120

FOOTNOTES AND REFERENCES 121

APPENDIX 125

LIST OF TABLES

		Page
I	Details of the calculation of the cross section	52
II	Final cross sections	57
III	Fits to differential cross sections	63
IV	Correction to cross sections for losses below $t = .02\ GeV^2$	65
V	Slope parameter as a function of mass and incident neutron momentum	68
VI	Mass and t intervals used in the calculation of moments	86
VIIa-f	Values of moments of the decay angular distributions	97
VIII	Summary of previous measurements of $n+p \rightarrow p\pi^- + p$ for incident momenta in excess of 5 GeV/c	105

LIST OF FIGURES

		Page
1.	(a) Definition of kinematical variables in the laboratory frame (b) Definition of Gottfried-Jackson frame (t channel) (c) Definition of helicity (s shannel helicity) frame.	6
2.	Diagram of M3 beam line at the Fermi National Accelerator Laboratory.	8
3.	Diagram of the high pressure gas target.	10
4.	Graph of the minimum value of t as a function of target pressure.	11
5.	Illustration of the scintillator arrangement inside the gas target.	12
6.	Diagram of the spark chamber spectrometer.	14
7.	Diagram of the scintillation counter system used in the experiment.	15
8.	Explanation of spark chamber magnetostrictive read out system.	17
9.	Drawing of calorimeter.	20
10.	Scatterplot of the logarithm of the ratio of the pulse heights observed at opposite ends of the recoil scintillators versus the z coordinate of the dissociation event as determined by the tracks obtained using the spark chambers.	30
11.	Histogram of weights used to correct for geometric efficiency.	33
12.	Plots of the average geometrical efficiency as a function of p, M and t.	34
13.	(a) A histogram of the calorimeter pulse heights (b) Histograms of the neutron momenta observed for events with calorimeter pulse heights less than and greater than 25.	36
14.	(a) Definition of recoil angle ϕ (b) Typical recoil-angle distribution	39
15.	(a) Momentum spectra for events with recoil angles less than and greater than 14°	40

Page

(b) Momentum spectra for events with proper and improper energy loss in the recoil scintillators.

16. Mean value of pulse heights versus t for a typical recoil scintillator for the following three conditions: 42
(a) All events
(b) Events with recoil angles less than 14°
(c) Events with recoil angles greater than 14°

17. t distributions observed for events with recoil angles between 14° and 28° for four incident neutron-momentum intervals. 45

18. Recoil-angle distribution for all events and estimate of the background. 47

19. Vertex distributions for target-full and target-empty runs. 49

20. Cross sections as a function of momentum for four mass intervals and each of the following four cases: 53
(a) All events
(b) Events with $\cos\theta_{GJ} > 0$
(c) Events with $\cos\theta_{GJ} < 0$
(d) Cross sections corrected for regions of poor geometric acceptance.

21. The two upper plots give the dependence of the cut-off momentum on mass which was used to obtain the final samples of data. The two lower graphs provide an estimate of the fraction of the beam spectrum above the cut off. The more restrictive cut offs used in the calculation of the moments are shown in (b), (a) shows the cut offs used for the less sensitive characteristics of the data. 55

22. Histograms showing the final differential cross sections obtained as a function of t, M, $\cos\theta_{GJ}$ ϕ_{GJ}, $\cos\theta_H$ and ϕ_H. 59

23. Distributions in t for eight mass regions. 61

24. Slope parameters of t distributions as a function of mass. 64

25. Slope parameters of t distributions as a function of momentum for four mass regions. 66

26. t-spectra as a function of $\cos\theta_{GJ}$ for $M < 1.35$ GeV/c^2. 69

Page

27. t-spectra as a function of $\cos\theta_{GJ}$ for 1.35 GeV/c^2 <M<1.55 GeV/c^2. 70

28. t-spectra as a function of $\cos\theta_{GJ}$ for 1.55 GeV/c^2 <M<1.8 GeV/c^2. 71

29. Slope parameters of t distributions as a function of $\cos\theta_{GJ}$ and $|\phi_{GJ}|$ for three mass regions. 72

30. Comparison of slope parameters as a function of mass between all the data and data for $|\cos\theta_{GJ}|<0.3$. 74

31. Mass histograms for six regions of t. 75

32. Mass histograms for six regions of $\cos\theta_{GJ}$. 76

33. Mass histograms for sixteen regions of $\cos\theta_{GJ}$ and $|\phi_{GJ}|$. 78

34. Mass distributions for M between 1.8 GeV/c^2 and 3.0 GeV/c^2 for all data, for $\cos\theta_{GJ} > 0$ and for $\cos\theta_{GJ} < 0$. 80

35. Distributions in $\cos\theta_{GJ}$ for two regions of t and for five regions of mass. 81

36. Distribution in ϕ_{GJ} for two regions of t and five regions of mass. 82

37. The cross section as a function of $\cos\theta_{GJ}$ and $|\phi_{GJ}|$ illustrated in both a scatterplot and a perspective drawing. 84

38. Histograms showing the deviations of the imaginary parts of the decay angular moments from zero in units of the moment error. 87

39. Plots of t channel moments as a function of mass in two regions of t. 89

40. (a)-(c) Plots of t channel moments as a function of t for six mass regions. 90

41. Plots of s-channel helicity moments as a function of mass for two t regions. 93

42. (a)-(c) Plots of s-channel helicity moments as a function of t for six mass regions. 94

Page

43. Dissociation cross section as a function of momentum. 108

44. A comparison of the momentum dependence for the dissociation of only one nucleon in the reactions: $n+p \rightarrow (p\pi^-)+p$ and $p+p \rightarrow (n\pi^+)+p$. 110

45. Feynman diagrams for the three processes used in our calculation:
(a) Pion-exchange Deck
(b) Proton-exchange Deck
(c) Direct nonresonant production (neutron pole term). 113

46. Comparison of the mass spectrum with that predicted by the model in four t regions. 114

47. Comparison of the t distributions with prediction of the model for four mass regions and three regions of $\cos\theta_{GJ}$. 115

48. Comparison of the low-order t-channel moments with predictions of the model as a function of mass for $.02<t<.12$ GeV^2. 117

49. Comparison of the smoothed correlation between $\cos\theta_{GJ}$ and $|\phi_{GJ}|$ with predictions of the model at low mass and low t. 118

CHAPTER I

INTRODUCTION

A. General Introduction

The data presented in this thesis represent a study of the neutron dissociation reaction

$$n + p \rightarrow p\pi^- + p \tag{1}$$

for incident neutron momenta between 50 and 300 GeV/c. The chief merits of this reaction are that it is a simple inelastic process with a relatively large cross section at high energy. It is hoped that the results of this experiment will provide a valuable testing ground for a theory of high energy production processes. In so doing, it will contribute to our understanding of the strong interaction.

B. Diffraction Dissociation

High energy elastic scattering is characterized by an angular distribution similar to that produced by the diffraction of light from an object and is thus referred to as diffraction scattering. Reaction (1) is one member of a class of inelastic processes which have many properties similar to those of elastic scattering and are, therefore, also referred to as 'diffractive'[1]. Such quasi-elastic

production processes, particularly at high energy, account for a large fraction of the total cross section.

Let us consider the general reaction:

$$A + B \rightarrow A^* + B$$

where A is an incident high energy particle of mass M_A, B is the target particle, and A* is an "excited" state of A having mass M_{A^*} ($M_{A^*} > M_A$). We can consider A* to be either an explicit resonant state or simply a system of final state particles into which A has dissociated.[2] To satisfy energy-momentum conservation, the target particle, B, must recoil with a certain minimum value of kinetic energy. At high energy this kinematic constraint can be approximated by the relation:

$$|t| > \left(\frac{M_{A^*}^2 - M_A^2}{2p}\right)^2$$

where p is the momentum of particle A in the laboratory and t is the squared four-momentum transfer between A and A*. Thus for fixed M_{A^*} the kinematic barrier for the transformation of A into the state A* becomes increasingly weaker as the momentum of A increases. For incident nucleons with momenta of 100 GeV/c it is possible to produce final state systems of 2 GeV/c^2 mass at $|t|$ values of the order of 10^{-4} GeV^2. From a kinematic point of view, therefore, there is very little difference between elastic scattering and the inelastic

production of several GeV/c^2 objects.

If the transformation were truly elastic-like in nature we would, moreover, expect the quantum numbers of A* to be the same as those of A. The only exception would be a possible change in the spin and parity of A caused by the transfer of momentum between the colliding objects leading to an excitation of A to A*. Consequently, the allowable final-state quantum numbers would be those resulting from the combination of the spin and parity of A with those of a term of the so called "natural"[3] spin-parity series $J^P = 0^+, 1^-, 2^+, \ldots$.

As with high energy elastic scattering, diffractive production reactions should show little momentum dependence. In general, most cross sections decrease as p^{-n} at high energy where n depends roughly upon the kind of particle that can be exchanged in the interaction.[4] For all diffractive processes the mediating particle is the Pomeranchukon ($\mathbb{P}$). The predicted value for n is thus expected to be far less than 1, compared with values of 2 or greater in the case of typical meson or baryon exchanges. At high energy there thus exists a natural selection process favoring diffractive processes and it is not surprising, therefore, that they account for a large fraction of the total cross section.

C. Experimental Goals

Since the introduction of the concept of diffraction dissociation, a great deal of experimental data has been accumulated in support of

the existence of such a production mechanism.[1] In addition to our neutron dissociation reaction, results have been obtained for many other analogous diffractive processes. A large fraction of the previous work was performed using bubble chambers. In most older bubble chamber experiments, the number of events collected tended to be quite small (of the order of thousands of events). The choice of deuterium as a source of neutrons for most of these experiments also required a model dependent correction to be made to extract the neutron component of the interaction. Furthermore, all previous experiments were performed at low energies, where significant contributions from nondiffractive reactions contaminated the Pomeranchuk-mediated processes. The goal of this experiment was, therefore, to perform a high statistics study of neutron dissociation in a previously unexplored momentum range of 50 to 300 GeV/c using a beam of free neutrons. In this region the process should be almost purely diffractive and a large data sample would allow detailed studies to be carried out.

D. Description of Reaction

Any reaction with two initial-state particles and three final-state particles, in which no spin information is measured, requires five variables for a complete description of the kinematics. Our choice for these variables will be the magnitude of the incident neutron momentum (p), the invariant mass of the dissociated $\pi^- p$ system (M), the absolute value of the squared four-momentum transfer

between the incident neutron and the exiting $\pi^- p$ system (t),[5] and the decay angles of the proton as calculated in the rest frame of the produced $\pi^- p$ system. Definitions for the first three of these variables are illustrated in Fig. 1. The two angular variables (θ and ϕ) will most often be given in the so called Gottfried-Jackson frame (t channel frame). An alternate frame, also used upon occasion, is the s-channel helicity frame, referred to for convenience as simply the "helicity" frame.

E. Outline

Chapter II discusses the experimental technique, Chapter III describes the reconstruction of particle trajectories from recorded spark chamber information. The selection of the final data sample, the weighting of each event to correct for detection inefficiencies, and the corrections for backround processes are also discussed in Chapter III. The fully processed data are presented in Chapter IV. Finally, discussion of the results and a summary of our conclusions are given in Chapter V.

(a) Laboratory frame

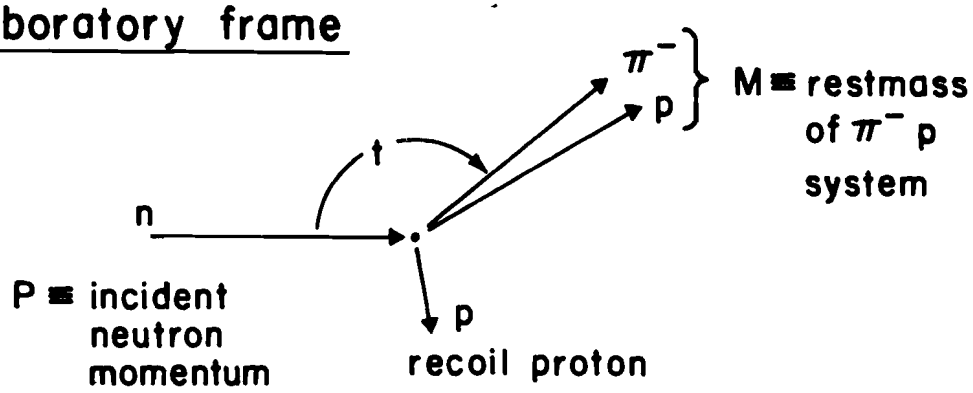

t ≡ | squared 4 momentum transfer |

(b) Gottfried – Jackson frame (t channel helicity)

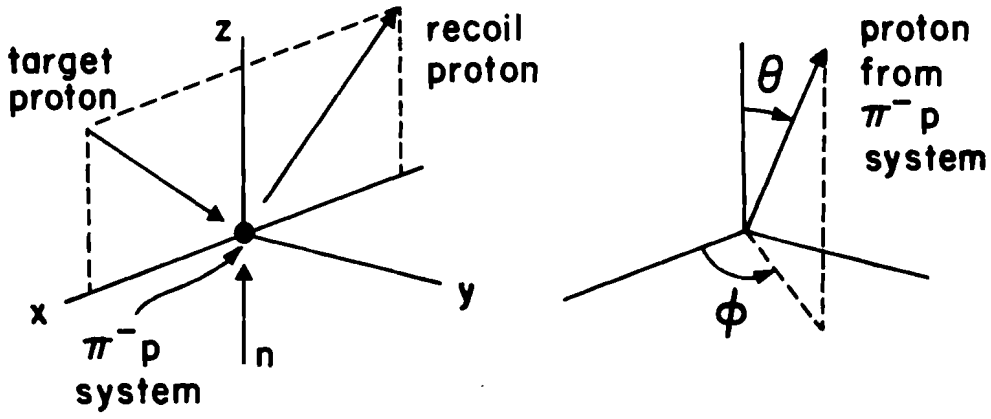

(c) Helicity (s channel helicity) frame

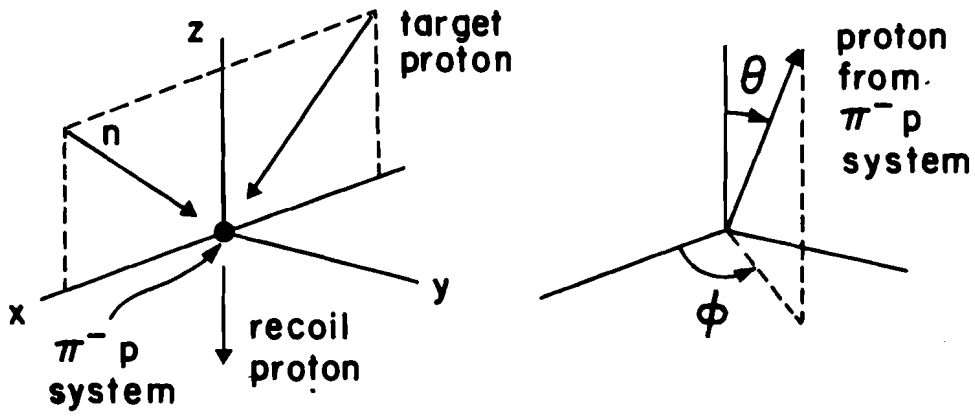

Figure 1

CHAPTER II

THE EXPERIMENT

A. Neutral Beam

The experiment was performed in the M3 beam line of the Fermilab Meson Detector Building (Fig. 2). Neutrons were produced through the interaction of 300 GeV/c primary protons in a 20 cm Be target. Secondary particles produced at approximately 1 mR were selected by collimators C_1-C_3 and the charged component of the beam was then removed with the series of magnets $Q_1D_1Q_2D_2D_3D_4$. Three radiation lengths of lead were used to convert photons in the beam into e^+e^- pairs. These were subsequently removed by collimators C_4 and C_5 after being deflected by dipole magnet D_5. At a distance of 300 meters from the production target, the collimator C_6 was used to define the final beam aperture. This collimator was equipped with a variable size insert which allowed adjustment of both size and intensity of the neutron beam. The final elements $D_6C_7C_8C_9C_{10}D_7$ removed any residual charged particles originating either at the production target or from material along the path of the beam. At the spectrometer target the beam had a radius of about 5 mm and was essentially free of halo.

M3 BEAMLINE

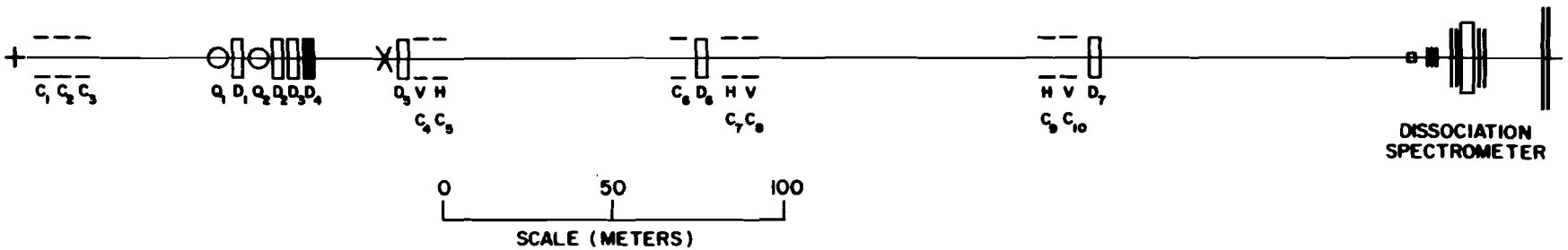

LEGEND

+ MESON PRODUCTION TARGET

= COLLIMATOR (H=> HORIZONTAL, V=> VERTICAL)

[] HORIZONTAL DIPOLE MAGNET

▮ VERTICAL DIPOLE MAGNET

O QUADRAPOLE MAGNET

X Pb γ CONVERTER

Figure 2

B. Hydrogen Target

Beam neutrons interacted with target protons contained in a high pressure hydrogen gas target (Fig. 3). This consisted of a cylindrical target region 9 cm in diameter and 50 cm long, enclosed within a pressure vessel and surrounded by a scintillation-counter system. Counters A_0 and S consisted of thin disc-shaped scintillators. A_0 was used to veto events which had charged incoming particles, and S was used to trigger on forward-going reaction products. The remaining sixteen counters (T1-T16) were 1/4" thick scintillators used to detect the recoiling target protons. Gas was chosen in place of liquid to allow measurements to be made at very small values of momentum transfer. Figure 4 shows a plot of the minimum value of t which had to be transferred in the reaction so that the recoil proton would have sufficient energy to transverse the gas region between the interaction point and trigger the recoil scintillators. Pressures of up to 3000 p.s.i. could be maintained within the target. (At this pressure hydrogen gas has approximately 20% of the density of liquid hydrogen.)

Light produced within the target scintillators was transferred via lucite light pipes and windows into phototubes positioned outside the pressure vessel. Both counters A_0 and S were monitored by two phototube systems (signals A_{OL}, A_{OR}, S_U, S_D) to insure highly reliable operation. The recoil counters were paired at both ends so as to reduce the complexity of construction of the target (Fig. 5). Counter pairs were staggered at opposite ends of the target to

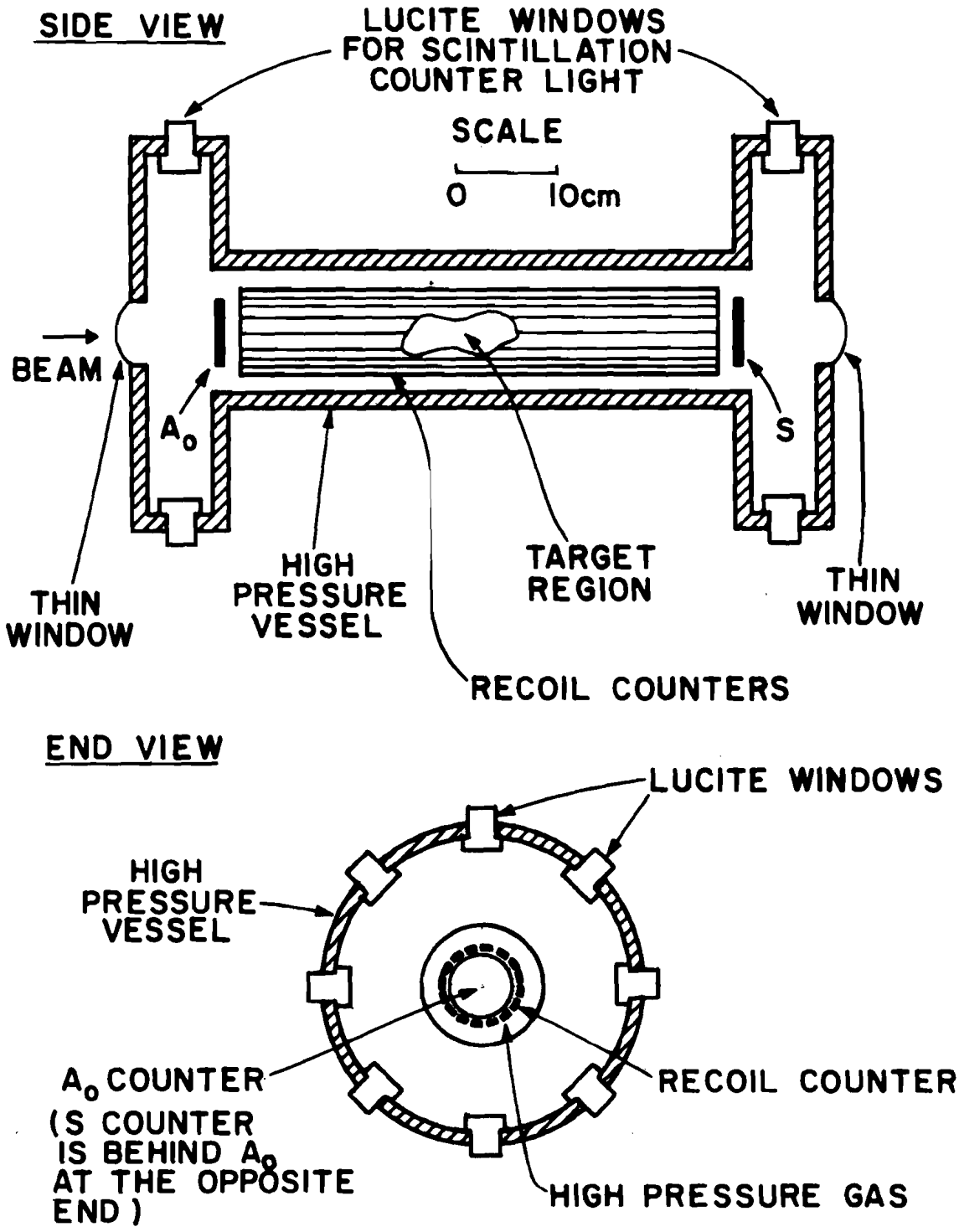
SIDE VIEW
LUCITE WINDOWS FOR SCINTILLATION COUNTER LIGHT
SCALE
0
10cm
BEAM
A_0
S
THIN WINDOW
HIGH PRESSURE VESSEL
TARGET REGION
THIN WINDOW
RECOIL COUNTERS
END VIEW
LUCITE WINDOWS
HIGH PRESSURE VESSEL
A_0 COUNTER
(S COUNTER IS BEHIND A_0 AT THE OPPOSITE END)
RECOIL COUNTER
HIGH PRESSURE GAS

Figure 3

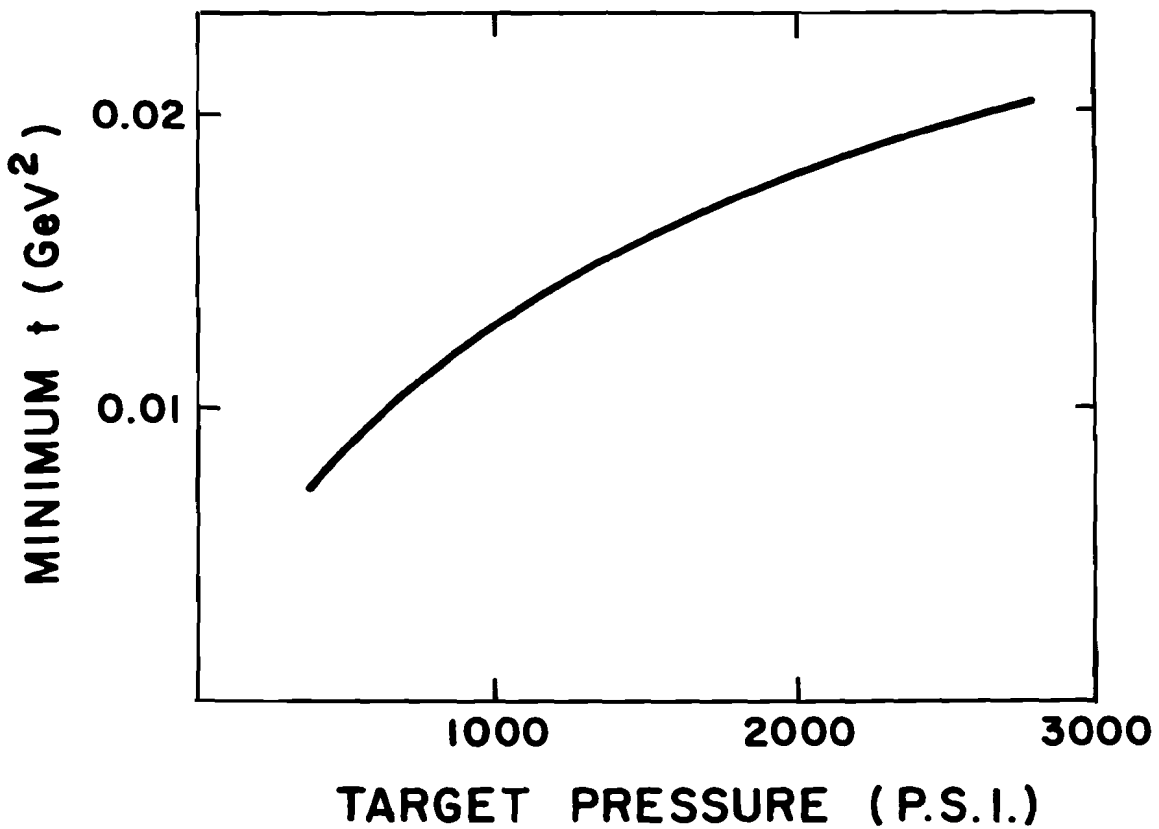

Figure 4

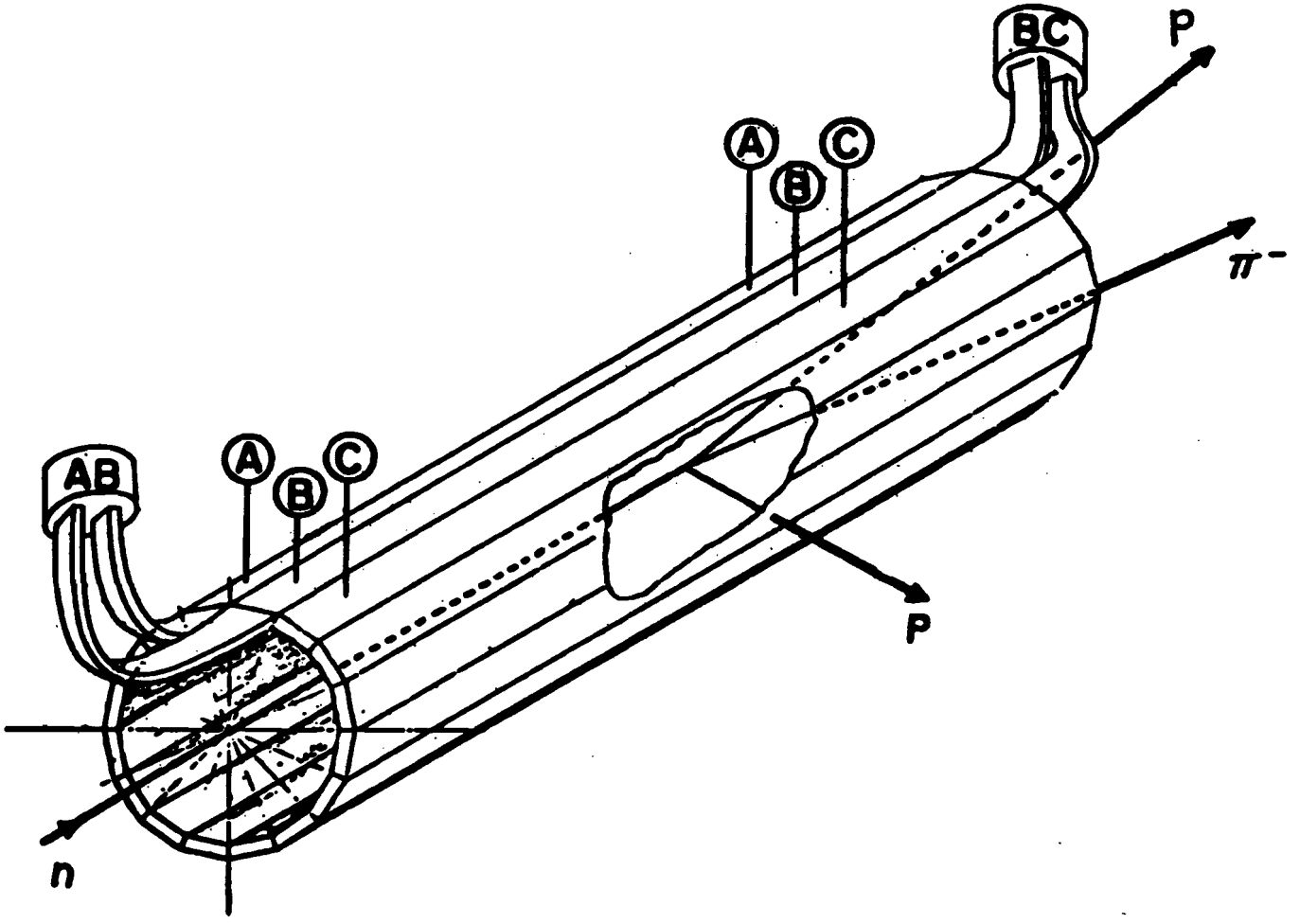

Figure 5

provide identification of the activated scintillator strip. For example, if the phototube associated with counters A and B produced a signal while a simultaneous signal was observed from the phototube for counters B and C, counter B was identified as the triggering counter. Three kinds of information were sought from the recoil counters: 1) The azimuthal direction of the recoil proton; 2) The position along the length of the target where the proton had struck the scintillator (determined from the relative pulse-heights at the two ends of the scintillator); 3) The energy deposited in the scintillator strip (determined from the combined pulse heights at the two ends of the scintillator strip).

C. Vee Spectrometer

The dissociation products of the neutron were detected using a spark-chamber spectrometer (Fig. 6). Principal components of this system were: 1) a trigger counter system, 2) a set of wire spark chambers, 3) an analyzing magnet, and 4) a small beam calorimeter.

1. Counter System

A set of scintillation counters was used to detect the occurrence of a dissociation event (Fig. 7). One array of counters, A_1-A_4, covered the front face of the spectrometer magnet to signal any particles missing the magnet aperture. These counters were positioned behind a 2 cm sheet of lead to enhance the detection of photons. Downstream of the magnet, particles passed through a six element counter hodoscope (H1). Finally, a second hodoscope of

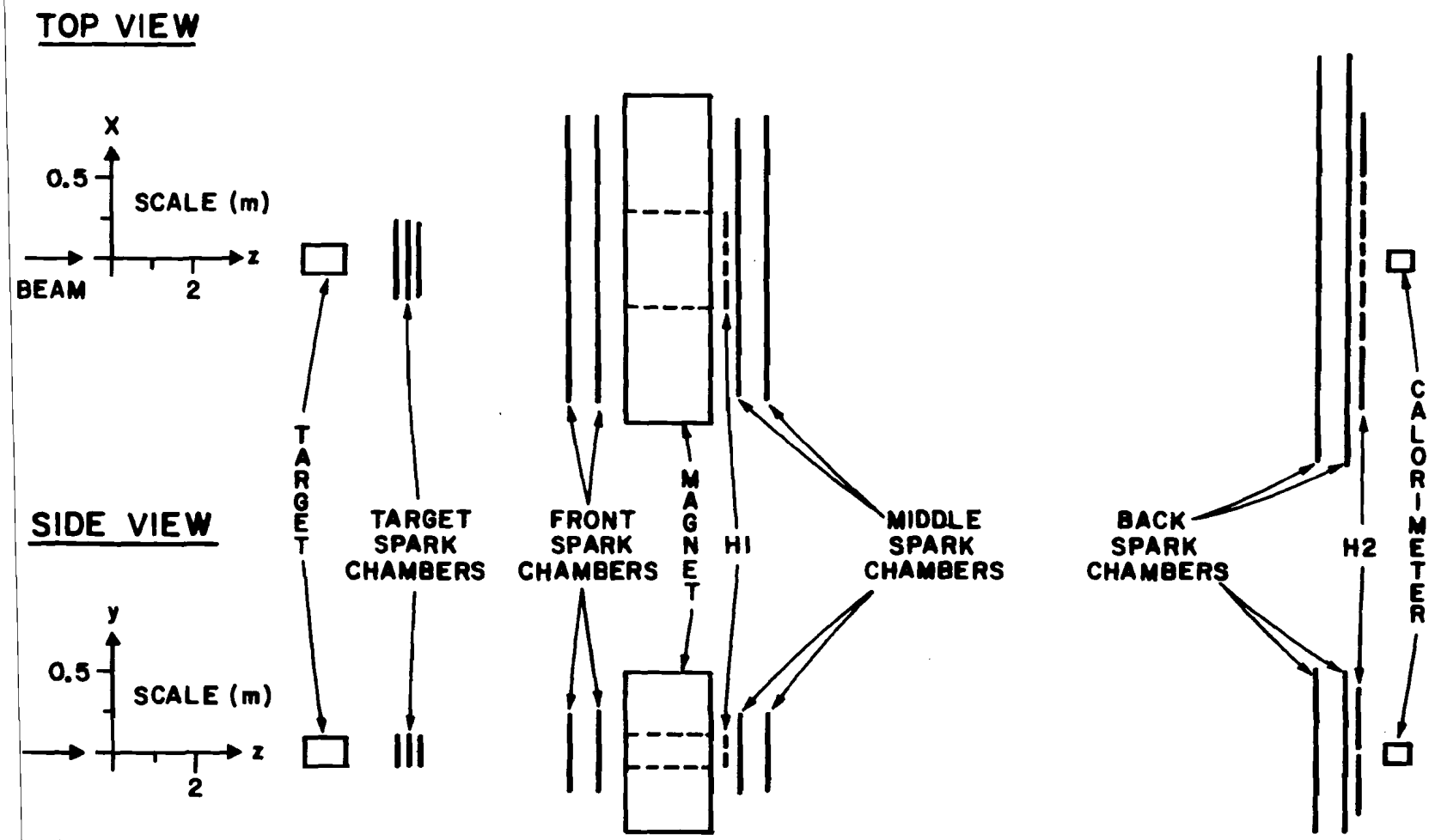
TOP VIEW
X
0.5
SCALE (m)
BEAM
2
z
SIDE VIEW
y
0.5
SCALE (m)
2
z
TARGET
TARGET SPARK CHAMBERS
FRONT SPARK CHAMBERS
MAGNET
H1
MIDDLE SPARK CHAMBERS
BACK SPARK CHAMBERS
H2
CALORIMETER

Figure 6

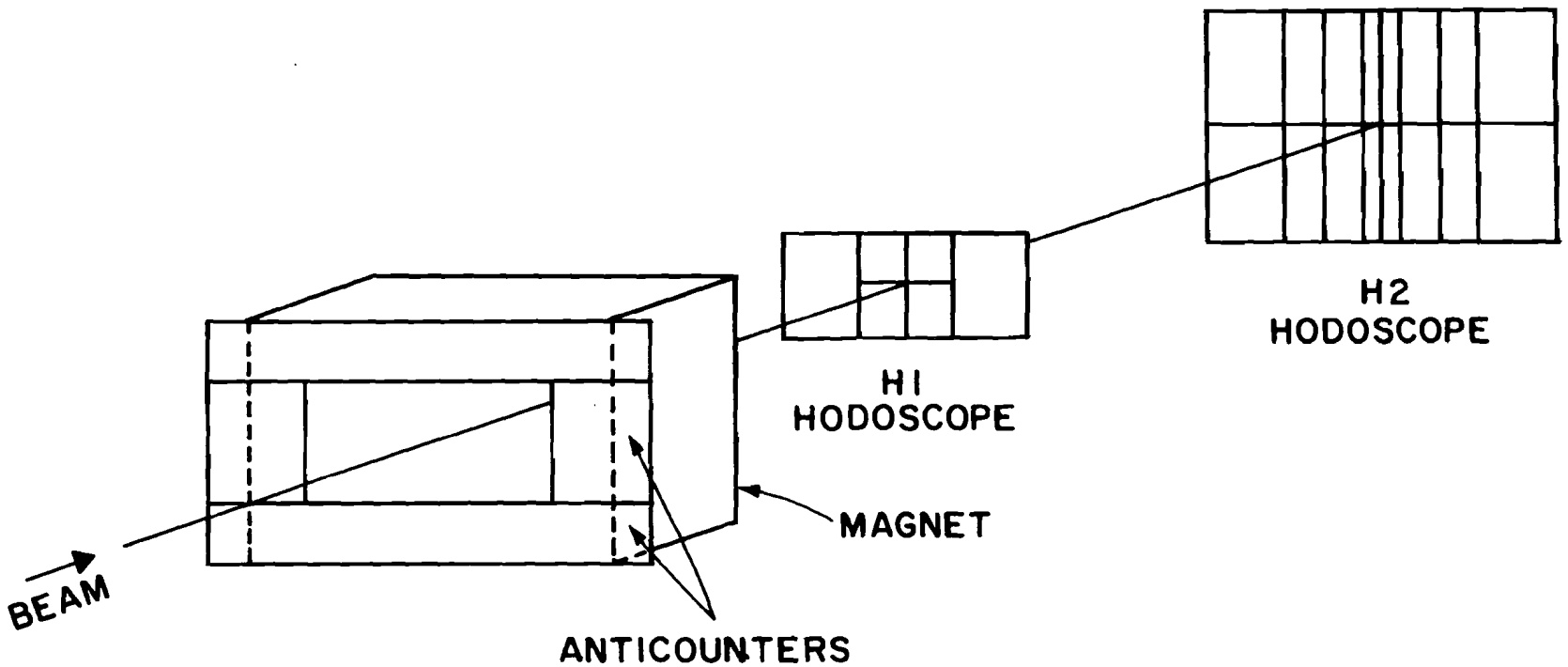

Figure 7

sixteen counters (H2) was located at the extreme downstream end of the spectrometer.

2. Spark Chambers

Thirty planes of spark chambers were used to determine the trajectories of charged particles within the spectrometer. Each plane recorded the position of any charged tracks passing through it in either the x, y, u or v direction. The coordinate system used defined y as vertical, x as horizontal, and z in the direction of the beam. Wires for the u and v planes were rotated either $\pm 15°$ or $\pm 45°$ relative to the y direction. The chambers were grouped into four sets with two sets, "target" and "front", upstream of the magnet with the remaining two sets, "middle" and "back", downstream of the magnet.

The positions of sparks were determined using a magnetostrictive read-out technique. The process began when, upon detection of an event by the trigger logic, a high voltage pulse was applied between the planes of chamber wires. Sparks then formed between the high voltage and ground planes (Fig. 8) with the most likely points of breakdown being at the positions where any charged particles had recently passed. Since the chamber planes consisted of an array of finely spaced wires (40 per inch), the current drawn by each spark flowed through the wire (or wires) closest to the spark.

A magnetized read-out wire was placed along the edge of each plane with only a thin layer of mylar insulation separating it from the spark chamber wires. The current pulse flowing along a wire

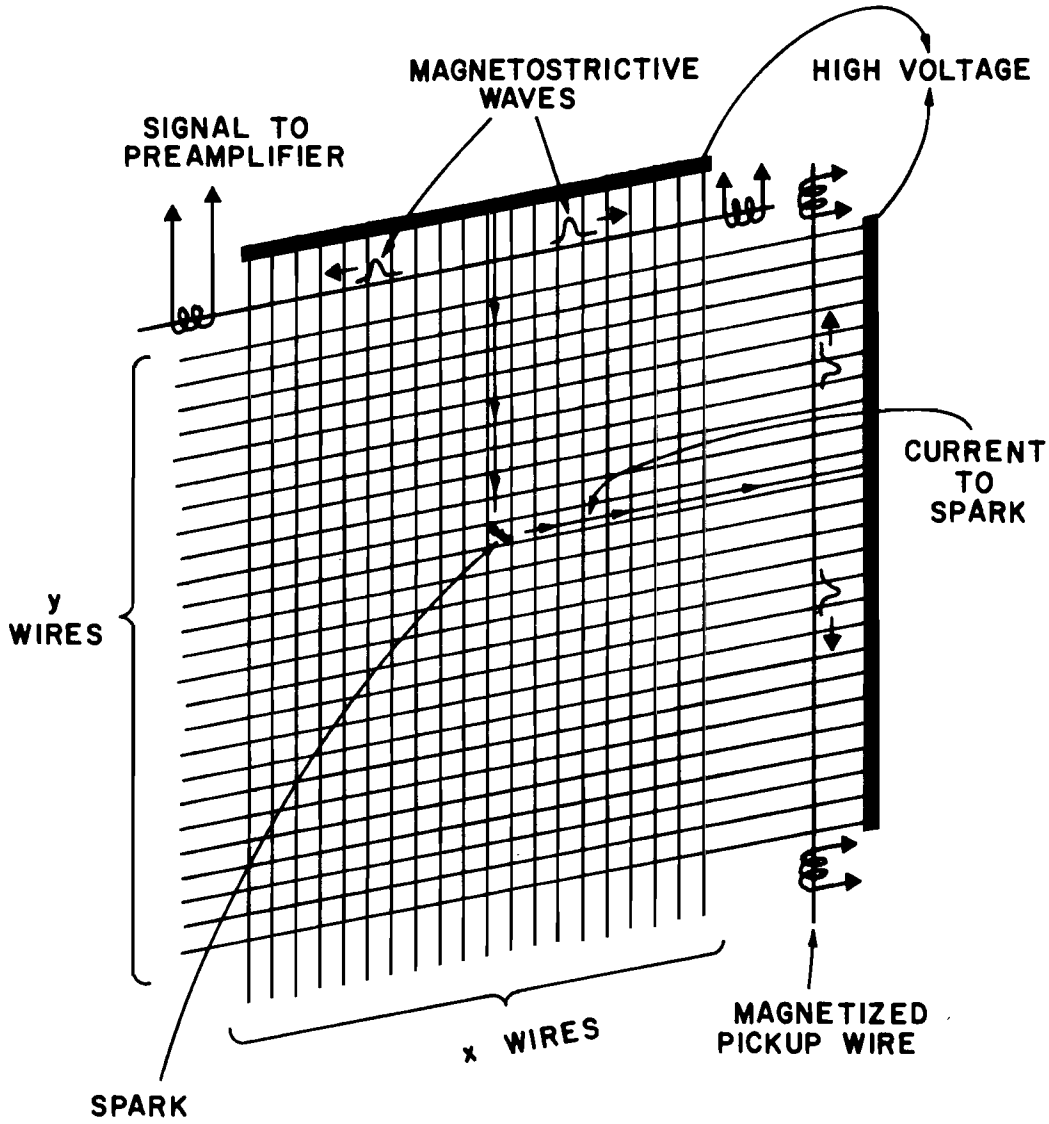
MAGNETOSTRICTIVE WAVES
HIGH VOLTAGE
SIGNAL TO PREAMPLIFIER
CURRENT TO SPARK
y WIRES
x WIRES
MAGNETIZED PICKUP WIRE
SPARK

Figure 8

toward the location of a spark produced a corresponding pulsed magnetic field around the wire. When this pulsed magnetic field interacted with the static field around the readout wire a shock wave was produced which propagated toward both ends of the readout wire at the velocity of sound. At each end of the readout line special "fiducial" wires were also pulsed upon detection of every desired event.

As each sonic wave reached the end of the readout line, the longitudinal movement of the magnetized wire induced a current in a surrounding pickup coil. The time between a fiducial and a spark signal, together with a knowledge of the velocity of sound in the readout wire, allowed the calculation of the distance from the fiducial wire to the spark wire. Since the distance between fiducials was known, measuring the time interval between the two fiducial signals allowed the velocity of sound to be monitored continuously in each readout line.

The signal from each readout line was next amplified, discriminated, and converted into a standard logic pulse. Associated with each line was a set of four fourteen bit binary scalars which were reset to zero before any readout signals had arrived. When the first readout pulse, normally from the first fiducial, had been detected, all scalars began to count signals from a high speed clock (20 MHz for the back stand of chambers and 40 MHz for all other planes). Subsequent spark readout pulses stopped the counting scalars in a specified order. That is, the second pulse stopped the first scalar, the third pulse stopped the second scalar and so

on. If less than five pulses were received, the extra scalars were stopped when they overflowed and an extra indicator bit was set. Any pulses after the fifth one were lost. For the cases when the scalers were started by the signal from the first fiducial, the counts in each of the scalars were directly related to the time lapse between the first fiducial and the particular signal pulse. To provide the system with a degree of redundancy, the signals from both ends of each readout line were digitized independently.

3. Analyzing Magnet

Momentum analysis of charged particles was provided by a BM109 dipole magnet with an aperture 20 cm high and 60 cm wide. The 18 kilogauss field region extended for 1.9 m along the z direction and delivered a momentum kick of approximately 1 GeV/c in the x direction. For the momentum range of particles studied, a sufficient approximation to the magnetic field was obtained by assuming a constant field within the magnet and no fringe field.

4. Calorimeter

Downstream of all spark chambers, at a distance of approximately 26 meters from the hydrogen target, a small hadron calorimeter was placed in the beam line (Fig. 9). Twenty one iron plates, 10 cm × 10 cm × 2.5 cm in size, were interleaved with 10 cm × 10 cm sheets of plastic scintillator, producing approximately three absorption lengths of material. The discriminator levels on the photomultiplier tubes of the calorimeter were set low enough to detect

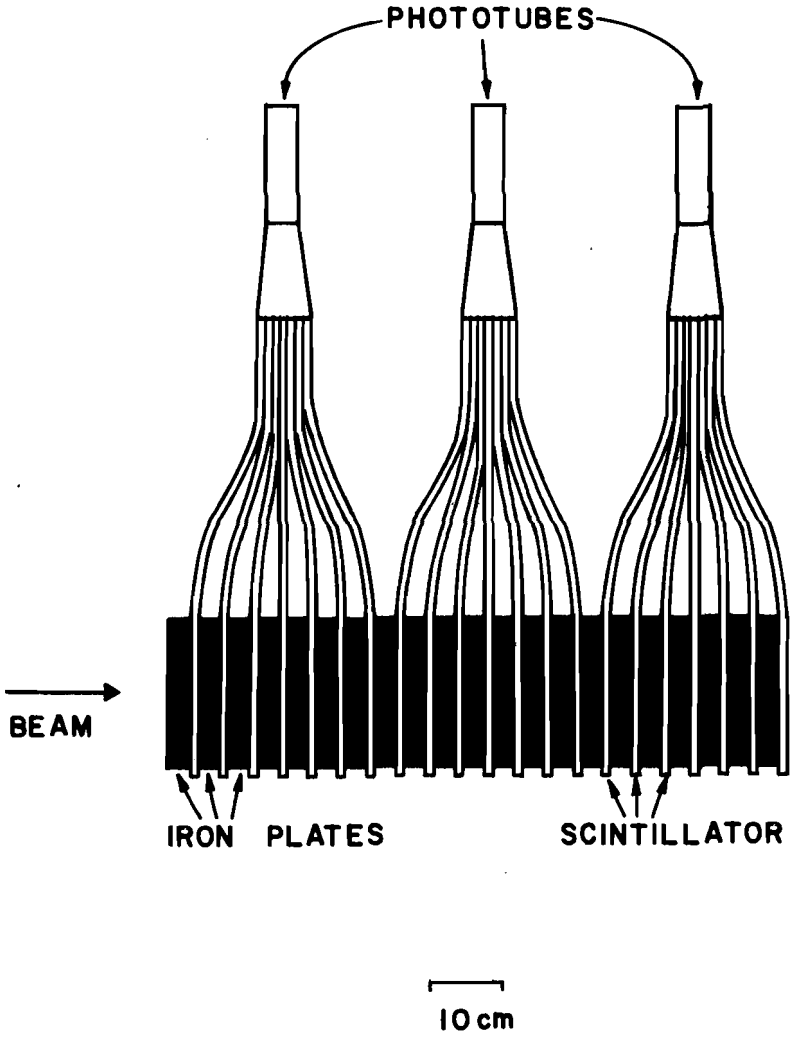

Figure 9

any charged particles produced within or traversing the calorimeter. The motivation for augmenting the spectrometer with this device was the detection of multibody dissociation processes such as

$$n + p \rightarrow n + \pi^{+} + \pi^{-} + p$$

which would contain a high energy neutron in the forward direction. As will be shown later, such processes were indeed observed as a significant background in our data. The calorimeter was also used to count the number of neutrons in the beam, and thereby provide a normalization for our measurements of the dissociation cross section.

D. Event Trigger

The detection of a possible neutron-dissociation event in the spectrometer was accomplished by requiring a set of coincident signals from the scintillation-counter system. A candidate event was required to have:

(1) At least one charged-particle present immediately following the target region,

(2) At least two particles traversing the H1 hodoscope,

(3) A recoil proton detected within the hydrogen target.

Condition (1) was satisfied by the observation of a signal from both phototubes associated with the S counter (S_U and S_D) at the downstream end of the high pressure hydrogen. The second condition required signals from exactly two H1 scintillators. Events having more than two charged tracks were not totally eliminated by this

procedure since it was possible for more than one particle to pass through the same element of the H1 array. Event candidates were considered to have a probable recoil proton if signals were observed simultaneously from only one upstream recoil-counter phototube and only one downstream phototube. No requirement was made in the trigger that the two phototubes be at opposite ends of a single scintillator. Subsequent analysis showed that this was, however, the case for approximately 85% of all recorded triggers.

The above trigger criteria were then augmented by requiring that no signals were observed in the veto counters. The first of these, A_0, was located within the high pressure vessel, and defined the upstream end of the target volume. A signal observed from either of the two phototubes associated with this counter (A_{OL}, A_{OR}) indicated that a charged particle rather than a neutron entered the target region, and the event was therefore rejected. The additional veto counters (A1-A4) were positioned to cover the region surrounding the spectrometer magnet aperture and eliminated events which had additional particles in this area. In summary, the complete trigger, T, can be written as

$$T=S_U \cdot S_D \cdot \left(\begin{array}{c}\text{Two}\\ \text{H1}\\ \text{counters}\end{array}\right) \cdot \left(\begin{array}{c}\text{One}\\ \text{Upstream}\\ \text{Target}\\ \text{Phototube}\end{array}\right) \cdot \left(\begin{array}{c}\text{One}\\ \text{Downstream}\\ \text{Target}\\ \text{Phototube}\end{array}\right) \cdot \overline{(A_{OL}+A_{OR})} \cdot \bar{A}_1 \cdot \bar{A}_2 \cdot \bar{A}_3 \cdot \bar{A}_4$$

E. Trigger Rates

The trigger rate was an approximately linear function of target pressure for pressures up to 1250 p.s.i. Typically 90% of the event

candidates were eliminated by the veto counters. Data was originally taken with a target pressure of 1250 p.s.i., but later lowered to 750 p.s.i. allowing lower-energy recoil protons to reach the recoil counters. At the lower pressure there were 5-10 triggers per machine cycle (a five second acceleration cycle followed by a one second spill) with about 2×10^5 neutrons per spill.

F. Data Acquisition

After each trigger, all the information required to describe the event was transferred through a CAMAC interface system into the memory of our online PDP15 computer. In addition to the scalars containing the spark chamber information, a number of other quantities were recorded. These included pulse-height information from the target and calorimeter counters, along with an indication of which H1 and H2 hodoscope counters had been activated in the event. Scalar readings for our calorimeter, as well as other monitoring counters, were also saved. After ten events had been accumulated the stored information was written onto magnetic tape. Throughout the course of the experiment the computer also made a number of checks on the quality of the incoming data. Numerous displays were available which allowed the continuous monitoring of spectrometer performance.

G. Summary of Data

The results presented in this report represent the analysis of approximately 4×10^5 triggers. About one quarter of these were

taken with a target pressure of 1250 p.s.i., with the rest at a pressure of 750 p.s.i. The data were collected in two, roughly equal, running periods in July and September of 1974.

CHAPTER III

ANALYSIS OF DATA

A. Reconstruction of Events

1. Check for Recoil Proton

The reconstruction of an event was begun by checking the signals from the hydrogen target. All pulse heights from the azimuthal recoil counters were examined to check that the two largest signals were from phototubes at opposite ends of one of the sixteen recoil scintillators. Events for which this was not the case lacked a clear recoil proton signal and were removed from the data. Approximately 85% of all triggers passed this requirement. In subsequent discussion, the phototube signals from the recoil counters will be referred to as A_{up}, for the upstream end of the target, and A_{down} for the downstream end of the target.

2. Calculation of Spark Position

As described in Chapter II, spark positions were initially recorded in terms of the number of clock pulses which lapsed between the observation of the first fiducial and the arrival of a spark pulse. Scaler values were subsequently converted to position measurements by using the velocity of propagation of signals on the magnetostrictive line (which in turn was obtained from the known

distance and the measured number of clock pulses between two fiducials). If, for some readout line, s_f was the scaler reading for the second fiducial, then a spark with scaler value s had a calculated position x_s given by

$$x_s = \left(\frac{d_f}{s_f}\right) \cdot s + x_o$$

where d_f was the distance between fiducials and x_o was the spatial position of the first fiducial. After all the spark coordinates were calculated from their corresponding scaler values, the spark positions determined from opposite ends of each readout line were compared for consistency. Those sparks whose coordinates matched to within 3 mm (∿8 times the resolution) were combined to yield a single average spark position.

3. Search for a Dissociation Event

(a) Location of Tracks

A search was next performed for particle tracks within the spectrometer. Sparks from the x planes were examined first. A tentative track segment was formed using only those sparks from the middle chambers (Fig. 6). This segment was extrapolated to the downstream end of the spectrometer and, if it intersected the back chambers, at least one spark was required to be located initially within 10 cm of the track. The track was also extrapolated to the center of the magnet. Subsequently, using a thin lens magnet approximation, the upstream portion of the track was approximated by a line drawn from the trajectory point at the center of the

magnet to the target position. The front chambers were then examined and each track had to have at least one spark in these chambers. A set of geometric parameters was saved for each track meeting the above criteria.

After all potential tracks were located in the x view, a search was made for the corresponding track in the y view. Since the magnetic field of the spectrometer magnet was along the y direction, there was a negligible change in the y slope of a track upon its passage through the magnet. This reduced the problem of reconstruction in the y view to one of locating all sets of y sparks that formed straight lines through the spectrometer.

The u-v planes were also used in reconstructing the y view. For each tentative track in the x view the predicted x values at all u or v planes were first calculated. These predicted x values were used in conjunction with the known angles of rotation of the spark chamber wires, to obtain a y coordinate from each u or v spark. Only those u-v sparks which lined up with y chamber sparks were used in the final reconstruction. In this way, locating tracks in the y view simultaneously matched each y track to an x track. After all tentative tracks had been found, each positive track was paired with each negative track and an attempt was made to fit the combination as dissociation products originating from a common vertex. Events in which no pair of oppositely charged tracks could be found were discarded.

(b) Determination of the z Coordinate of the Vertex

Because the angle between the two tracks upstream of the magnet was small (∿10 mR), the z coordinate of the interaction vertex obtained by using the spark chamber tracks was often uncertain to several tens of centimeters. This error was greatly reduced by using the recoil scintillators to determine the location of the interaction vertex. Assuming an exponential loss for light travelling along one of these scintillators, we can express the observed pulse height at either end as follows:

$$A_{up} = e_{up} \cdot Ae^{-az}$$

$$A_{down} = e_{down} \cdot Ae^{-a(\ell - z)}$$

where A is proportional to ionization produced within the scintillator by the recoil proton, z is the position along the scintillator at which the recoil struck, a is the attenuation coefficient for light travelling through the scintillator, ℓ is the length of the scintillator strip and e_{up} (e_{down}) is the efficiency of the upstream (downstream) light guide and phototube system. Solving for z we have

$$z = \frac{1}{2a} \ln \left[\frac{A_{down}}{A_{up}}\right] + \frac{1}{2a} \left[\ln \left[\frac{e_{up}}{e_{down}}\right] + a\ell\right]$$

or

$$z = C_1 \ln \left[\frac{A_{down}}{A_{up}}\right] + C_2 \quad .$$

The constants C_1 and C_2 were determined for each scintillator by reconstructing a fraction of the data without using the information

from the hydrogen target and then plotting the z coordinate of the vertex as a function of $\ln (A_{down}/A_{up})$. Figure 10 illustrates the correlation observed for a typical target counter. For this plot we used only those events with large opening angles and, therefore, small errors in the z coordinate of the vertex.

(c) Least Squares Fit

After the location of the vertex and the track elements an iterative least squares fit was performed to the sparks. Those sparks which deviated by more than 2 mm from the fitted trajectory were removed. If the same spark had been used for both tracks of the Vee, subsequent to the first iteration, it was assigned to the closest track. After the fit, track pairs with a high χ^2 or with a track containing an excessively small number of sparks were dropped.

(d) Elimination of Spurious Multiple Tracks

Events which had more than one pair of oppositely charged tracks were subjected to more detailed examination. Many of these events contained sets of tracks which were nearly identical in their composition of sparks. In such cases, only the highest quality track (determined by the relative χ^2 and number of sparks) was retained. If, after this selection, more than a single Vee still remained, the event was then rejected. Approximately 60% of all triggers survived the entire reconstruction process.

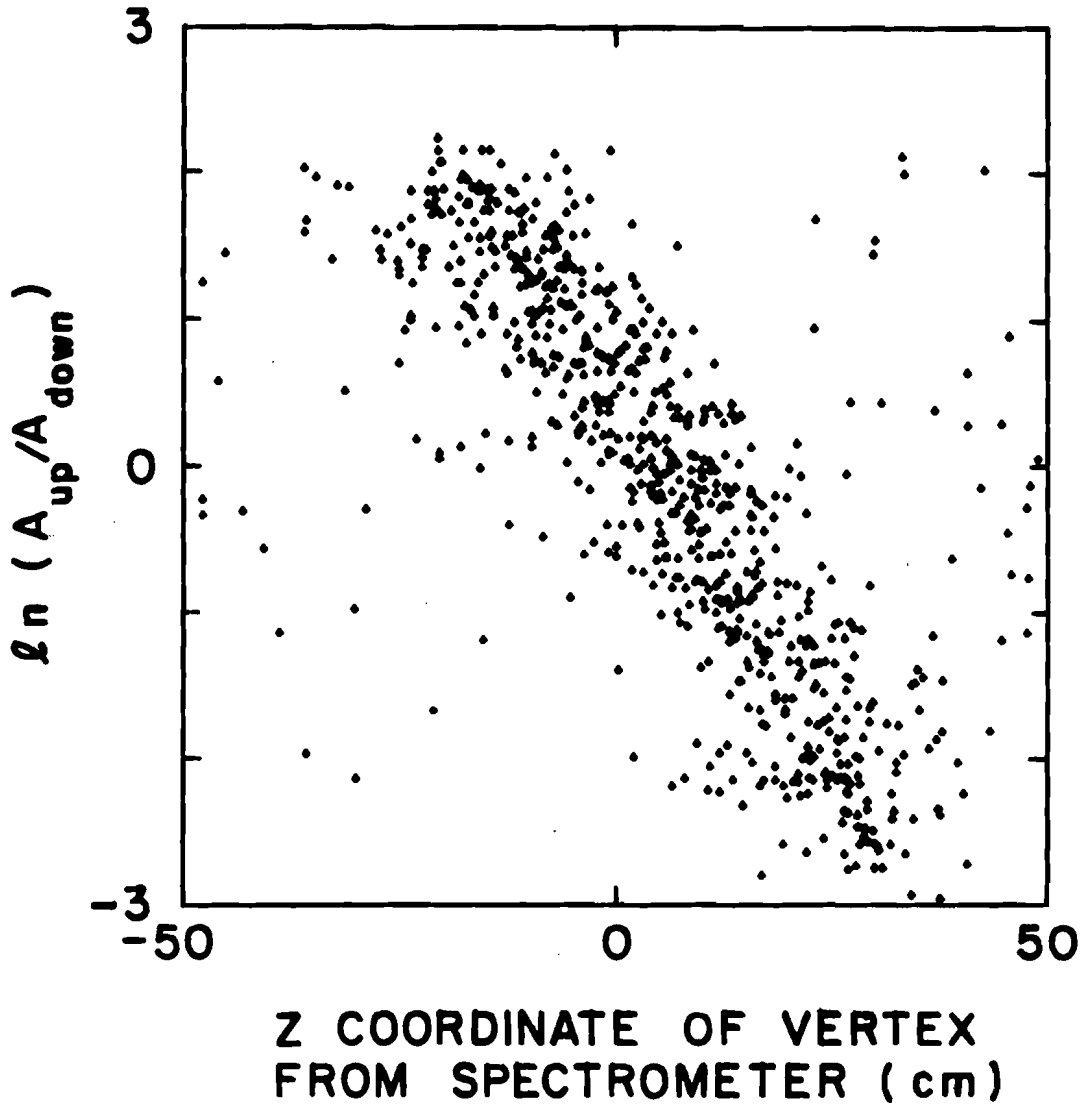
3
0
-3
-50
0
50
ℓn (A_up/A_down)
Z COORDINATE OF VERTEX
FROM SPECTROMETER (cm)

Figure 10

B. Correction for Geometrical Efficiency

Because of the dimensions of the spectrometer, not every event was produced in such a way as to be able to trigger the apparatus. Consequently, the data had to be corrected for various geometric cuts and losses. This was done by calculating a weight for each event through a Monte Carlo technique. Although nine parameters are needed to fully describe a two-track event having a common vertex, only five variables (e.g., $p, M, t, \cos\theta_{GJ}, \phi_{GJ}$) are needed to fully specify the kinematics of the dissociation reaction. The "physics" content of an event is not affected by the particular way we choose the four remaining parameters. The latter were chosen for convenience in the Monte Carlo, to be the three coordinates of the production vertex (x_v, y_v, z_v) and the azimuthal orientation of the plane of the Vee event about the z axis (ϕ).

To obtain a weight for each physical event, a number of fictitious events were generated having the same kinematic properties but random values for x_v, y_v, z_v and ϕ (these were generated over the same range of values as found in the data as a whole). These Monte Carlo events were tracked through the spectrometer to determine if the event would produce a trigger or not. The weight was then taken to be:

$$W = \frac{\text{NUMBER OF EVENTS GENERATED}}{\text{NUMBER OF GENERATED EVENTS PRODUCING TRIGGERS}} .$$

Enough events were generated to insure that the fractional statistical error on the weight was at most 10%.

The experiment events were also tracked through the apparatus and a few per cent failed due to the idealized geometry of the spectrometer used in the Monte Carlo calculation. The events which failed this check were eliminated from the sample because they were already compensated for by the remaining (weighted) events. A histogram of the final weight spectrum is given in Fig. 11. A plot of the average geometric efficiency of the spectrometer as a function of p, M, and t is presented in Fig. 12.

Below a neutron momentum of 50 GeV/c the geometric efficiency falls rapidly. This problem is further aggravated by the reconstruction program's difficulty in locating tracks with momenta below 5 GeV/c. Furthermore, as will be shown in the following sections, many background corrections are most important at low beam momentum. For the above reasons, events with neutron momenta below 50 GeV/c were discarded.

In addition to calculating a weight for each observed event, the acceptance of the apparatus was also studied using events generated for all regions of phase space. This simulation procedure revealed the existence of a kinematic region for which the geometric acceptance was $\sim$1%. The biased regime corresponded to values of $\cos\theta > 0$ (for the Gottfried-Jackson frame), and was strongly dependent on mass and the incident neutron momentum. For small M values, this bias was limited to very low momenta ($\lesssim$ 50 GeV/c), but for masses of 2 GeV/c^2 the bias problem was significant up to momenta of approximately 200 GeV/c. The Monte Carlo weight

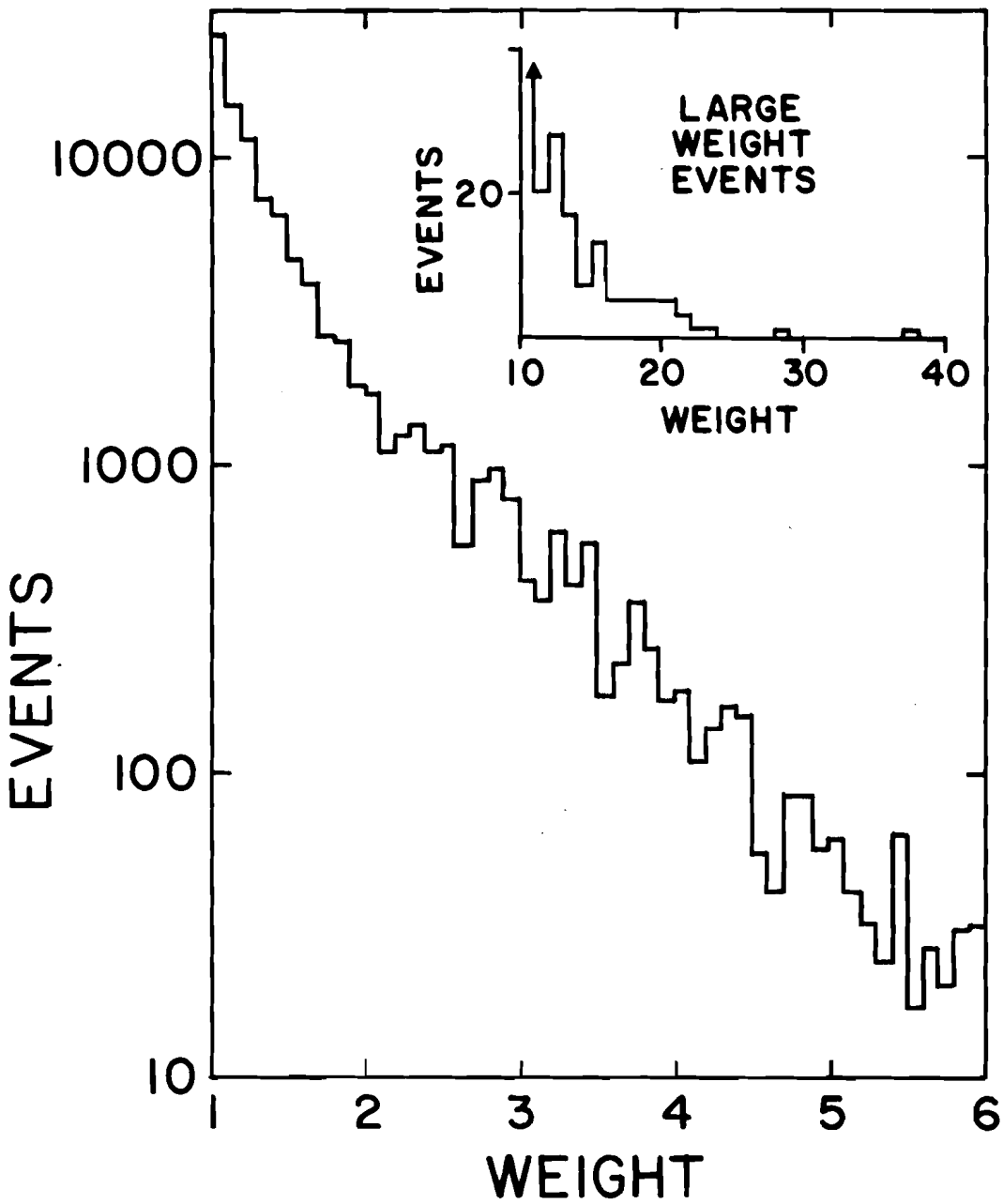
10000
1000
100
10
EVENTS
1
2
3
4
5
6
WEIGHT
LARGE
WEIGHT
EVENTS
20
EVENTS
10
20
30
40
WEIGHT

Figure 11

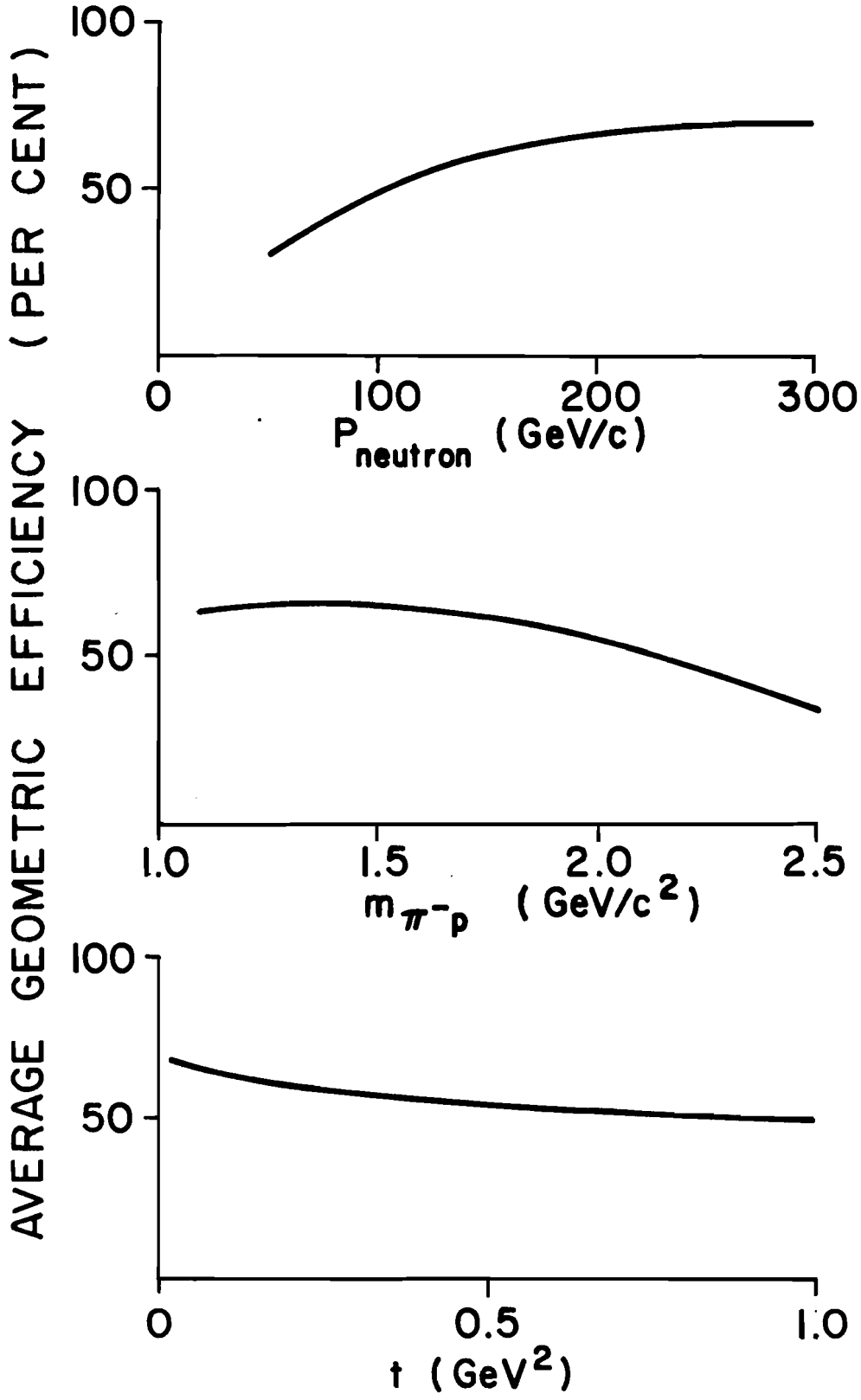
AVERAGE GEOMETRIC EFFICIENCY (PER CENT)
100
50
0
100
200
300
P neutron (GeV/c)
100
50
1.0
1.5
2.0
2.5
m π⁻p (GeV/c²)
100
50
0
0.5
1.0
t (GeV²)

Figure 12

calculation described above corrects only for lost events if other similar events are present, and is consequently inadequate for handling a region of miniscule acceptance. Experimental evidence for such gross losses, as well as the steps taken to correct them, will be discussed in Section D.

C. Corrections for Background

1. Calorimeter

As was mentioned in the first chapter, the calorimeter was intended to detect reactions such as

$$n + p \rightarrow n + \pi^{+} + \pi^{-} + p$$

For reactions of this kind it is expected that the final-state neutron would, in a substantial fraction of these events, have a momentum and direction similar to that of the incident neutron beam. Figure 13a displays the experimentally observed distribution for the sum of the pulse heights from the three phototubes of the calorimeter. While the bulk of the data have small pulse heights, there is nevertheless a long tail to the distribution extending to very large pulse heights. The small fraction of the events for which the trajectory of one of the reconstructed charged-particle tracks of the Vee intersected the calorimeter position was removed from the distribution. The energy deposited in the calorim- can, therefore, be attributed to secondary interactions of neutral hadrons in the calorimeter. Events with a

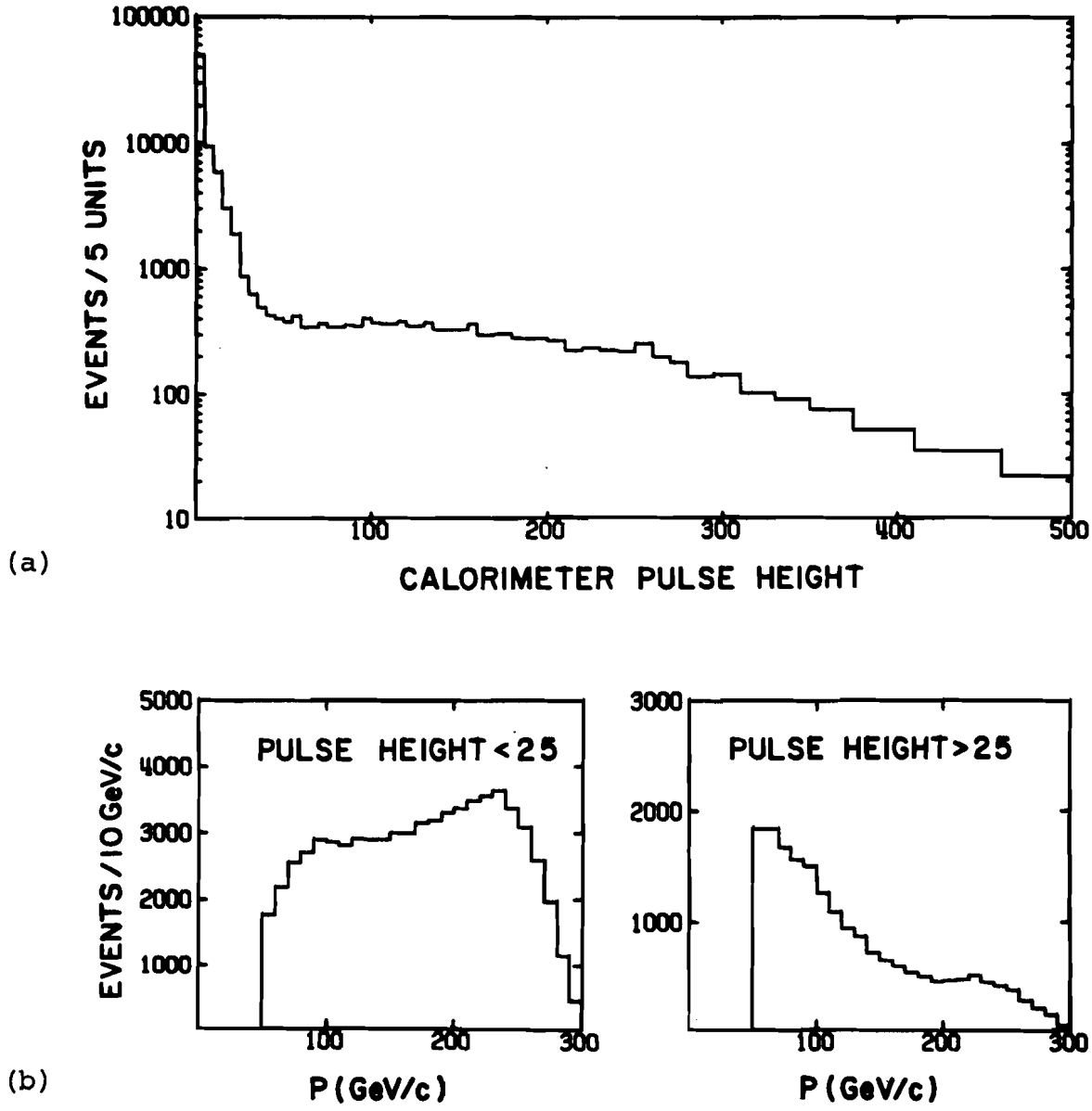
100000
10000
1000
100
10
EVENTS / 5 UNITS
100
200
300
400
500
(a)
CALORIMETER PULSE HEIGHT
5000
4000
3000
2000
1000
EVENTS / 10 GeV/c
PULSE HEIGHT < 25
100
200
300
P (GeV/c)
3000
2000
1000
PULSE HEIGHT > 25
100
200
300
P (GeV/c)
(b)

Figure 13

pulse height of 25 or greater were judged to result from interactions of neutrons and these were consequently eliminated from consideration. A further indication that this interpretation was sound can be found by examining the momentum spectrum of the incident neutrons for those events with calorimeter pulse heights above 25. When compared with the spectrum for the remaining events (Fig. 13b), the data having large pulse heights show a dramatic low-momentum enhancement. This is exactly what one would expect, because the secondary neutron is degraded in momentum relative to a neutron-beam particle.

Unfortunately, the calorimeter was available for only approximately 60% of our data taking. Although, without the calorimeter signal, the background events could not be identified on an individual basis, they were corrected for in a statistical manner as follows. Events with large pulse heights were not discarded, but were rather given negative weights whose magnitude was the ratio of the total number of events having no calorimeter information to the number of events for which the calorimeter information was available. In this way whenever the entire data sample was plotted in a histogram, a proper background subtraction was automatically made for events with large pulse heights, which effectively served to remove contamination from this background on, at least, a statistical basis.

2. Hydrogen Target

(a) Recoil-Angle Distribution

The pulse height information obtained from the hydrogen target phototubes proved to be an extremely valuable means for

eliminating background events. To begin with, the angle of the recoil proton, as calculated from the π^- and p momenta measured in the spark chamber spectrometer, was compared with the recoil direction as determined by the recoil counters which detected the proton (Fig. 14a). A typical distribution in the difference between the calculated recoil angle and the observed angle of the recoil signal, for one of the sixteen recoil counters, is shown in Fig. 14b. Most of the events have a ϕ angle within the angular resolution of the recoil counter (360°/16=22.5°). As was the case for events having large calorimeter pulse heights, we attribute events outside of the peak to background reactions involving missing neutrals, e.g.:

$$n + p \rightarrow n + \pi^+ + \pi^- + p$$
$$n + p \rightarrow p + \pi^- + \pi^o + p$$

For these type of events, the calculation of ϕ is based only upon the observed charged tracks and therefore cannot yield the correct direction of the recoil proton. (The effect of experimental measuring error on the recoil angle calculation will be considered later.) Again, as was the case for events with large pulse heights in the calorimeter, the indication of additional missing neutrals is corroborated by a low-momentum enhancement in the beam spectrum for events outside of the peak region in ϕ (Fig. 15a).

(b) Energy Loss of the Recoil Proton

Formulas for pulse heights observed by the phototubes at either end of the target recoil counters have previously been given

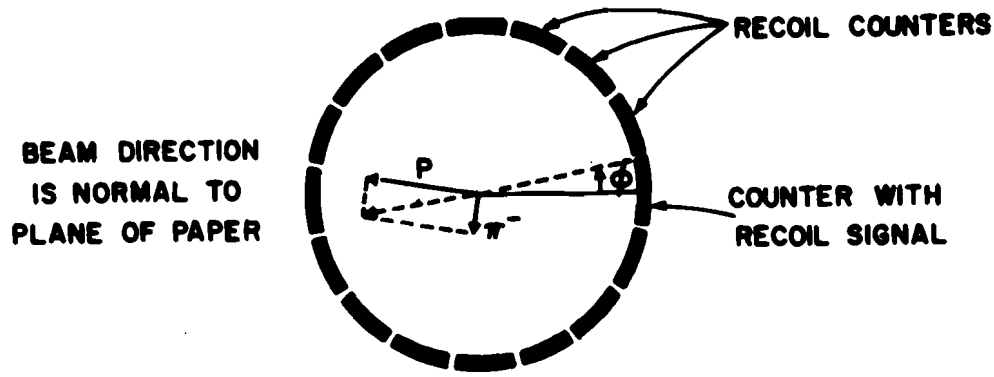

(a): DEFINITION OF RECOIL-ANGLE ϕ

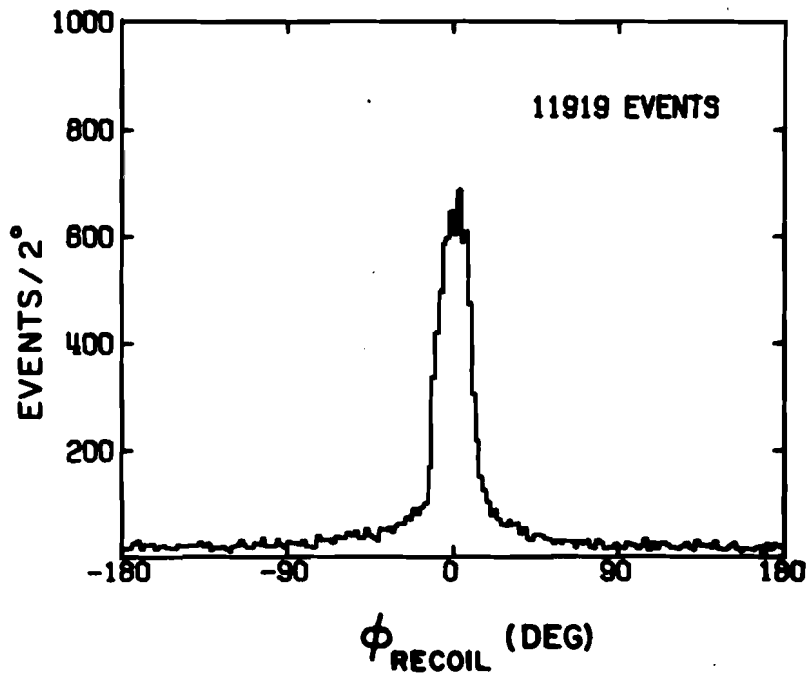

(b): TYPICAL RECOIL-ANGLE DISTRIBUTION

Figure 14

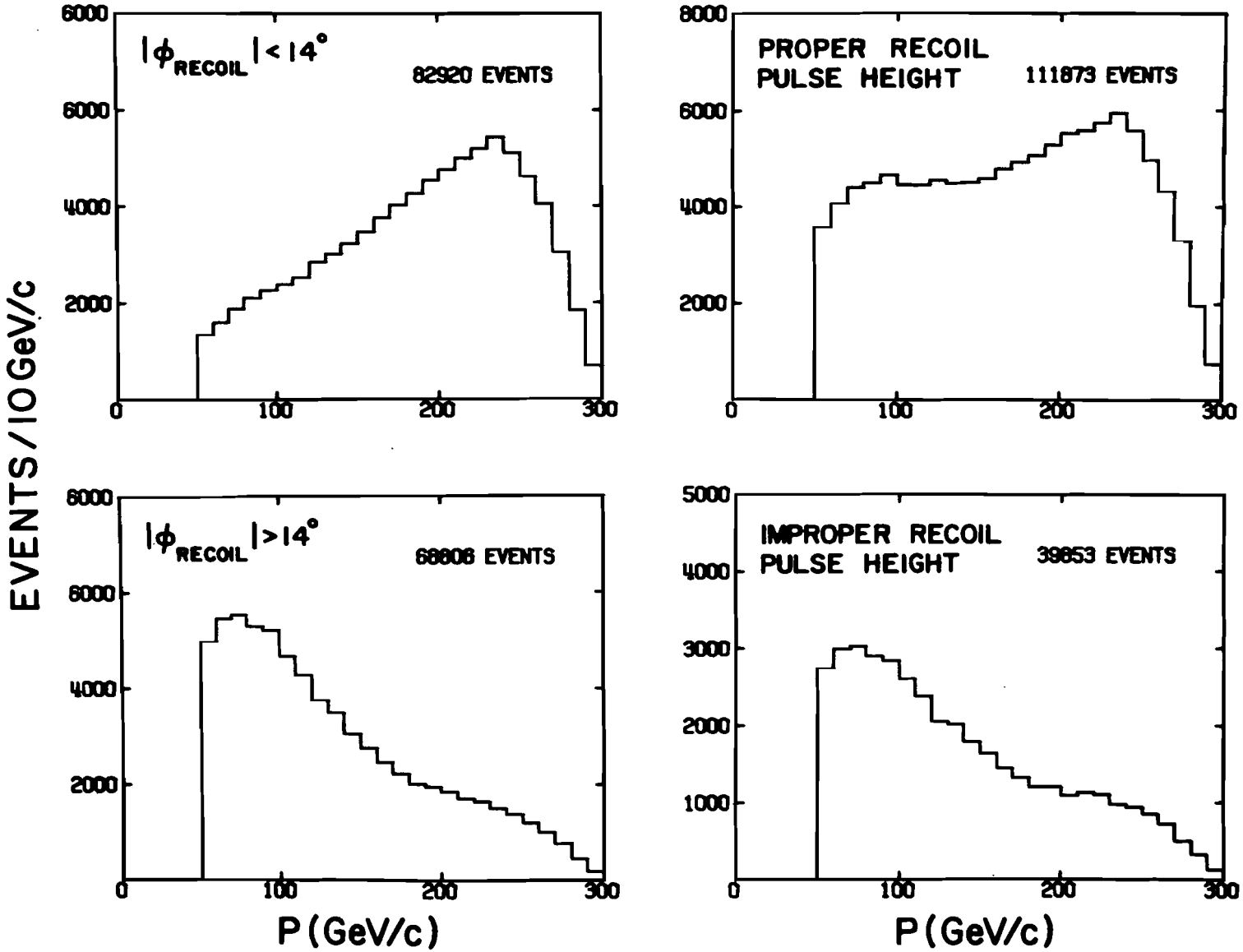
EVENTS/10GeV/c
$|\phi_{RECOIL}| < 14°$
82920 EVENTS
$|\phi_{RECOIL}| > 14°$
68806 EVENTS
PROPER RECOIL PULSE HEIGHT
111873 EVENTS
IMPROPER RECOIL PULSE HEIGHT
39853 EVENTS
P(GeV/c)
P(GeV/c)

(a) (b)

Figure 15

in section A-3 of this chapter. Using these equations we can define an average pulse height $\bar{A}$ as follows:

$$\bar{A} \equiv \sqrt{A_{up} \cdot A_{down}} = \sqrt{e^{-a\ell} e_{up} e_{down}} \cdot A$$
$$= C \cdot A$$

where A is proportional to the energy lost within the scintillator by the recoiling proton, A_{up} and A_{down} are the phototube pulse heights at the upstream and downstream end of the recoil counter, and C is a constant dependent on the nature of each recoil counter. Since the squared four momentum transfer, t, can be written as

$$t = 2m_p T$$

where m_p is the mass of the proton and T is the kinetic energy of the recoil proton in the laborabory, we can conveniently use t as a measure of T. A plot of $\bar{A}$ vs. t for a typical recoil counter is given in Fig. 16a. In this figure a band of high density is seen to rise linearly from the lower left hand corner until a t of approximately .06 GeV^2 is reached. For larger t, the band decreases in value and appears to be asymptotically approaching a horizontal line as t becomes large. The above description is in complete agreement with the expected signal from recoil protons. If the recoil has little kinetic energy, the proton will stop within the scintillator, depositing all its energy and producing a pulse height proportional to T (and therefore t). As T of the proton increases, the recoil will eventually pierce through the scintillator and

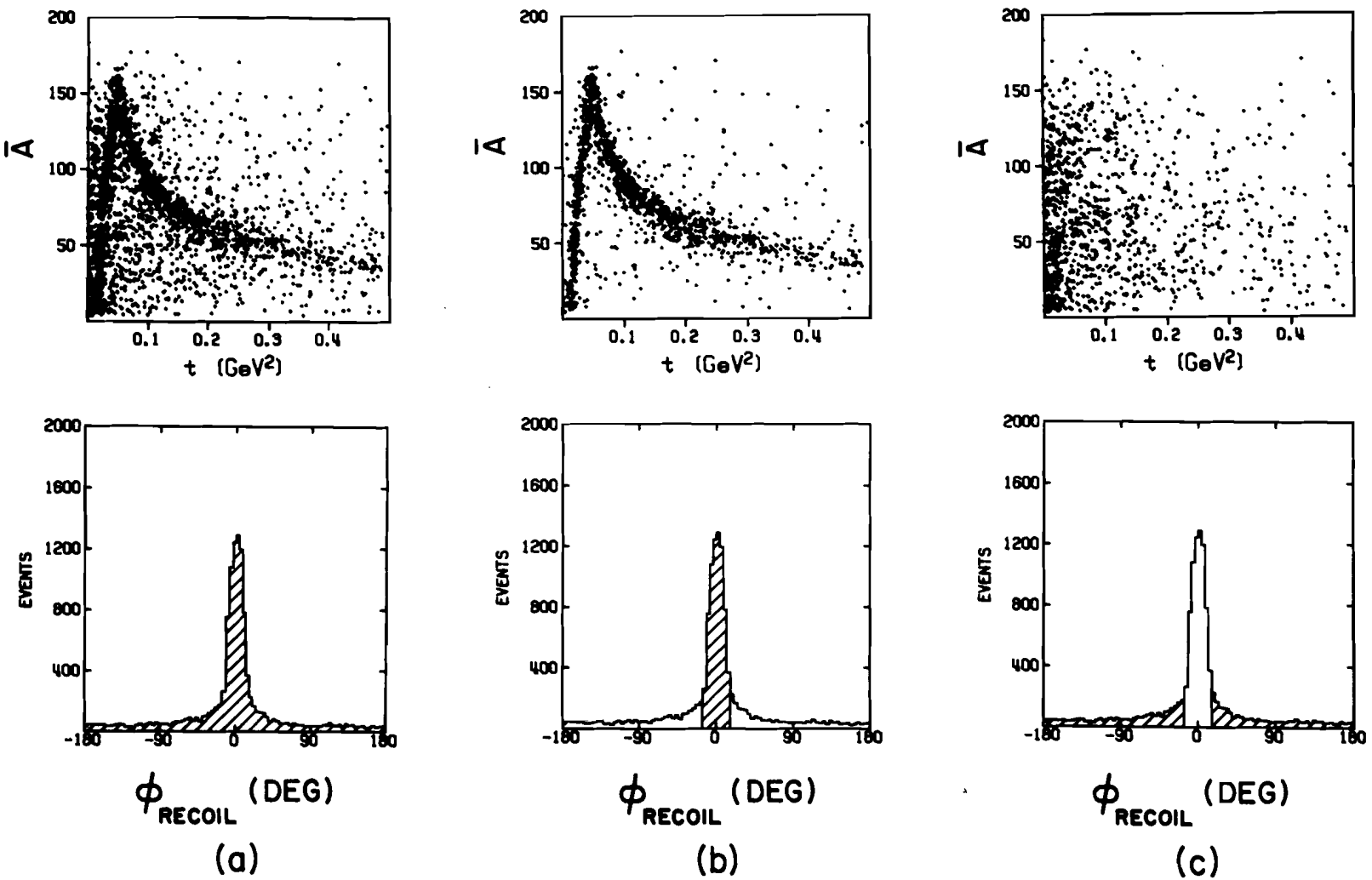
200
150
100
50
$\bar{A}$
0.1
0.2
0.3
0.4
t (GeV^2)
2000
1600
1200
800
400
EVENTS
-180
-90
0
90
180
ϕ_{RECOIL} (DEG)
(a)
(b)
(c)

Figure 16

deposit less than its total kinetic energy. At large values of T, the energy deposited within the scintillator will approach the value expected for a minimum ionizing particle.

If the data are divided into portions with small and large recoil angles (Figs. 16b and 16c), those events with small recoil angles are found to have a much cleaner energy-loss distribution. Using plots similar to these, events with improper recoil pulse heights were removed. As before, the momentum spectrum for the events removed (Fig. 15b) shows the low momentum enhancement expected when the final state contains additional missing neutrals. (Events with t values below 0.02 GeV^2 were also discarded because most of these would have had insufficient recoil energy to reach the counters and produce a trigger.)

(c) Background Subtraction Using Recoil-Angle Distributions

In addition to removing background by rejecting events with pulse heights outside of the signal band, we also imposed a cut off on the ϕ recoil angles. An event with a recoil angle of absolute value less than 14° was considered as an acceptable candidate for Reaction (1). We corrected this "signal" region of the data by subtracting from it events whose recoil angles had magnitudes between 14° and 28° (the "background" region); this had the effect of approximately removing effects caused by background events remaining in the signal region. An additional refinement was added to this procedure in order to correct for resolution error in our determination of the recoil angle. This is discussed below.

As with any measured quantity, there is an experimental uncertainty in the value of the proton recoil angle. Because of this, some of the events found in the background region are, in fact, good events with badly measured recoil angles. For our spectrometer, the angle error increases with increasing beam momentum and decreasing t. This effect is evident in the data shown in Fig. 17, where we display the t distribution as a function of beam momentum for events with ϕ between 14° and 28°. At low beam momentum the t distribution has an approximately e^{-7t} behavior, while at higher momenta a steep peak develops at small t with a e^{-30t} dependence. This is to be contrasted with the signal region which has an approximately e^{-10t} behavior and is nearly momentum independent. This strong t dependence at high momentum is caused by the increased number of low-t events with large errors in ϕ. Failure to compensate for this effect would have resulted in an over subtraction of background at high momentum and low t. A correction was, therefore, applied to the data using a Monte Carlo method described below.

For each event in the signal-region of the ϕ distribution a number of Monte Carlo events were generated in which the momentum vectors for the pion and proton for each Monte Carlo event were smeared by their estimated experimental resolutions. A new recoil angle was then calculated for each of these generated events and a count kept of how many remained within the signal region. The following weighting factor for the signal region:

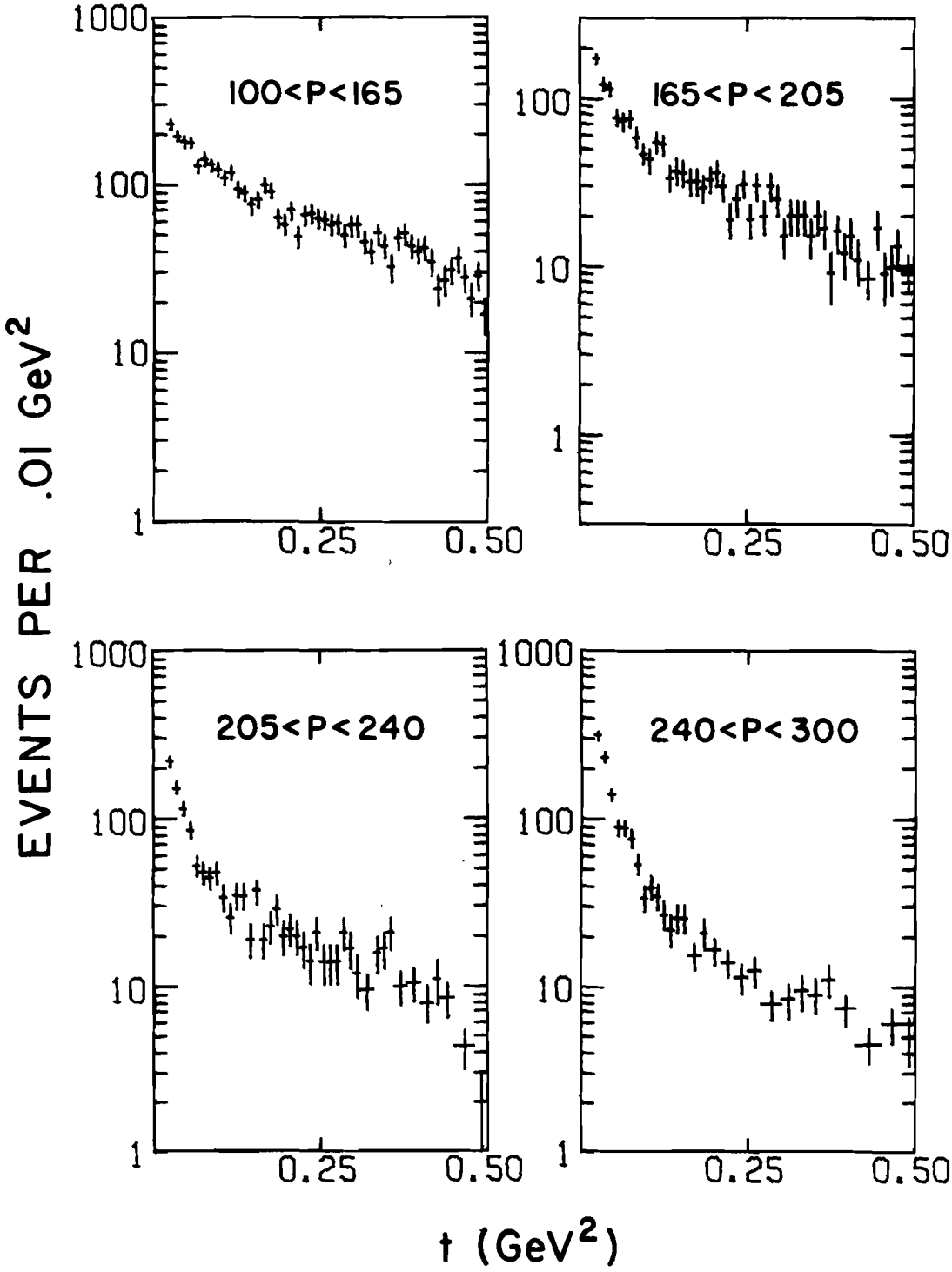
100<P<165
165<P<205
205<P<240
240<P<300
EVENTS PER .01 GeV^2
t (GeV^2)
1000
100
10
1
0.25
0.50

Figure 17

$$W = \frac{\text{NUMBER OF EVENTS GENERATED}}{\text{NUMBER OF GENERATED EVENTS WITH RECOIL ANGLES IN THE SIGNAL REGION}}$$

was then assigned to the event. As in the calculation of the geometric acceptance, enough events were generated to insure at most at 10% statistical error in W. The average value for W was 1.04 and the maximum weight was 2.65.

Having made the above correction, we were then able to proceed with the background subtraction. The weighted recoil angle distribution for the entire data sample is displayed in Fig. 18. At large recoil angles the distribution is well approximated by a straight line on a semilog plot. The plot was made using 7° bins, hence, the first two bins represent the signal region and the next two the background. Although the counts in the background bins are well above the line estimating the background level in the signal region, this excess is almost exactly equal to the calculated number of events lost from the signal because of resolution. If the indicated line in Fig. 18 is a good approximation of the real level of background, then it would appear that the background increases as the magnitude of ϕ decreases. This result led us to weight those events in the background region by yet another factor (approximately 1.2 as determined from Fig. 18) before subtracting the side bands from the signal.

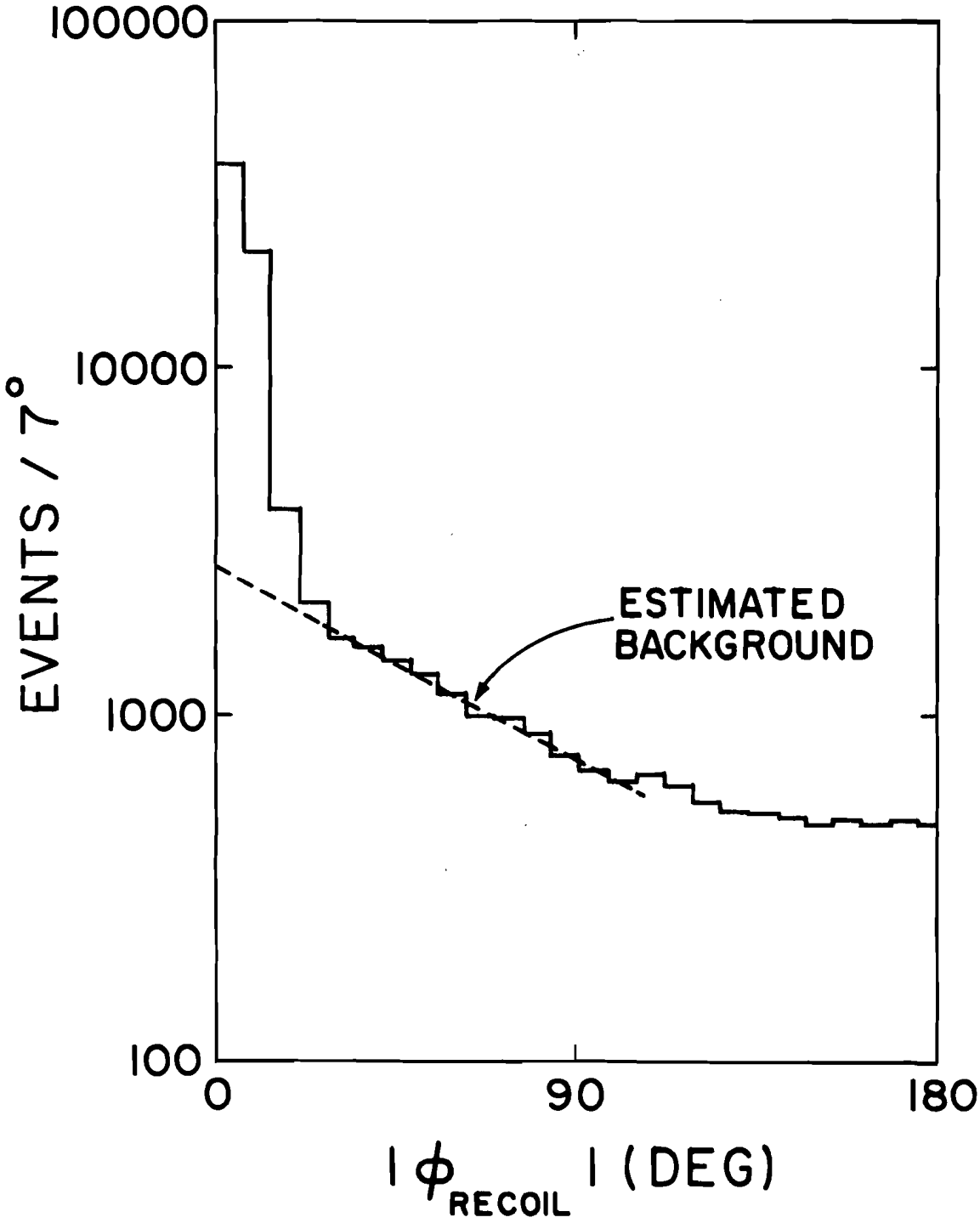
100000
10000
1000
100
EVENTS / 7°
ESTIMATED
BACKGROUND
0
90
180
| φ RECOIL | (DEG)

Figure 18

(d) Target-Empty Correction

During the experiment, some special runs were taken with all gas evacuated from the hydrogen target. This data could then be subtracted from the normal data to correct for interactions occurring in material other than the high pressure gas. When normalized to the same incident neutron flux, the target empty correction was found to be less than 0.3%. In addition, because the distributions of kinematic variables were very similar for target-empty and for target full, the net effect of this correction was completely negligible. One interesting aspect of the target-empty data is the distribution of the z coordinate of the $\pi^- p$ production vertex (Fig. 19). In contrast with the smooth distribution obtained for the target full data, the target empty events exhibit two peaks corresponding to the locations of the veto and trigger counters within the gas target.

3. Summary

In summary, the total background correction was accomplished by first removing events with improper pulse heights in the recoil counters, then events having $t < 0.02$ GeV^2 and finally data with recoil angles of magnitude greater than 28°. A weight, W, was then defined as

$$W = W_{geom} \cdot W_{cal} \cdot W_{\phi}$$

and assigned to all remaining events. In this expression, W_{geom} was the weight calculated to correct for the geometric efficiency.

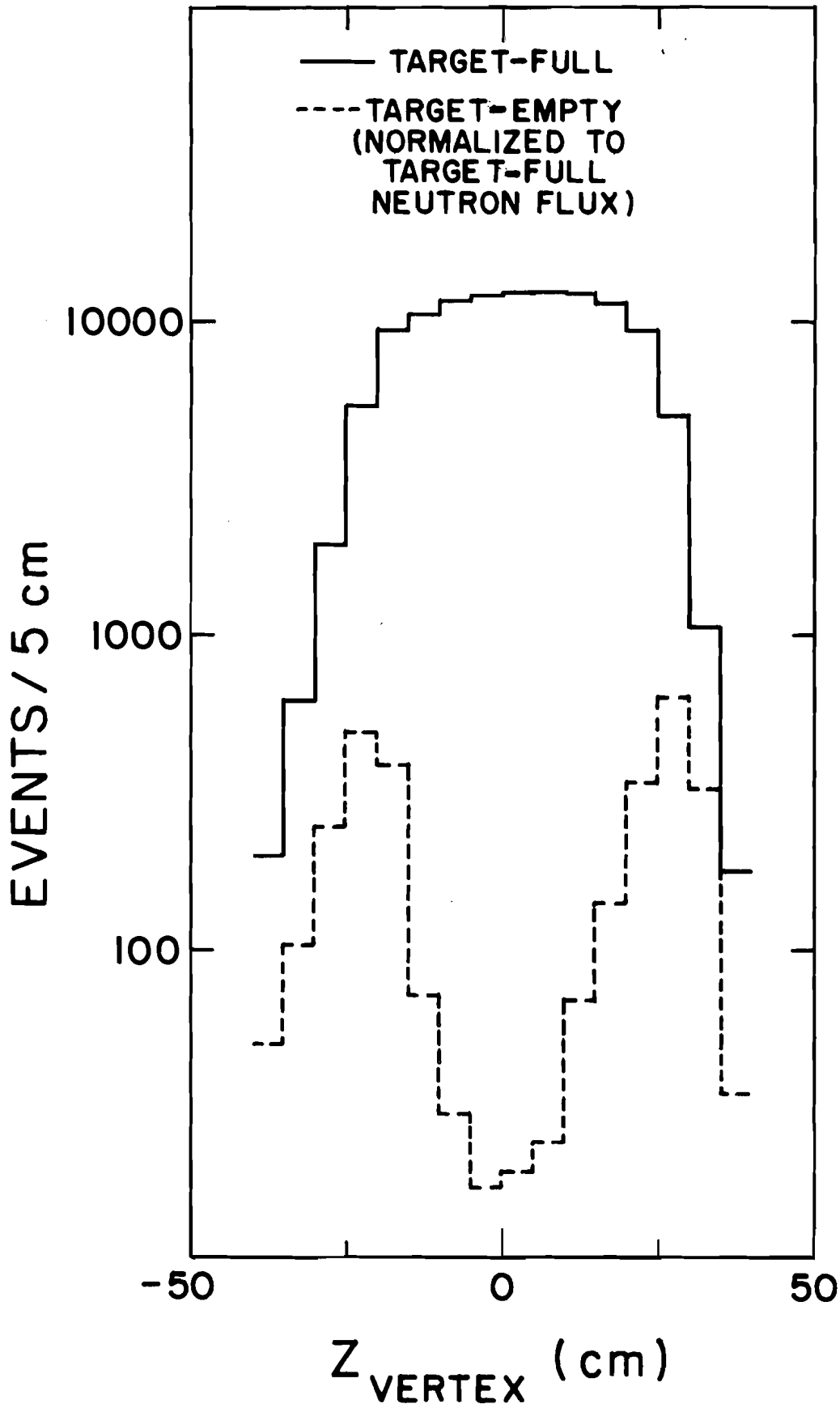
TARGET-FULL
TARGET-EMPTY
(NORMALIZED TO
TARGET-FULL
NEUTRON FLUX)
10000
1000
100
EVENTS / 5 cm
-50
0
50
Z VERTEX (cm)

Figure 19

W_{cal} was equal to 1 except for events having large pulse heights in the calorimeter. For such events W_{cal} was set negative so as to subtract the background on a statistical basis, for those events with large calorimeter pulse heights for which calorimeter information was not available. W_ϕ was set to -1.2 for events in the background region of recoil angles ($14° < |\phi_{recoil}| < 28°$). Within the signal region of recoil angles ($|\phi_{recoil}|<14°$) W_ϕ was a positive quantity used to correct for losses from the signal region due to experimental error in the recoil angle. The average weight per event was 2.0. The data sample consisted of a signal of approximately 60,000 events and a background of approximately 10,000 events.

D. Cross Section

1. Preliminary Normalization

A preliminary cross section for our reaction was determined using the formula

$$\sigma(\mu b) = 10^{30} \cdot N_{events} \cdot f$$

$$f \equiv \frac{1}{N_{neutrons} \cdot n}$$

where the factor of 10^{30} converted from square centimeters to microbarns, N_{events} was the final weighted number of events, $N_{neutrons}$ was the total number of neutrons incident upon the target as determined by the calorimeter, and n was the number of target

protons/cm^2. Because data was accumulated using two different target prossures (1250 and 750 p.s.i.), the value used for f in the calculation was a weighted average of the results from the two individual pressures (Table I). Two corrections were included at this point in the calculation. The first of these was a 10 ± 3% correction for losses due to reconstruction inefficiency. Another correction of 10 ± 3% was made to account for the fact that events with neutron momenta below 50 GeV/c were not used as data but were counted in the calorimeter.

The preliminary cross section integrated over the entire beam momentum spectrum, was 221 ± 15 μb. The error on this value inclused an estimated 5% uncertainty in our knowledge of the incident neutron flux. Two other important corrections to the above cross section are discussed below.

2. Further Corrections

(a) Region of Negligible Geometric Acceptance

This correction was necessitated by the fact that there were regions of very low geometric efficiency (discussed in section B of this chapter). The events affected by this problem were principally at low momentum, high mass, and at $\cos\theta_{GJ} > 0$. The preliminary cross section, as a function of momentum, for four mass regions, is shown in Fig. 20a[6]. At small mass, the cross section is nearly constant while at high mass it rises in an approximately linear fashion with increasing momentum. The relatively strong momentum-dependence observed at high mass was attributed to event

TABLE I

Details of Calculation of the Cross Section

Quantity	Pressure 1250 p.s.i.	750 p.s.i.
Target gm/cm^2	.342	.210
n	2.06×10^{23}	1.26×10^{23}
$N_{neutrons}$	1.52×10^{9}	4.82×10^{9}
f	3.20×10^{-33}	1.64×10^{-33}
$N_{triggers}$	1.11×10^{3}	2.75×10^{3}

$$\bar{f} = \frac{(N_{triggers})_{1250} \cdot f_{1250} + (N_{triggers})_{750} \cdot f_{750}}{(N_{triggers})_{1250} + (N_{triggers})_{750}}$$

$$= \frac{1.11 \times 10^{3} \cdot 3.20 \times 10^{-33} + 2.75 \times 10^{3} \cdot 1.64 \times 10^{-33}}{1.11 \times 10^{3} + 2.75 \times 10^{3}}$$

$$= 2.09 \times 10^{-33}\ cm^2$$

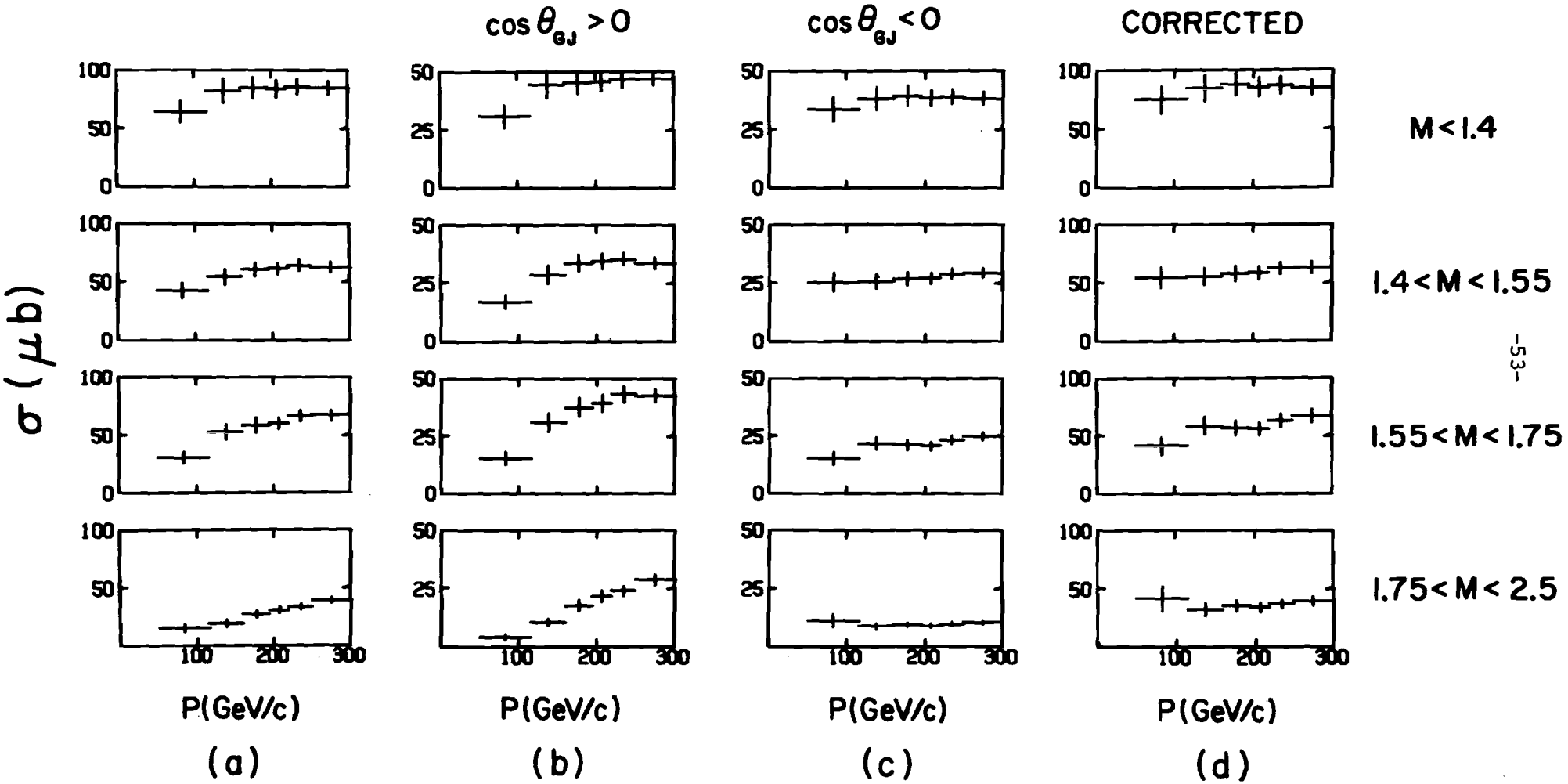
cos θ_GJ > 0
cos θ_GJ < 0
CORRECTED
σ (μb)
M<1.4
1.4<M<1.55
1.55<M<1.75
1.75<M<2.5
P(GeV/c)
(a)
(b)
(c)
(d)

Figure 20

losses in the problematic region of our acceptance. Further evidence that geometric inefficiencies were involved was obtained by examining separately, the cross sections for $\cos\theta_{GJ} < 0$ and $\cos\theta_{GJ} > 0$ (Figs. 20b and 20c). At negative values for $\cos\theta$, where there were no problems with acceptance, the cross section is flat for all masses, whereas for positive $\cos\theta$, the region of possible losses, there is an accentuated momentum dependence.

Corrections for the losses at $\cos\theta_{GJ} > 0$ were made as follows. Because in regions of good acceptance, the cross section displayed only a weak variation with momentum, we assumed that the $\cos\theta_{GJ}$ distribution was also energy independent. We therefore estimated the total cross section by dividing the results for $\cos\theta_{GJ} < 0$ by the ratio of the cross section for $\cos\theta_{GJ} < 0$ to the cross section for all $\cos\theta_{GJ}$ as determined from the highest values of beam momentum. Figure 20d gives the resulting corrected cross sections.

To minimize the effect of losses at low momentum on the rest of the analysis, the data sample was subjected to a further cut off. In particular, the minimum allowed value of momentum for data to be acceptable was taken to be an increasing function of mass (Fig. 21a). This cut eliminated that portion of the data containing significant losses. Assuming the dissociation process to be nearly momentum independent, the fraction of the data that survived the momentum cut can be approximated by the fraction of the incident neutron beam-momentum spectrum above the cut off (see lower part of Fig.21a). The inverse of this fraction is the weight needed to correct for

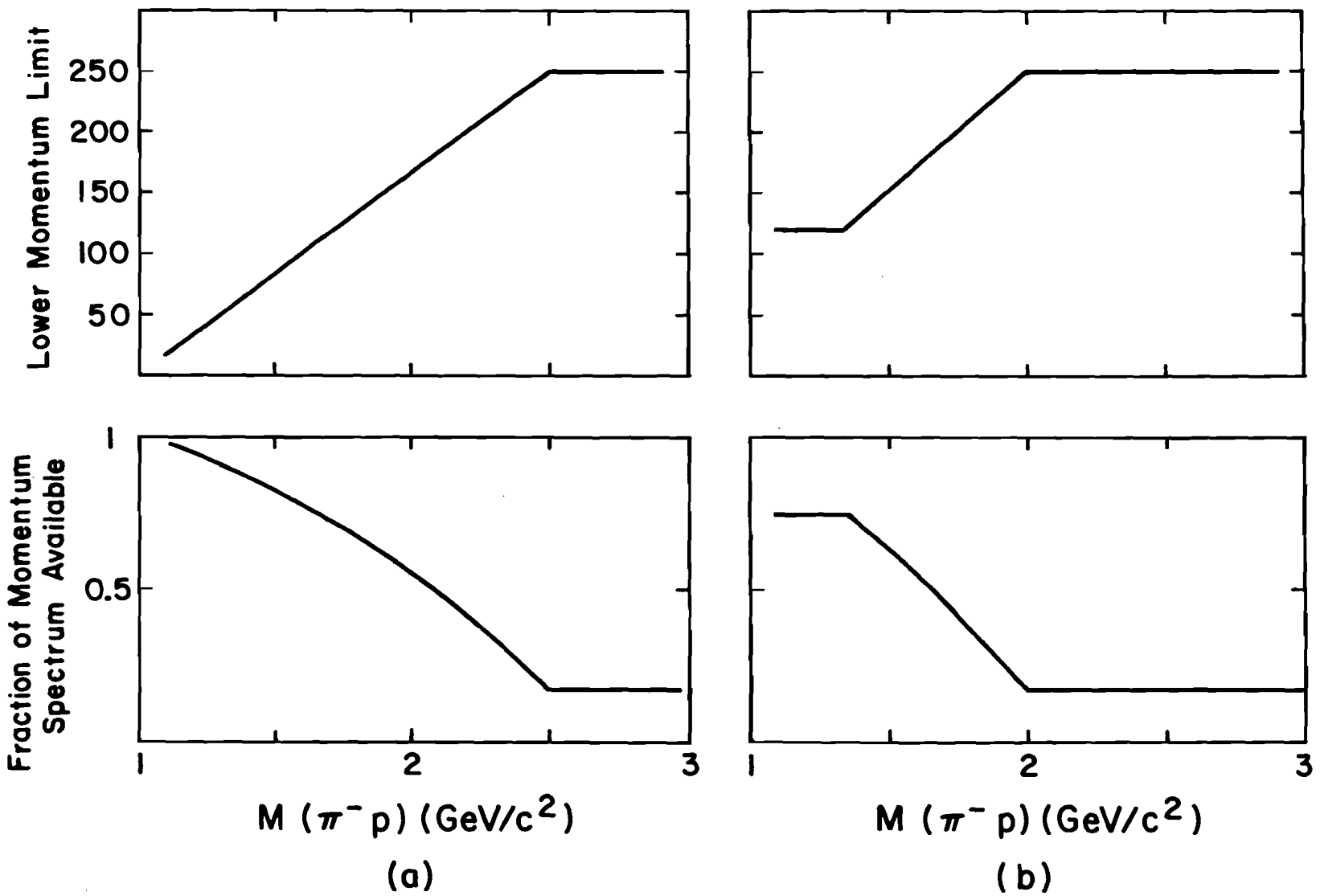
Lower Momentum Limit
250
200
150
100
50
Fraction of Momentum Spectrum Available
1
0.5
1
2
3
M (π^- p) (GeV/c^2)
(a)
1
2
3
M (π^- p) (GeV/c^2)
(b)

Figure 21

the low-momentum cut-off imposed on the data. The same procedure, but with a more restrictive low-momentum cut-off was used for calculating the more sensitive moments of the spherical harmonics in (θ_{GJ}, ϕ_{GJ}). The cut offs used for the calculation of moments are displayed in Fig. 21b. The moments are discussed in Chapter IV, Section D of this thesis.

(b) Events with $t<.02$ GeV^2

A final correction to the cross section was made for those events with a t value below .02 GeV^2. This was done by extrapolating the observed t distribution to t=0. A more detailed discussion of this calculation will be given in the next chapter.

(c) Final Cross Sections

Table II shows our final cross sections. The data indicate approximate momentum independence of the cross section for momenta between 50 GeV/c and 300 GeV/c.

TABLE II

Final Cross Sections

Momentum interval (GeV/c)	Mean momentum (GeV/c)	$\sigma(\mu b)$		
50 - 115	85	260	±	39
115 - 160	140	282	±	38
160 - 195	180	289	±	35
195 - 220	208	285	±	32
220 - 250	235	299	±	31
250 - 300	265	304	±	29
50 - 300	200	287	±	22

CHAPTER IV

PRESENTATION OF RESULTS

This chapter contains a detailed presentation of our experimental results. Primary emphasis will be placed on differential cross sections in t, M, $\cos\theta_{GJ}$ and ϕ_{GJ}. Comparison with other experiments as well as with theory, will be made in the following chapter.

A. General Features

The overall weighted distributions in t, M, $\cos\theta_{GJ}$, ϕ_{GJ}, $\cos\theta_H$ and ϕ_H are displayed in Fig. 22. The t distribution is exceedingly steep at small t values, and less so at larger t. $d\sigma/dM$ is characterized, primarily, by a broad low-mass enhancement. In addition, there are peaks at masses of approximately 1.38, 1.48 and 1.65 GeV/c^2, followed by a smooth high mass tail beyond 1.8 GeV/c^2. The distribution in $\cos\theta_{GJ}$ shows a strong forward, and a smaller backward, peak, while the corresponding $\cos\theta_H$ plot is nearly flat with a pronounced minimum in the forward direction. (The detailed nature of this minimum, however, occurs in the region of worst acceptance and is consequently somewhat sensitive to our weighting procedures.) Both the ϕ_{GJ} and the ϕ_H distributions have maxima at ±180 degrees, and the ϕ_H cross section has a small additional peak at zero. Both ϕ

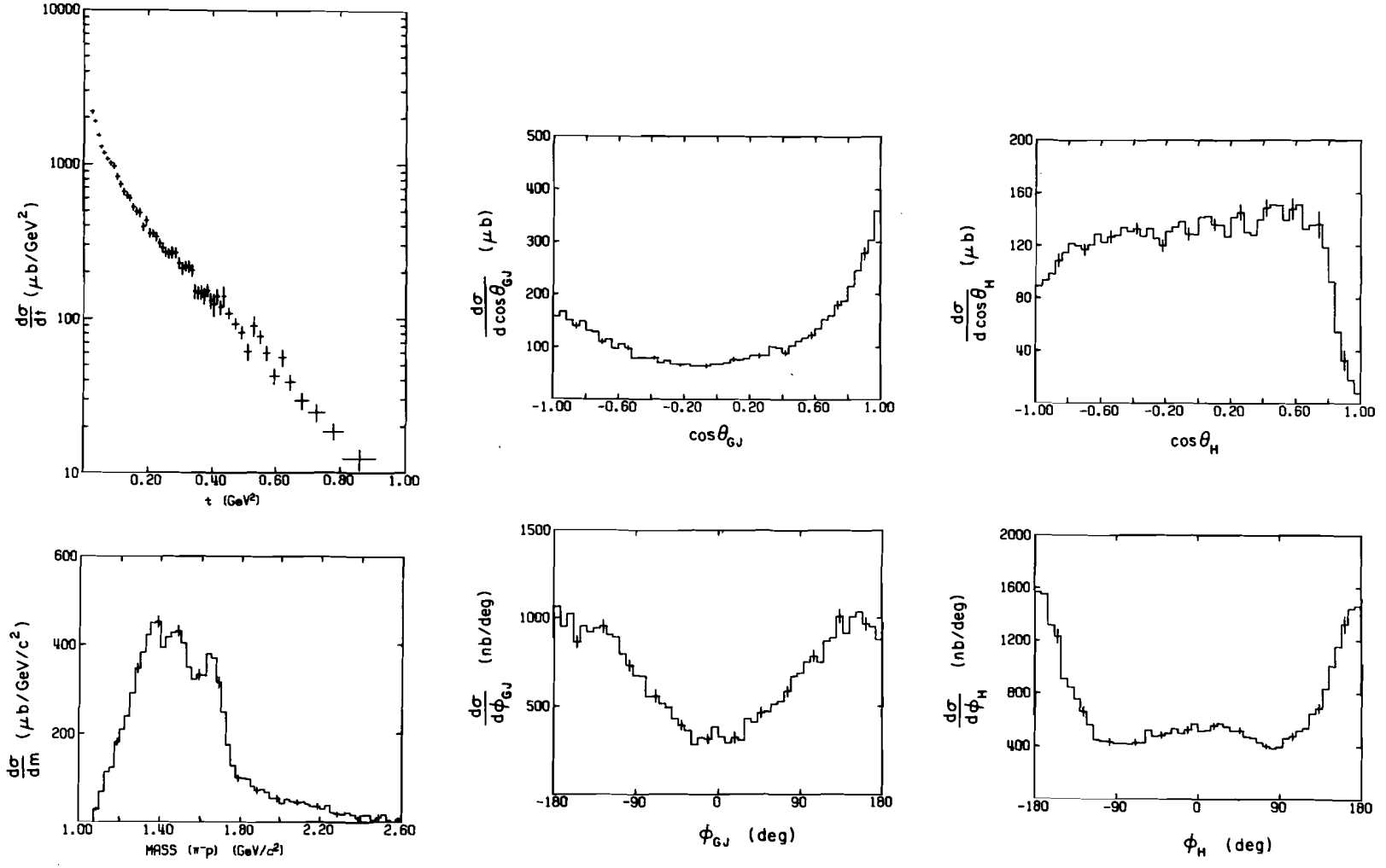
$\frac{d\sigma}{dt}$ (μb/GeV^2)
t (GeV^2)
$\frac{d\sigma}{d\cos\theta_{GJ}}$ (μb)
$\cos\theta_{GJ}$
$\frac{d\sigma}{d\cos\theta_H}$ (μb)
$\cos\theta_H$
$\frac{d\sigma}{dm}$ (μb/GeV/c^2)
MASS (π^-p) (GeV/c^2)
$\frac{d\sigma}{d\phi_{GJ}}$ (nb/deg)
ϕ_{GJ} (deg)
$\frac{d\sigma}{d\phi_H}$ (nb/deg)
ϕ_H (deg)

Figure 22

distributions are symmetric about the origin, as is required by parity conservation (assuming an unpolarized beam of neutrons). For this reason, all further discussion of these variables can be limited to their absolute values. In the succeeding sections of this chapter we examine the data in greater detail.

B. Distributions in Momentum Transfer

1. Mass Dependence

Our data show a strong variation of $d\sigma/dt$ with the mass of πp system. In Fig. 23, t distributions are presented for eight mass intervals from threshold to 2 GeV/c^2. For the higher-mass regions $d\sigma/dt$ is, with the exception of a possible turn over at small t, well approximated over the entire range of t values by a simple exponential. The data below a mass of about 1.5 GeV/c^2 show more structure. At very small values of t the behavior is again exponential but with a dependence that becomes invreasingly steeper as smaller masses are selected. There is an abrupt change in the shape near 0.2 GeV^2, after which the low-mass data appear to fall off in t at a rate comparable to that observed for the data at high mass.

Fits to $d\sigma/dt$ were made using the parameterization $d\sigma/dt=Ae^{-bt}$. The use of this parameterization is quite common in the study of our reaction and we will subsequently refer to b as the "slope parameter" of the t distribution. At small-mass values the upper limit of the t interval over which the fit was performed was carefully chosen to include only those values of t that were well approximated by a

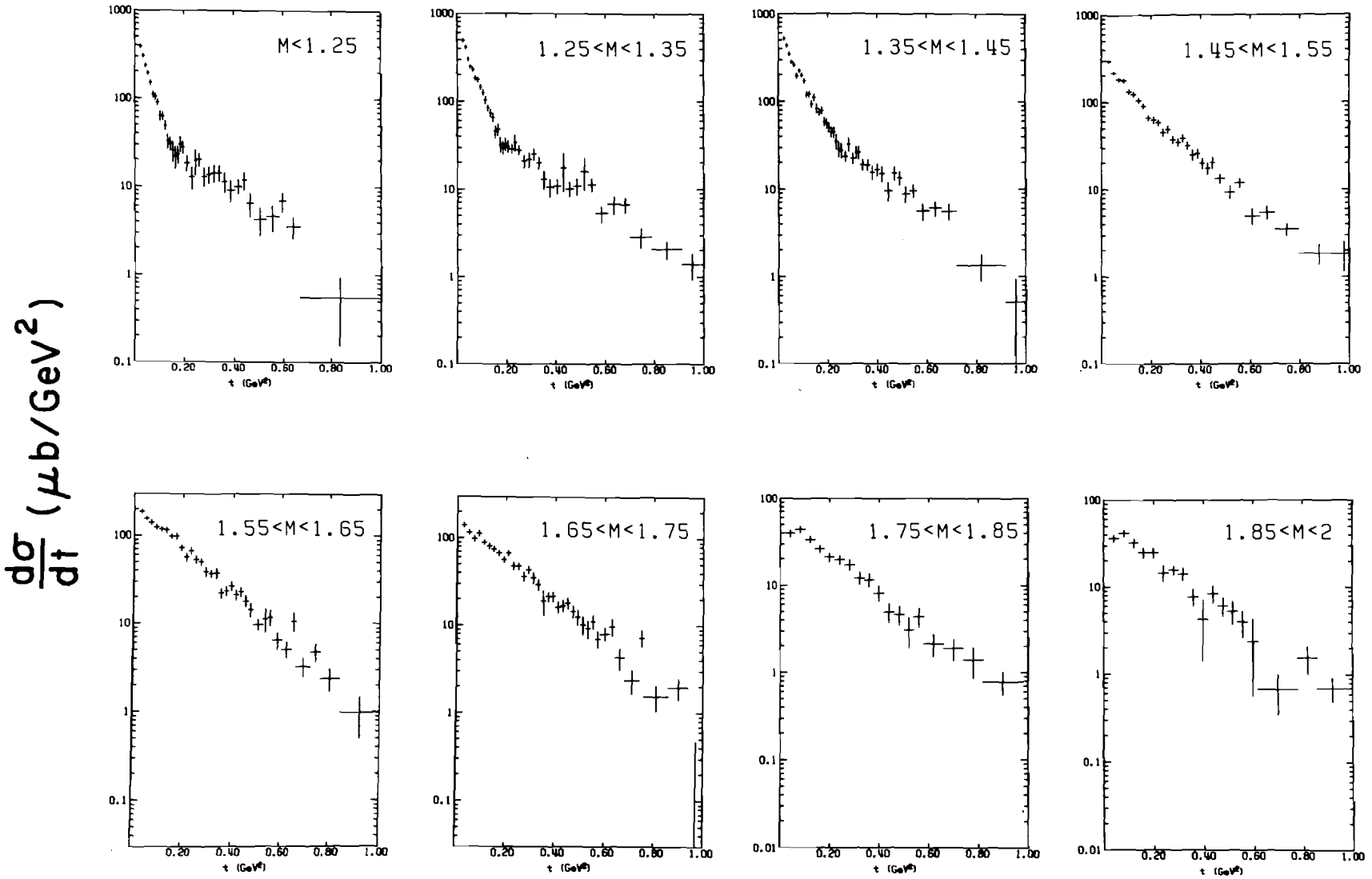
$\frac{d\sigma}{dt}$ (μb/GeV^2)
M<1.25
1.25<M<1.35
1.35<M<1.45
1.45<M<1.55
1.55<M<1.65
1.65<M<1.75
1.75<M<1.85
1.85<M<2
t (GeV²)

Figure 23

simple exponential. The results of the fits are listed in Table III, and plotted in Fig. 24. Starting with a slope of about 25 GeV^{-2} at small M, a value approximately twice that observed for proton-proton elastic scattering[7], b drops steadily as the mass increases. Although the dependence on mass is nearly linear, the rate of decline seems to decrease between 1.25 and 1.4 GeV/c^2, and then to increase again for masses just above this interval. The slope parameter appears to be constant, $\sim$5 GeV^{-2}, for masses greater than 1.6 GeV/c^2.

As mentioned in Section D of the previous chapter, a correction was made to the cross sections for events with a value of t too small to be detected by our apparatus (t values below .02 GeV^2). This was done using the fits given in Table III, and extrapolating the data to t=0. The resulting corrections are summarized in Table IV. The statistical errors given in Table IV are based on the errors in the fit parameters and consequently do not include the effects of possible nonexponential behavior for $d\sigma/dt$ at t values below .02. A more realistic estimate of the error for the total correction is therefore provided in the table to take account of such systematic uncertainties.

2. Momentum Dependence

Using the exponential parameterization of the previous section, the momentum dependence of the t-distribution was also investigated. The lower momentum cut off as a function of mass, described in the previous chapter, could not be used in this study, so the investigation was limited to low masses, where biases were minimal. Figure 25

Table III

Fits to differential cross sections [exp(-bt)]

Mass interval (GeV/c^2)	t range for fit (GeV^2)	$b(GeV^{-2})$
< 1.165	.03 - .15	24.4 ± 1.6
1.165 - 1.25	.03 - .15	19.2 ± 0.9
1.25 - 1.3	.03 - .15	16.8 ± 0.9
1.3 - 1.35	.03 - .15	16.0 ± 0.7
1.35 - 1.4	.03 - .15	15.0 ± 0.65
1.4 - 1.45	.03 - .15	11.2 ± 0.8
1.45 - 1.5	.03 - .19	8.8 ± 0.6
1.5 - 1.55	.03 - .19	6.3 ± 0.6
1.55 - 1.6	.03 - .49	6.1 ± 0.25
1.6 - 1.65	.03 - .49	5.1 ± 0.2
1.65 - 1.7	.03 - .49	5.1 ± 0.2
1.7 - 1.75	.03 - .49	5.1 ± 0.3
1.75 - 1.85	.03 - .44	4.8 ± 0.4
1.85 - 2.0	.03 - .44	4.6 ± 0.4

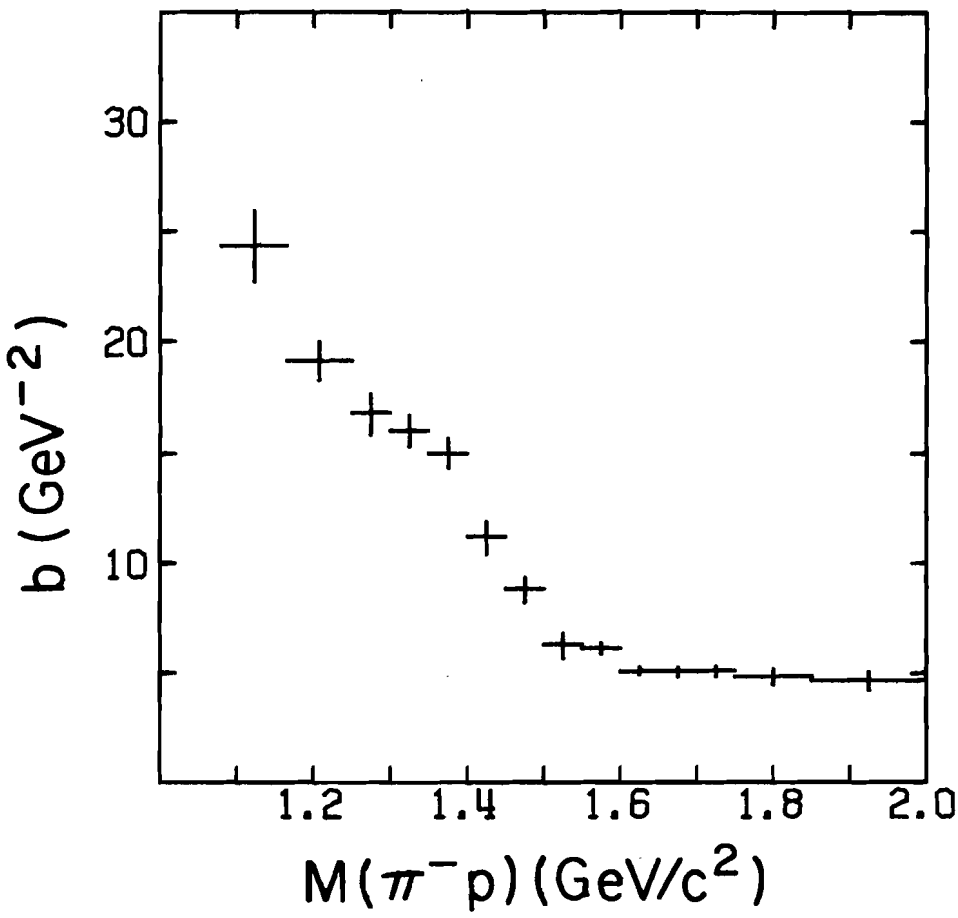

Figure 24

Table IV

Correction to cross sections for losses below $t = .02\ GeV^2$

$$\frac{d\sigma}{dt} \simeq a(M)e^{-b(M)t} \quad \text{for small } t$$

$$\sigma[t_1;t_2] = \int_{t_1}^{t_2} \left(\frac{d\sigma}{dt}\right)dt \simeq \frac{a(M)}{b(M)}\left(e^{-bt_1} - e^{-bt_2}\right)$$

$$\sigma[0;.02] \simeq \frac{a(M)}{b(M)}\left(1 - e^{-.02b}\right)$$

Mass interval (GeV/c^2)	$a(\mu b/GeV^2)$	$b(GeV^{-2})$	$\sigma(\mu b)^{\dagger}$
$M < 1.165$	204	24.4	3.2 ± 0.4
1.165 - 1.25	399	19.2	6.6 ± 0.5
1.25 - 1.3	305	16.8	5.2 ± 0.5
1.3 - 1.35	365	16.0	6.3 ± 0.4
1.35 - 1.4	392	15.0	6.8 ± 0.5
1.4 - 1.45	252	11.2	4.5 ± 0.4
1.45 - 1.5	200	8.8	3.8 ± 0.3
1.5 - 1.55	129	6.3	2.4 ± 0.3
1.55 - 1.6	114	6.1	2.2 ± 0.1
1.6 - 1.65	105	5.1	2.0 ± 0.1
1.65 - 1.7	99	5.1	1.9 ± 0.1
1.7 - 1.75	60	5.1	1.2 ± 0.1
1.75 - 1.85	58	4.8	1.1 ± 0.1
1.85 - 2	54	4.6	1.0 ± 0.1
2 - 3	62	3.1	1.2 ± 0.2
		Total	49.2 ± 1.2 μb

†Errors are statistical. To correct for the presence of systematics we estimate a final correction of 49 ± 16 μb.

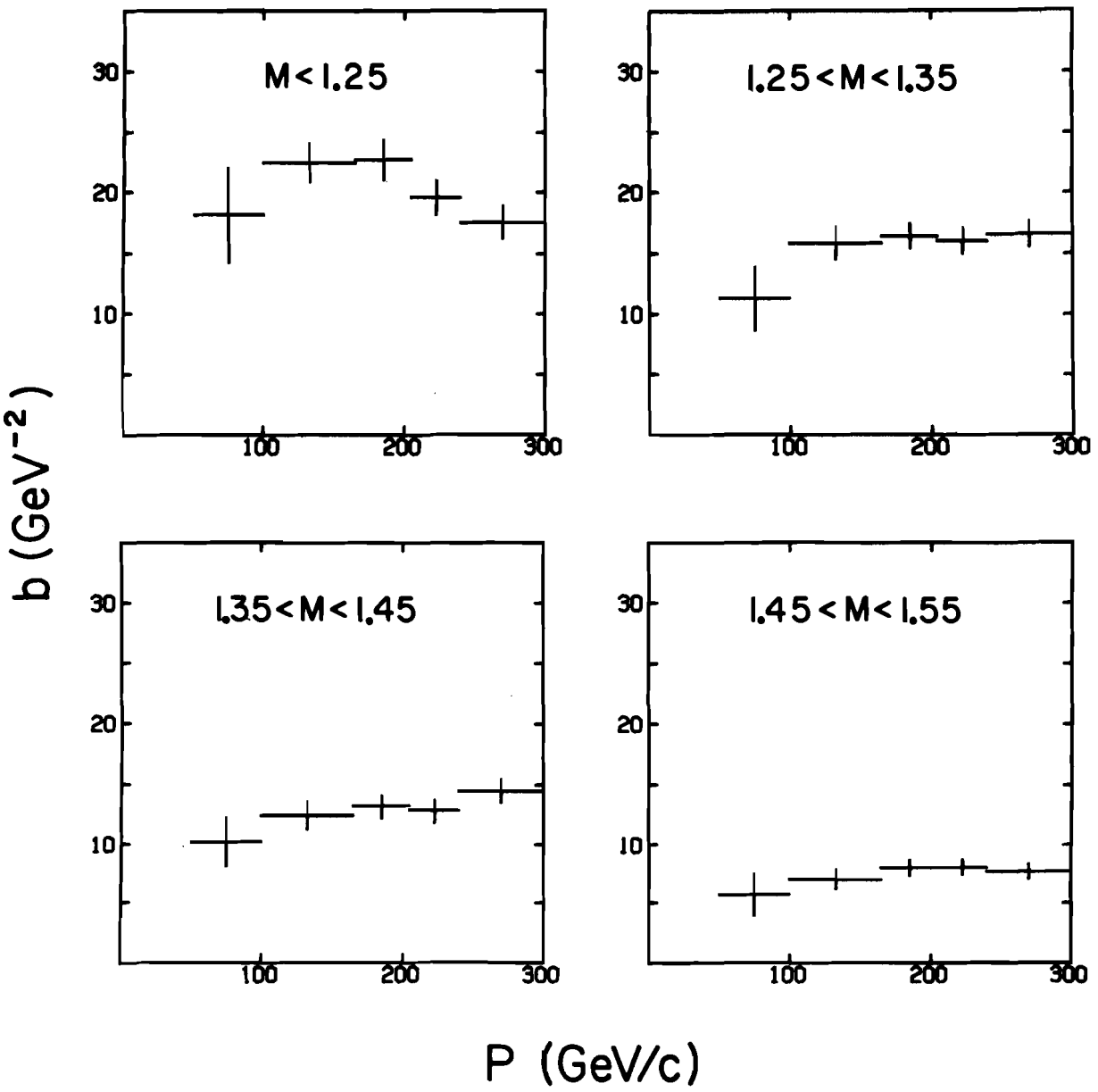
M<1.25
1.25<M<1.35
1.35<M<1.45
1.45<M<1.55
30
20
10
100
200
300
b (GeV^{-2})
P (GeV/c)

Figure 25

and Table V summarize the results. All mass intervals, except the very lowest one, show a small possible increase in b over our beam-momentum range. The weak momentum dependence observed here serves further to justify the presentation of our other results in terms of averages over incident momenta.

3. Decay-Angle Dependence

When the data were examined to determine the variations of $d\sigma/dt$ with the decay angles of the πp system, a striking effect was observed. The t distribution was very insensitive to cuts in ϕ_{GJ}, but was a strong function of θ_{GJ}. As can be seen in Figs. 26-28, the break in $d\sigma/dt$ which occurs at smaller masses is greatly enhanced for central values of $\cos\theta_{GJ}$, while data having very large absolute values of $\cos\theta$ show no break at all. For larger mass values, where the overall t distribution is approximately exponential, there is much less variation with $\cos\theta$. All three mass intervals show a low-t turn over in $d\sigma/dt$ at large values of $\cos\theta$. We will show in the next chapter that some of this behavior can be explained in terms of a specific diffraction-production model.

Figure 29 shows the observed dependence of the slope parameter on $\cos\theta_{GJ}$ and $|\phi_{GJ}|$ for the same three mass intervals studied in Figs. 26-28. This plot confirms the weak dependence of $d\sigma/dt$ on $|\phi_{GJ}|$, and provides a quantitative measure of the dramatically different values for slopes found for different regions of $\cos\theta_{GJ}$. The small changes of b with $|\phi_{GJ}|$ can be attributed to the known correlation in our data between $\cos\theta_{GJ}$ and ϕ_{GJ}, which will be

Table V

Slope parameter as a function of mass and incident momentum

Mass interval (GeV/c^2)	Momentum interval (GeV/c)	t range for fit (GeV^2)	$b(GeV^{-2})$
	50 - 100		18.2 ± 3.9
	100 - 165		22.5 ± 1.6
1.25 <	165 - 205	.03 - .15	22.7 ± 1.6
	205 - 240		19.6 ± 1.4
	240 - 300		17.5 ± 1.4
	50 - 100		11.3 ± 2.6
	100 - 165		15.9 ± 1.3
1.25 - 1.35	165 - 205	.03 - .15	16.4 ± 1.0
	205 - 240		16.0 ± 1.0
	240 - 300		16.5 ± 1.0
	50 - 100		10.2 ± 2.1
	100 - 165		12.4 ± 1.1
1.35 - 1.45	165 - 205	.03 - .15	13.2 ± 1.0
	205 - 240		12.8 ± 1.0
	240 - 300		14.4 ± 1.0
	50 - 100		5.7 ± 1.7
	100 - 165		7.0 ± 0.8
1.45 - 1.55	165 - 205	.03 - .21	8.0 ± 0.7
	205 - 240		8.0 ± 0.7
	240 - 300		7.6 ± 0.7

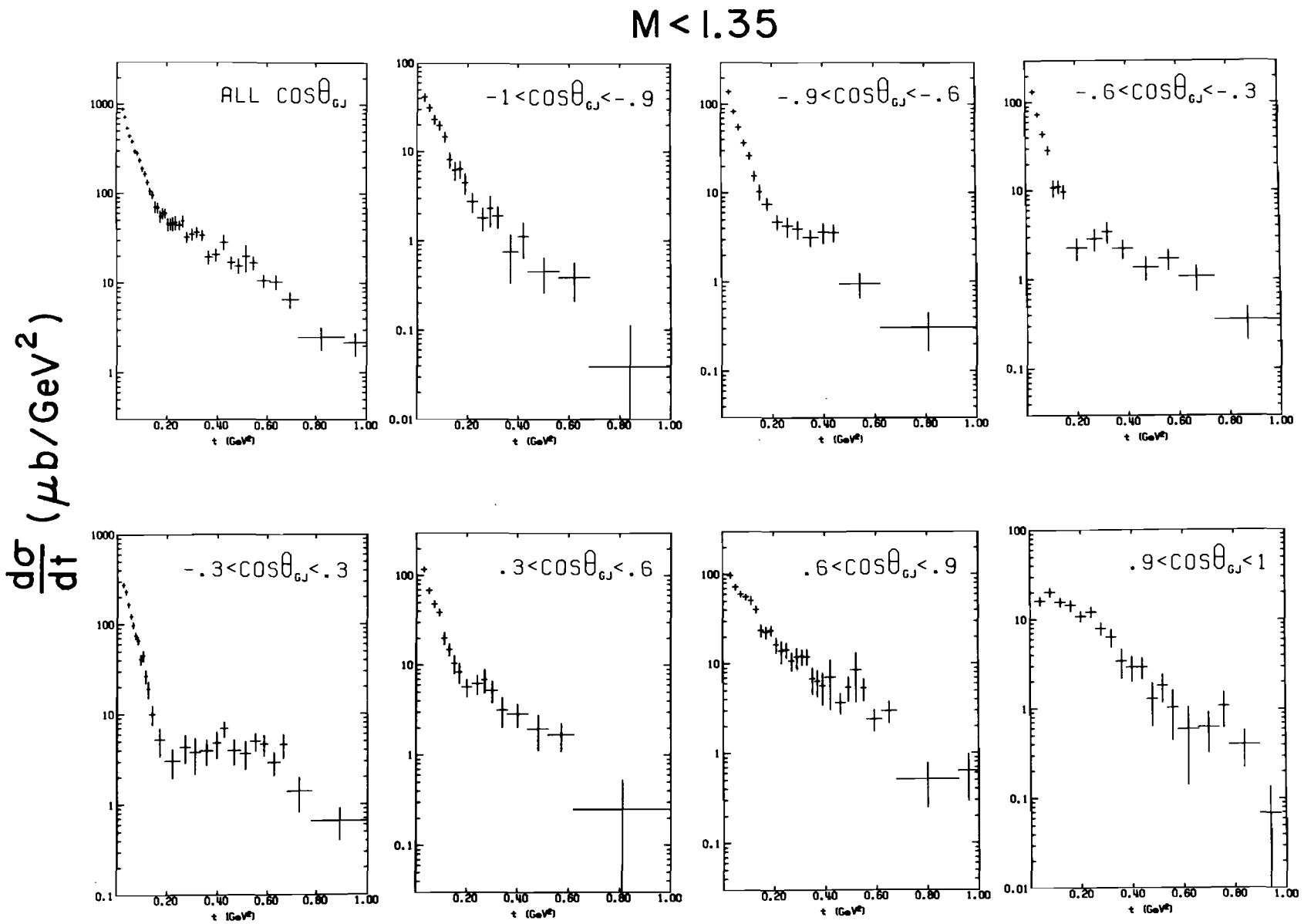
M<1.35
ALL cosθGJ
-1<cosθGJ<-.9
-.9<cosθGJ<-.6
-.6<cosθGJ<-.3
-.3<cosθGJ<.3
.3<cosθGJ<.6
.6<cosθGJ<.9
.9<cosθGJ<1
dσ/dt (μb/GeV²)
t (GeV²)

Figure 26

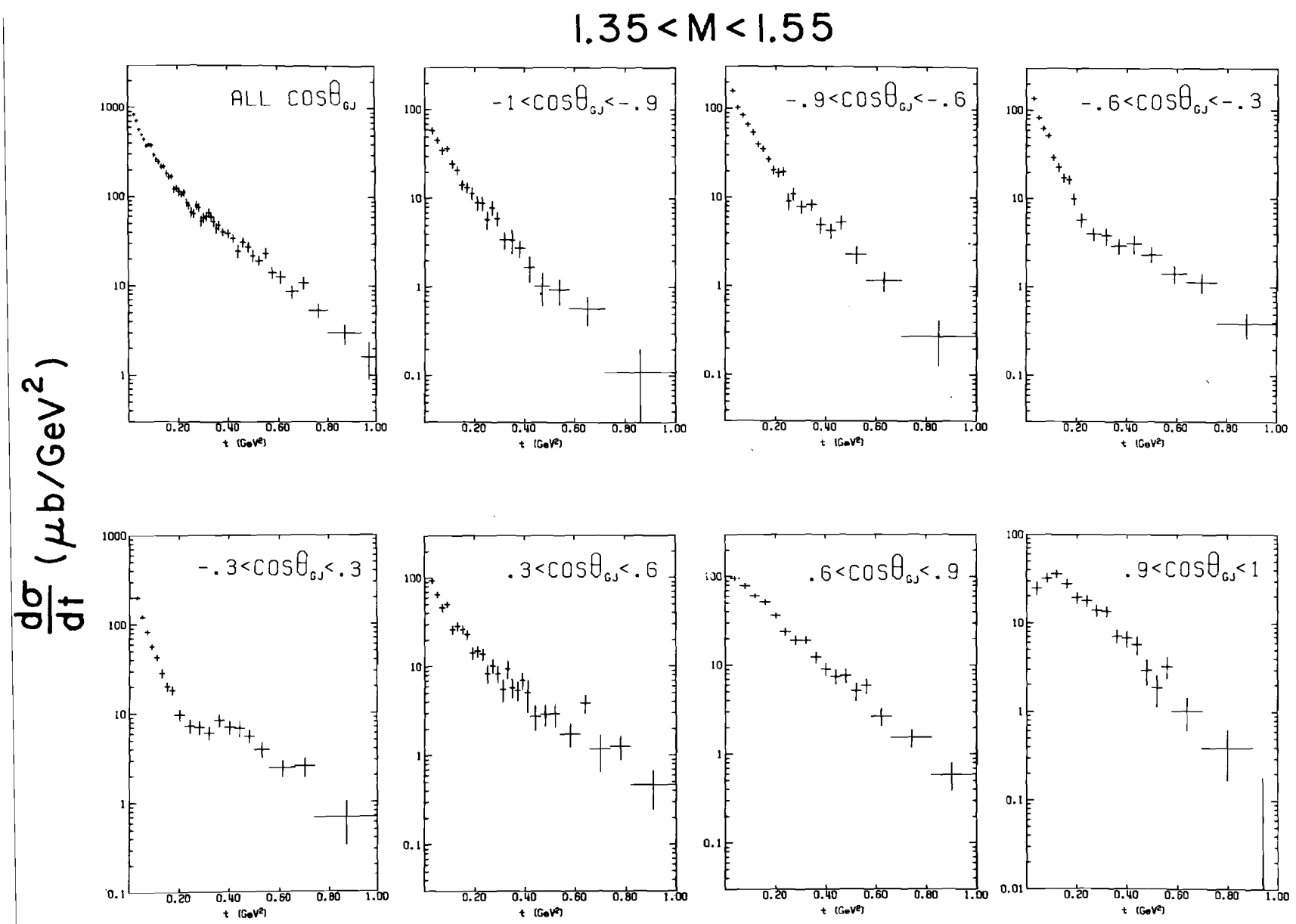
1.35<M<1.55
ALL cosθGJ
-1<cosθGJ<-.9
-.9<cosθGJ<-.6
-.6<cosθGJ<-.3
-.3<cosθGJ<.3
.3<cosθGJ<.6
.6<cosθGJ<.9
.9<cosθGJ<1
dσ/dt (μb/GeV²)
t (GeV²)

Figure 27

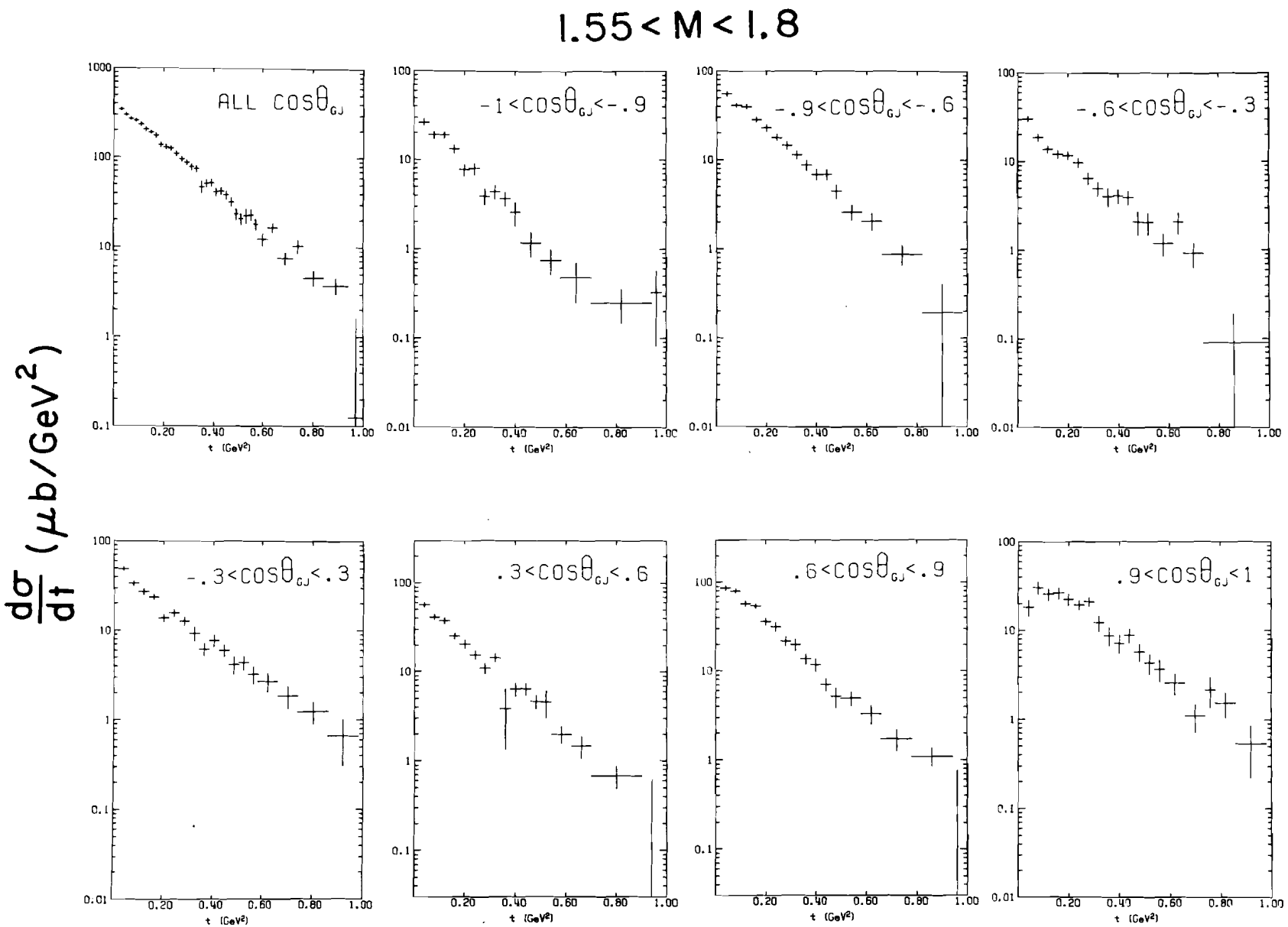
1.55 < M < 1.8
dσ/dt (μb/GeV²)
ALL cosθ_GJ
-1<cosθ_GJ<-.9
-.9<cosθ_GJ<-.6
-.6<cosθ_GJ<-.3
-.3<cosθ_GJ<.3
.3<cosθ_GJ<.6
.6<cosθ_GJ<.9
.9<cosθ_GJ<1
t (GeV²)

Figure 28

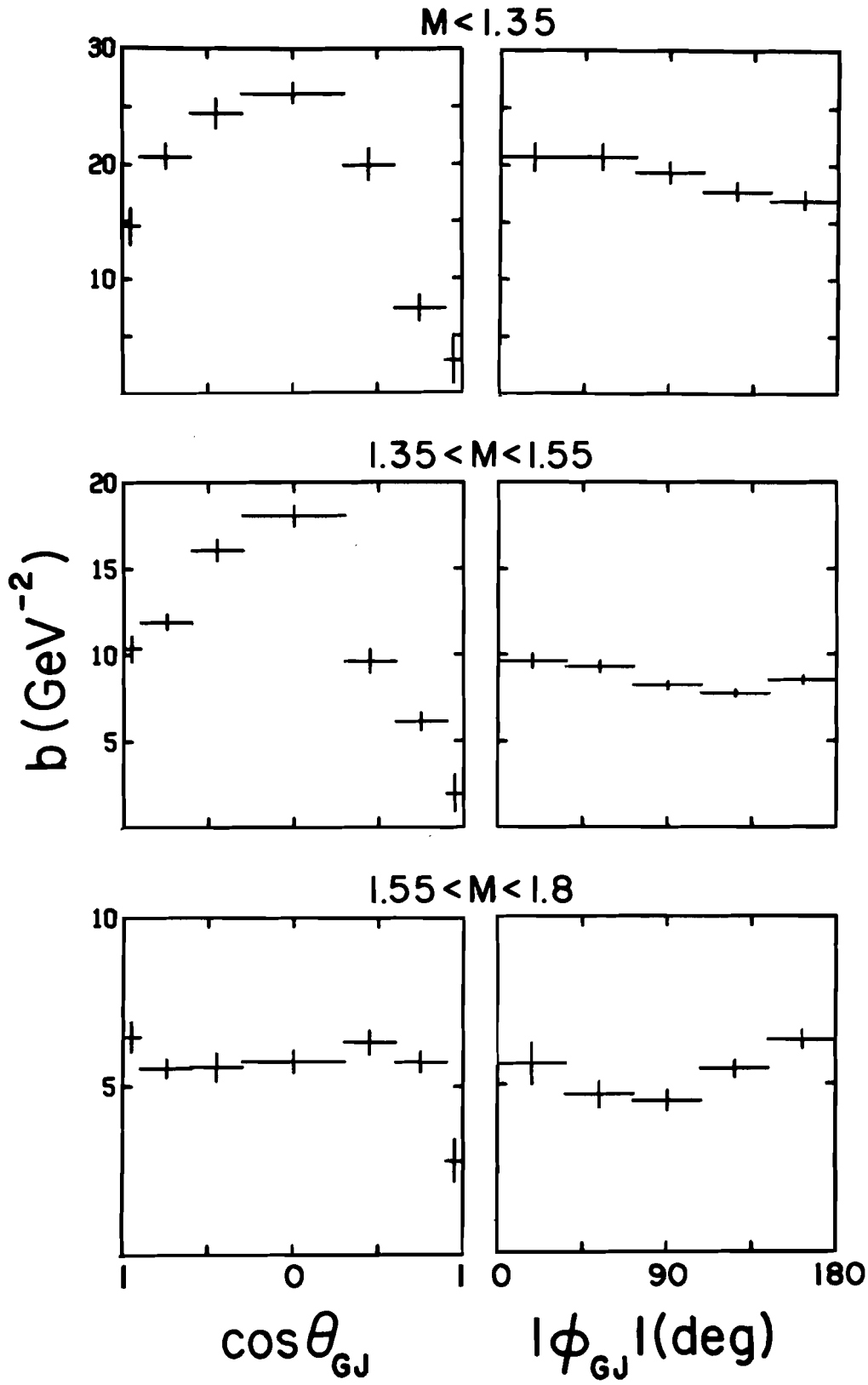
M<1.35
1.35<M<1.55
1.55<M<1.8
b (GeV^{-2})
30
20
10
20
15
10
5
10
5
1
0
1
0
90
180
$\cos\theta_{GJ}$
$|\phi_{GJ}|$(deg)

Figure 29

discussed later in this chapter.

A comparison between slope parameters using all decay angles, and data for $|\cos\theta_{GJ}| < .3$, is given in Fig. 30 as a function of mass. For central values of $\cos\theta_{GJ}$ the slope is about one and one half times larger than that for all the data, for masses up to 1.5 GeV/c^2. The b value for the restricted decay region then falls suddenly, and the two sets of data exhibit similar behavior above 1.6 GeV/c^2.

C. Mass Distributions

1. Dependence on t

The strong variation of $d\sigma/dt$ with mass is likewise reflected in the dependence of $d\sigma/dM$ upon t. Figure 31 displays the M distributions for six t regions. At low t the spectrum is dominated by a low-mass peak at approximately 1.4 GeV/c^2. As t is increased, the mean mass value also increases, and there is evidence for peaks at about 1.5 and 1.7 GeV/c^2.

2. Decay-Angle Dependence

Again as was the case with our t distributions, the mass spectra show interesting variations as a function of decay angles. Figure 32 illustrates the dependence of $d\sigma/dM$ on $\cos\theta_{GJ}$. There is a striking peak at 1.7 GeV/c^2 for large negative values of $\cos\theta$, which seems to provide the clearest evidence we have for the production of possible $\pi^- p$ resonant states. As $\cos\theta$ is increased, the production of this state at first diminishes rapidly and then,

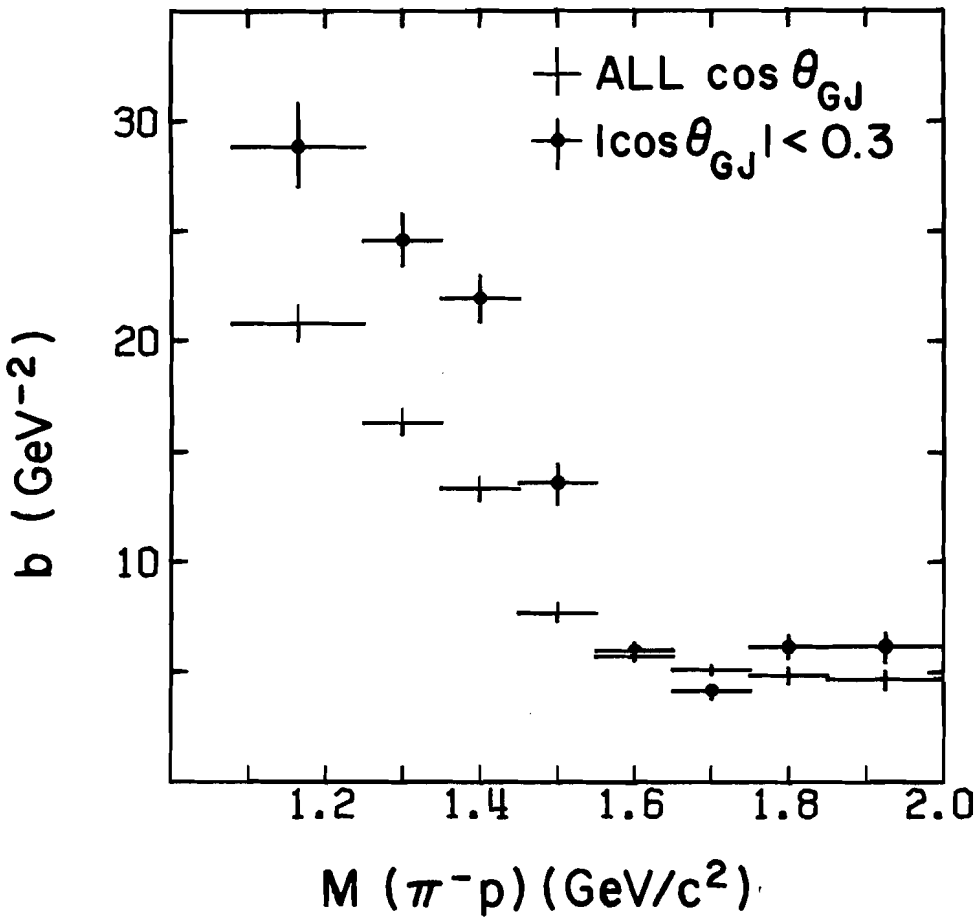

Figure 30

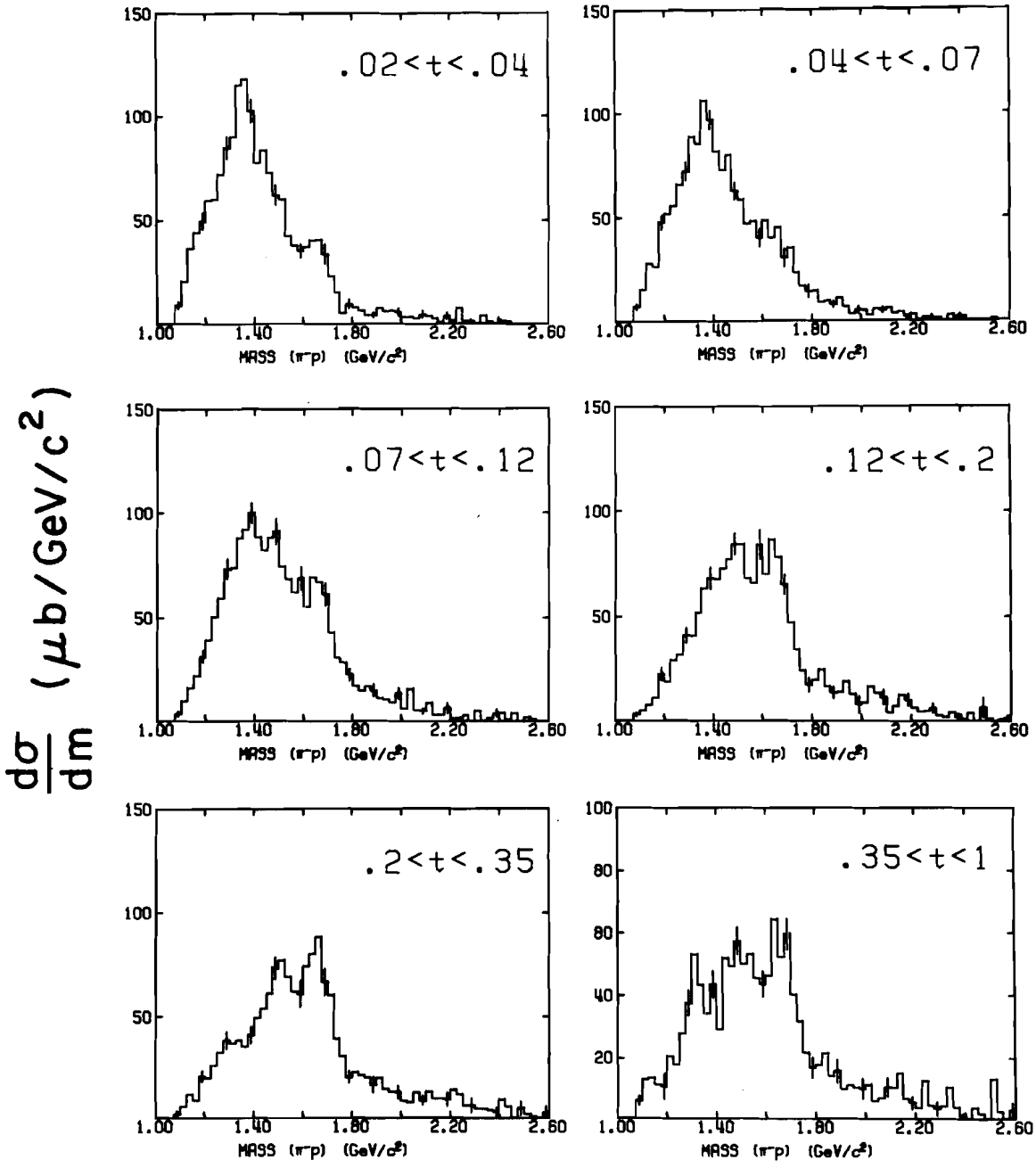
$\frac{d\sigma}{dm}$ (μb/GeV/c^2)
.02<t<.04
.04<t<.07
.07<t<.12
.12<t<.2
.2<t<.35
.35<t<1
MASS (π^-p) (GeV/c^2)

Figure 31

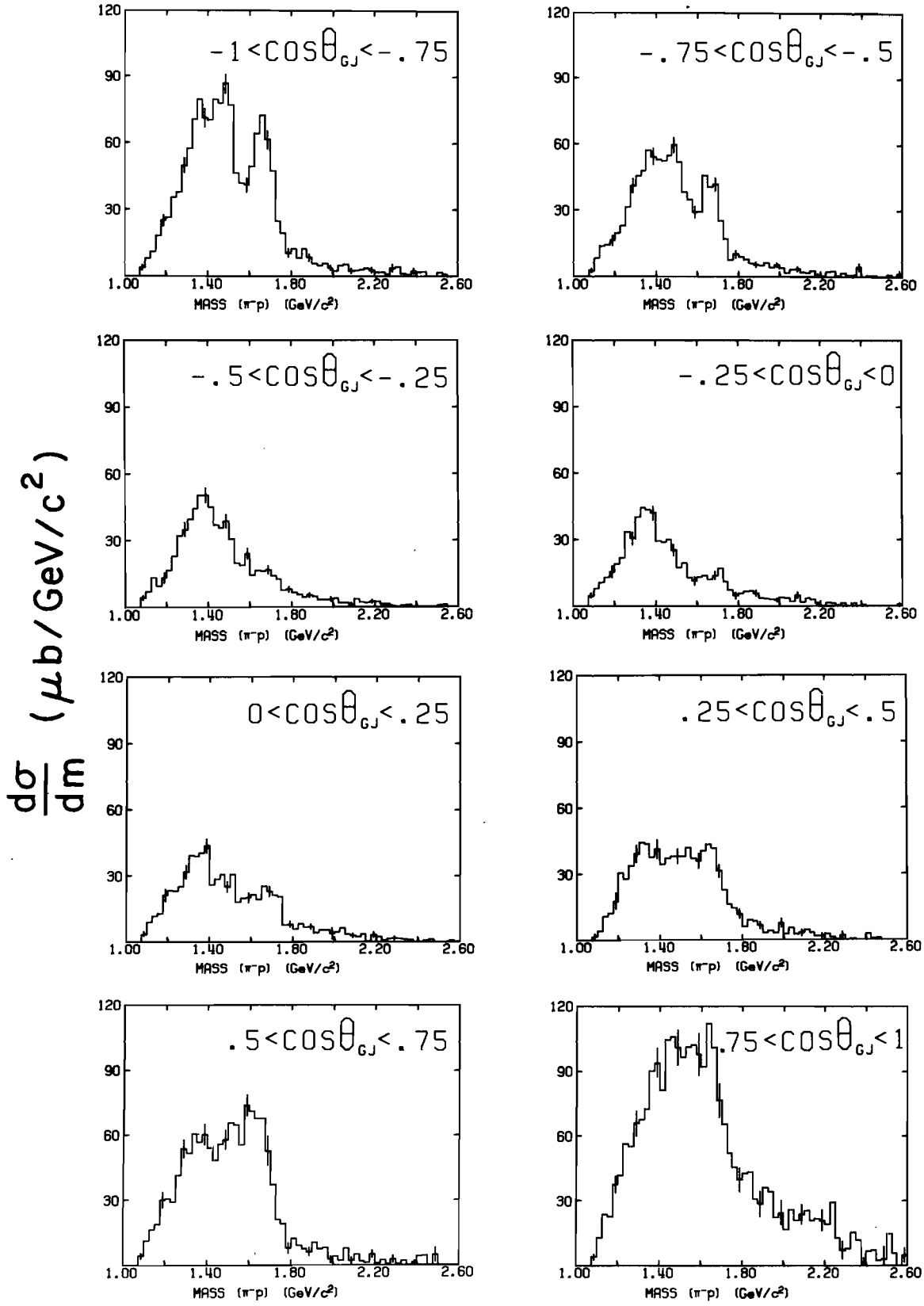
$\frac{d\sigma}{dm}$ (μb/GeV/c^2)
-1<cosθ_{GJ}<-.75
-.75<cosθ_{GJ}<-.5
-.5<cosθ_{GJ}<-.25
-.25<cosθ_{GJ}<0
0<cosθ_{GJ}<.25
.25<cosθ_{GJ}<.5
.5<cosθ_{GJ}<.75
.75<cosθ_{GJ}<1
MASS (π^-p) (GeV/c^2)
120
90
60
30
1.00
1.40
1.80
2.20
2.60

Figure 32

at larger positive $\cos\theta$, the peak appears again, although not as clearly as at $\cos\theta < 0$. It is also evident from this figure that there is a large increase in the cross section at very large positive $\cos\theta$ for events with masses above 1.8 GeV/c^2.

We have further subdivided the data into regions of $|\phi_{GJ}|$, as well as $\cos\theta_{GJ}$ (Figs. 33a and 33b). There appears to be little ϕ dependence for negative $\cos\theta$, but for positive $\cos\theta$ the cross section clearly peaks at large $|\phi|$. Changes in ϕ, in general, do not greatly affect the shape of the mass distribution. The dependence of the decay angles on mass and t will be discussed in a later section of this chapter.

3. High-Mass Behavior

There is some evidence in our data for the production of a high-mass state above 2 GeV/c^2. Such an observation has recently been reported in the literature[8]. A plot showing the high-mass portion of $d\sigma/dM$, given in Fig. 34, shows the suggestion of an excess of events at approximately 2.2 GeV/c^2. The effect is further enhanced by selecting those events with positive values of $\cos\theta_{GJ}$.

D. Decay-Angle Distributions

Cross sections as a function of $\cos\theta_{GJ}$ and $|\phi_{GJ}|$ are given in Figs. 35 and 36 for two t regions and five mass regions. Our $d\sigma/d|\phi_{GJ}|$ spectra are nearly independent of mass and t, with a common minimum at $|\phi|=0°$ and a maximum at $|\phi|=180°$. The dependence

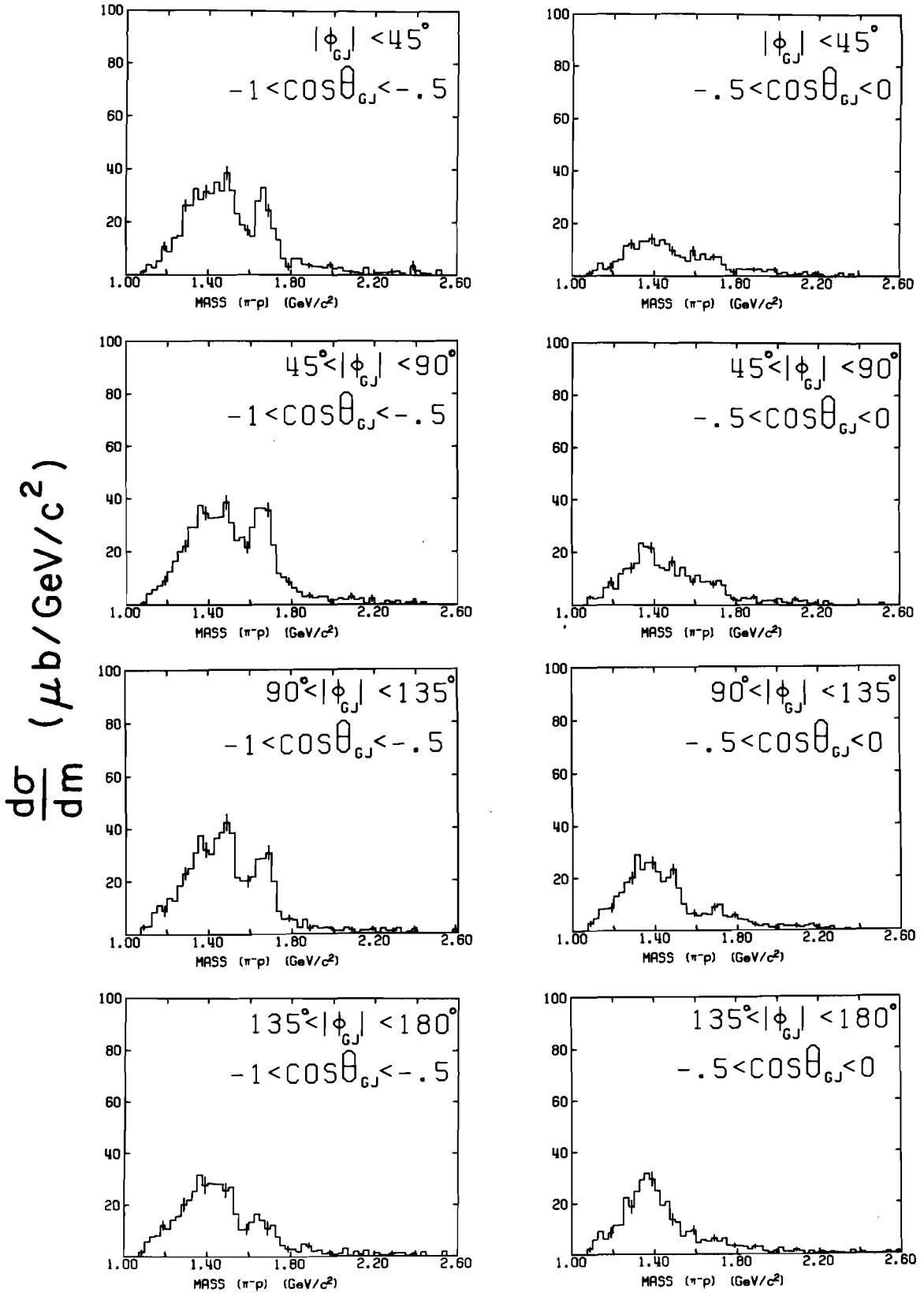
$\frac{d\sigma}{dm}$ (μb/GeV/c^2)
$|\phi_{GJ}| < 45°$
$-1 < \cos\theta_{GJ} < -.5$
$-.5 < \cos\theta_{GJ} < 0$
$45° < |\phi_{GJ}| < 90°$
$90° < |\phi_{GJ}| < 135°$
$135° < |\phi_{GJ}| < 180°$
MASS (π^-p) (GeV/c^2)
1.00
1.40
1.80
2.20
2.60
20
40
60
80
100

Figure 33 (a)

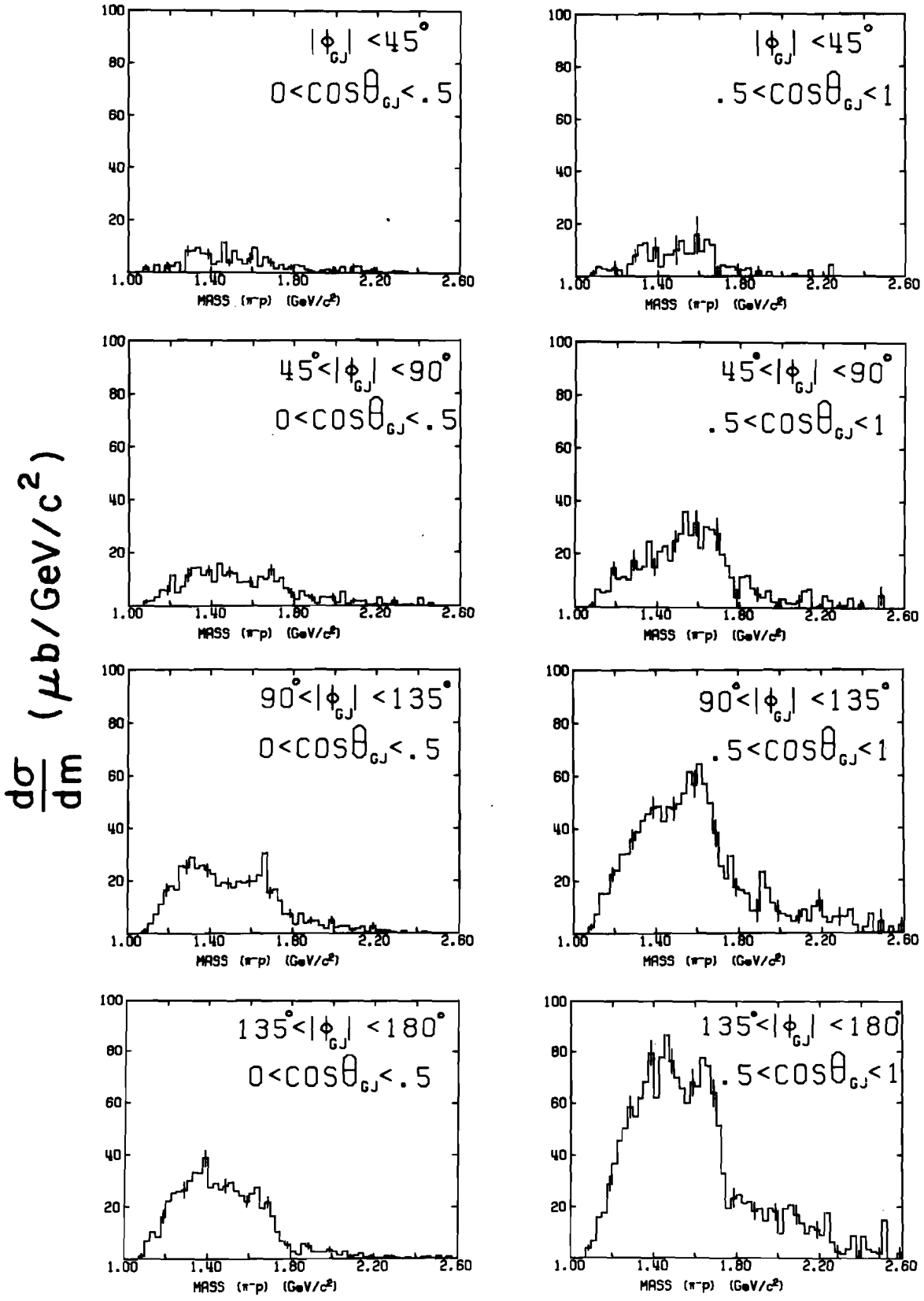
$\frac{d\sigma}{dm}$ (μb/GeV/c^2)
$|\phi_{GJ}| < 45°$
$0 < \cos\theta_{GJ} < .5$
$|\phi_{GJ}| < 45°$
$.5 < \cos\theta_{GJ} < 1$
$45° < |\phi_{GJ}| < 90°$
$0 < \cos\theta_{GJ} < .5$
$45° < |\phi_{GJ}| < 90°$
$.5 < \cos\theta_{GJ} < 1$
$90° < |\phi_{GJ}| < 135°$
$0 < \cos\theta_{GJ} < .5$
$90° < |\phi_{GJ}| < 135°$
$.5 < \cos\theta_{GJ} < 1$
$135° < |\phi_{GJ}| < 180°$
$0 < \cos\theta_{GJ} < .5$
$135° < |\phi_{GJ}| < 180°$
$.5 < \cos\theta_{GJ} < 1$
MASS (π^-p) (GeV/c^2)
1.00
1.40
1.80
2.20
2.60
20
40
60
80
100

Figure 33 (b)

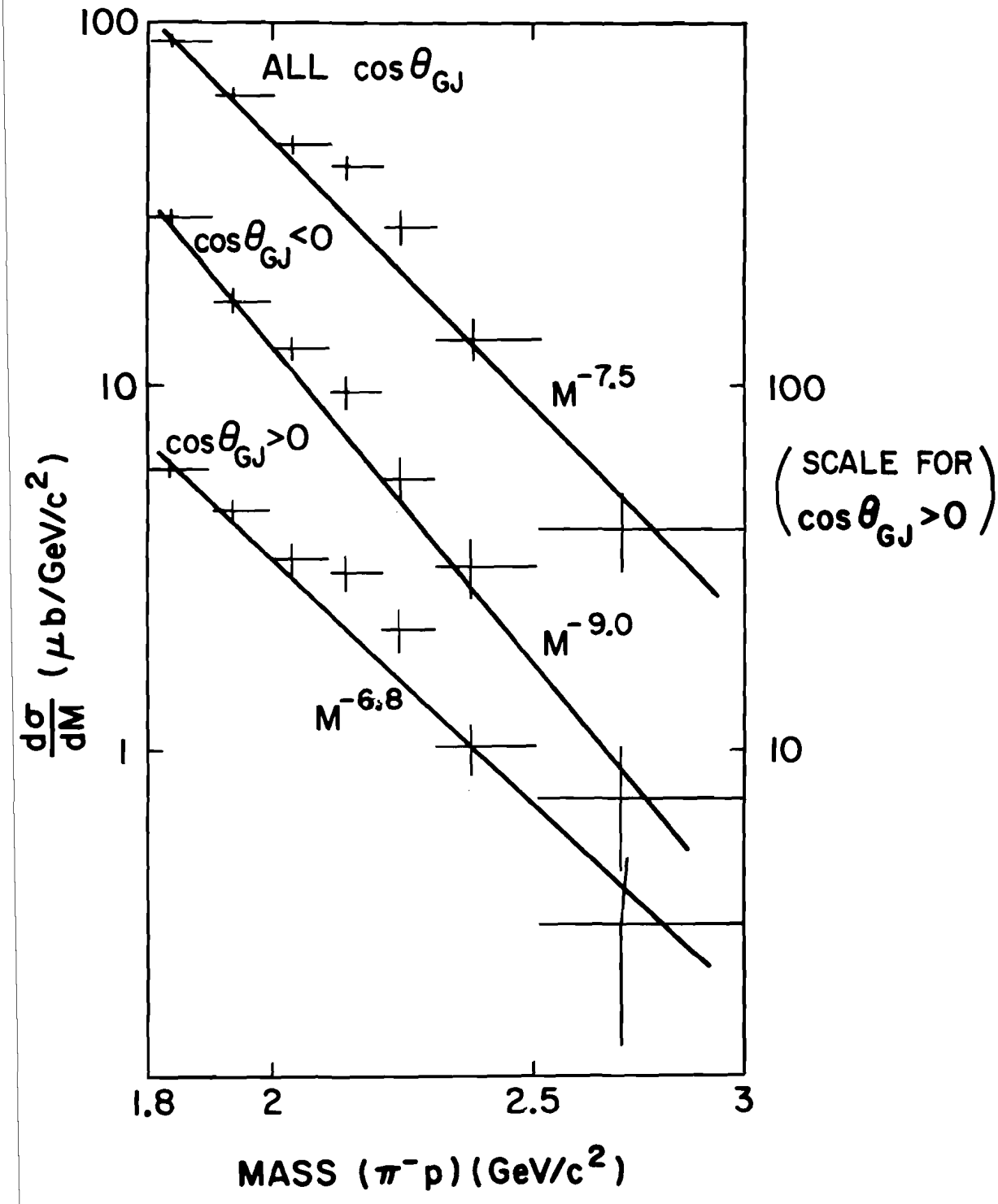
100
10
1
ALL cos θGJ
cos θGJ<0
cos θGJ>0
M^-7.5
M^-9.0
M^-6.8
100
10
(SCALE FOR cos θGJ>0)
dσ/dM (μb/GeV/c²)
1.8
2
2.5
3
MASS (π⁻p) (GeV/c²)

Figure 34

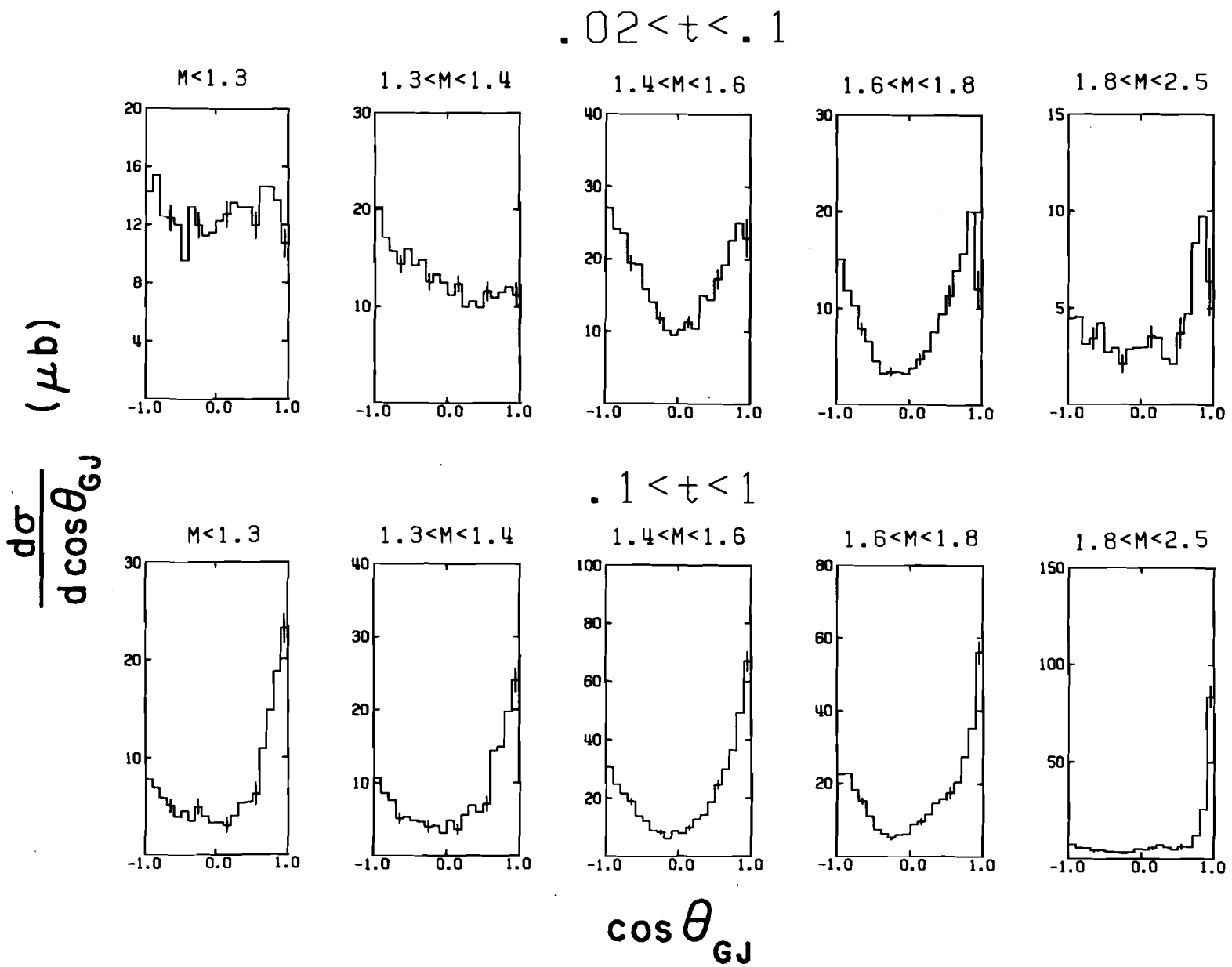
.02<t<.1
M<1.3
1.3<M<1.4
1.4<M<1.6
1.6<M<1.8
1.8<M<2.5
.1<t<1
M<1.3
1.3<M<1.4
1.4<M<1.6
1.6<M<1.8
1.8<M<2.5
$\frac{d\sigma}{d\cos\theta_{GJ}}$ (μb)
$\cos\theta_{GJ}$

Figure 35

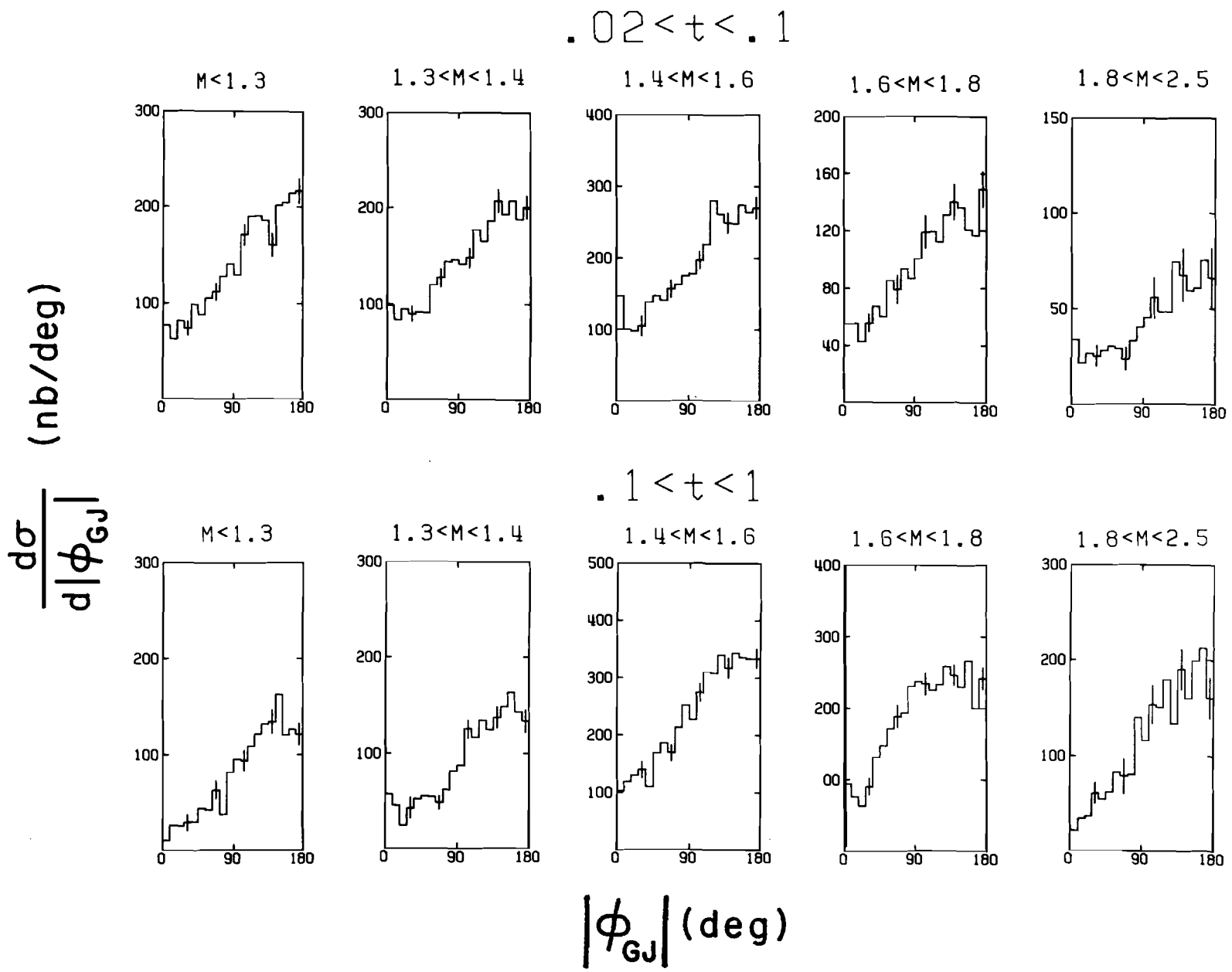
.02<t<.1
M<1.3
1.3<M<1.4
1.4<M<1.6
1.6<M<1.8
1.8<M<2.5
.1<t<1
M<1.3
1.3<M<1.4
1.4<M<1.6
1.6<M<1.8
1.8<M<2.5
dσ/d|φGJ| (nb/deg)
|φGJ| (deg)

Figure 36

of the $\cos\theta_{GJ}$ distribution on mass and t is more pronounced. At small mass and t, $d\sigma/d\cos\theta_{GJ}$ is nearly flat. As the mass is increased, the small-t data show, first, a slight peak at $\cos\theta = -1$, then, nearly equal peaks at the two extremes of $\cos\theta$, and finally, at the highest masses, a single peak near $\cos\theta=1$. All mass intervals for the high-t data exhibit similar behavior in $\cos\theta$: there is a large peak at $\cos\theta=1$ and a smaller peak at small $\cos\theta = -1$. The data at high t and highest mass have a particularly pronounced peak at $\cos\theta=1$.

A more dramatic display of the variation of the cross section with the decay angles is given in Fig. 37. This illustration combines a weighted scattergram (top) with a perspective view of a three-dimensional representation of the cross section. It is clear that the cross section is largest at large $\cos\theta_{GJ}$ and large $|\phi_{GJ}|$, and varies slowly for $\cos\theta_{GJ}$ less than zero. We have also performed a more detailed analysis of the decay angular distribution by decomposing the data into a sum of spherical harmonics.

The normalized moments of the spherical harmonics, or simply the "moments" are defined as follows:

$$\langle Y_{\ell m}\rangle \equiv \frac{\sum_i W_i \; Y_{\ell m}(\cos\theta_i, \phi_i)}{\sum W_i}$$

where the summation runs over all events, W_i is the weight for an event, and the angles θ and ϕ are the decay angles in some particular rest frame of the $\pi^- p$ system. For our data, moments were

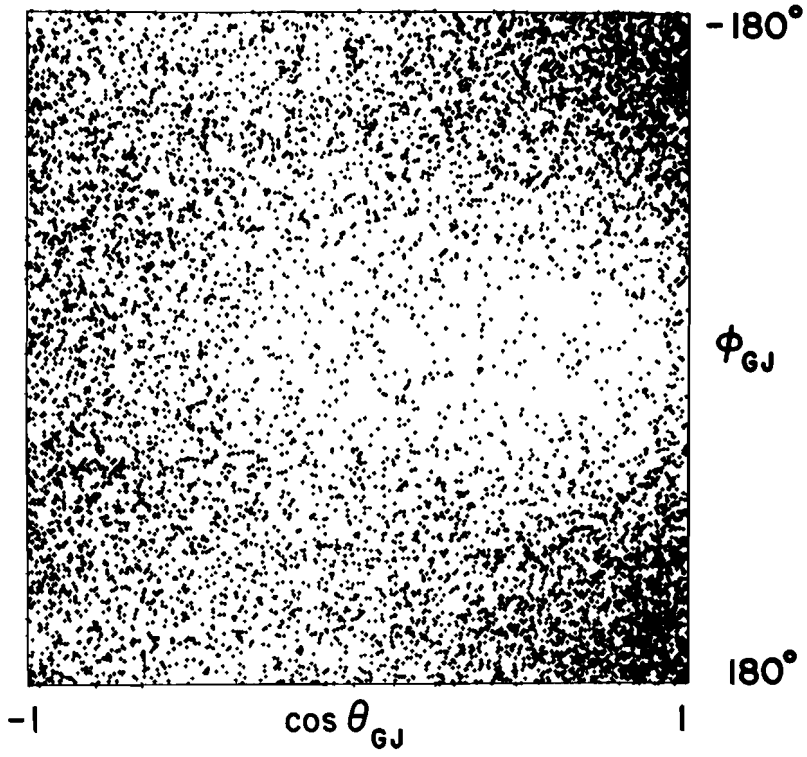

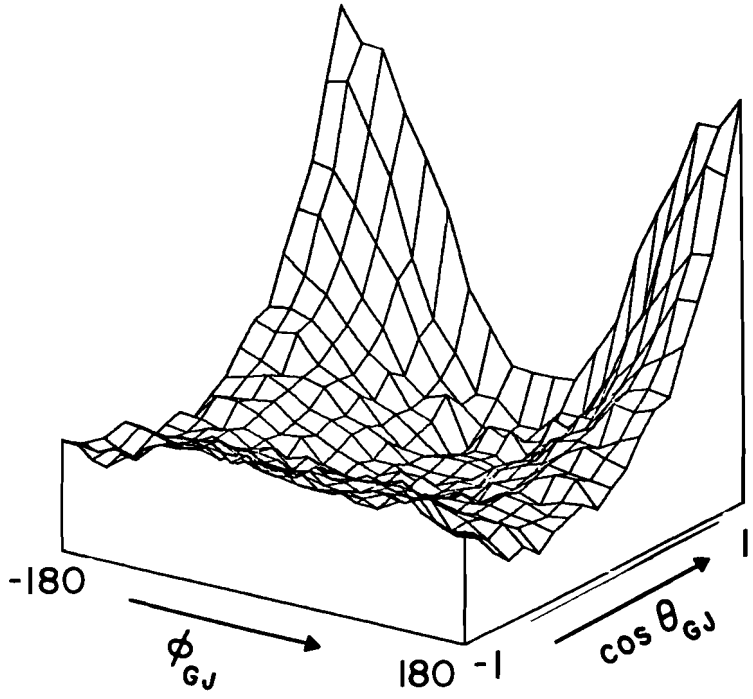

Figure 37

calculated using two sets of mass and t intervals. In the first calculation, the data were divided into two t intervals with seventeen mass intervals at low t and sixteen mass intervals at high t. This gave a detailed mass dependence which is particularly useful in determining what, if any, resonant states are present in the data. A second calculation was performed using seven t intervals, each with six mass intervals. This enabled us to examine the t dependence of the moments in more detail. Table VI lists the mass and t intervals that were used in the analyses.

Moments were calculated in the s and t channel frames for ℓ values up to $\ell=6$. Both the real and imaginary parts of the moments were calculated but as mentioned previously parity conservation requires our data to be symmetric about $\phi=0$, which implies that the imaginary parts of all moments must vanish. Our data do indeed satisfy this requirement as can be demonstrated through an inspection of the distribution in the imaginary parts of all moments in terms of the number of standard deviations they differ from zero (i.e., plotting the calculated moments divided by their experimental errors). If the observed imaginary parts are merely random statistical fluctuations around zero then one expects such a plot to be Gaussian, centered at zero, with a unit standard deviation. The results shown in Fig. 38 for both sets of mass and t intervals, as well as both kinds of rest frames, are seen to be consistent with this prediction. Individual imaginary parts for the moments will therefore, not be present in this thesis. The observed

Table VI

Mass and t intervals used in the calculation of moments

(t in GeV^2, mass in GeV/c^2)

Calculation 1

.02 < t < .12 with the following mass intervals

< 1.18	1.18 - 1.23	1.23 - 1.27	1.27 - 1.33	1.33 - 1.35
1.35 - 1.37	1.37 - 1.39	1.39 - 1.42	1.42 - 1.45	1.45 - 1.48
1.48 - 1.51	1.51 - 1.55	1.55 - 1.60	1.60 - 1.65	1.65 - 1.70
1.70 - 1.80	1.80 - 2.50			

.12 < t < 1 with the following mass intervals

< 1.24	1.24 - 1.30	1.35 - 1.40	1.40 - 1.44	1.44 - 1.48
1.48 - 1.51	1.51 - 1.54	1.54 - 1.58	1.58 - 1.62	1.62 - 1.65
1.65 - 1.68	1.68 - 1.72	1.72 - 1.79	1.79 - 1.92	1.92 - 2.16
2.16 - 3.00				

Calculation 2

.02 < t < .05	each of these t intervals with each of the following mass intervals	< 1.25
.05 < t < .08		1.25 - 1.35
.08 < t < .12		1.35 - 1.45
.12 < t < .2		1.45 - 1.55
.2 < t < .4		1.55 - 1.80
.4 < t < .6		1.8 - 3.0
.6 < t < 1		

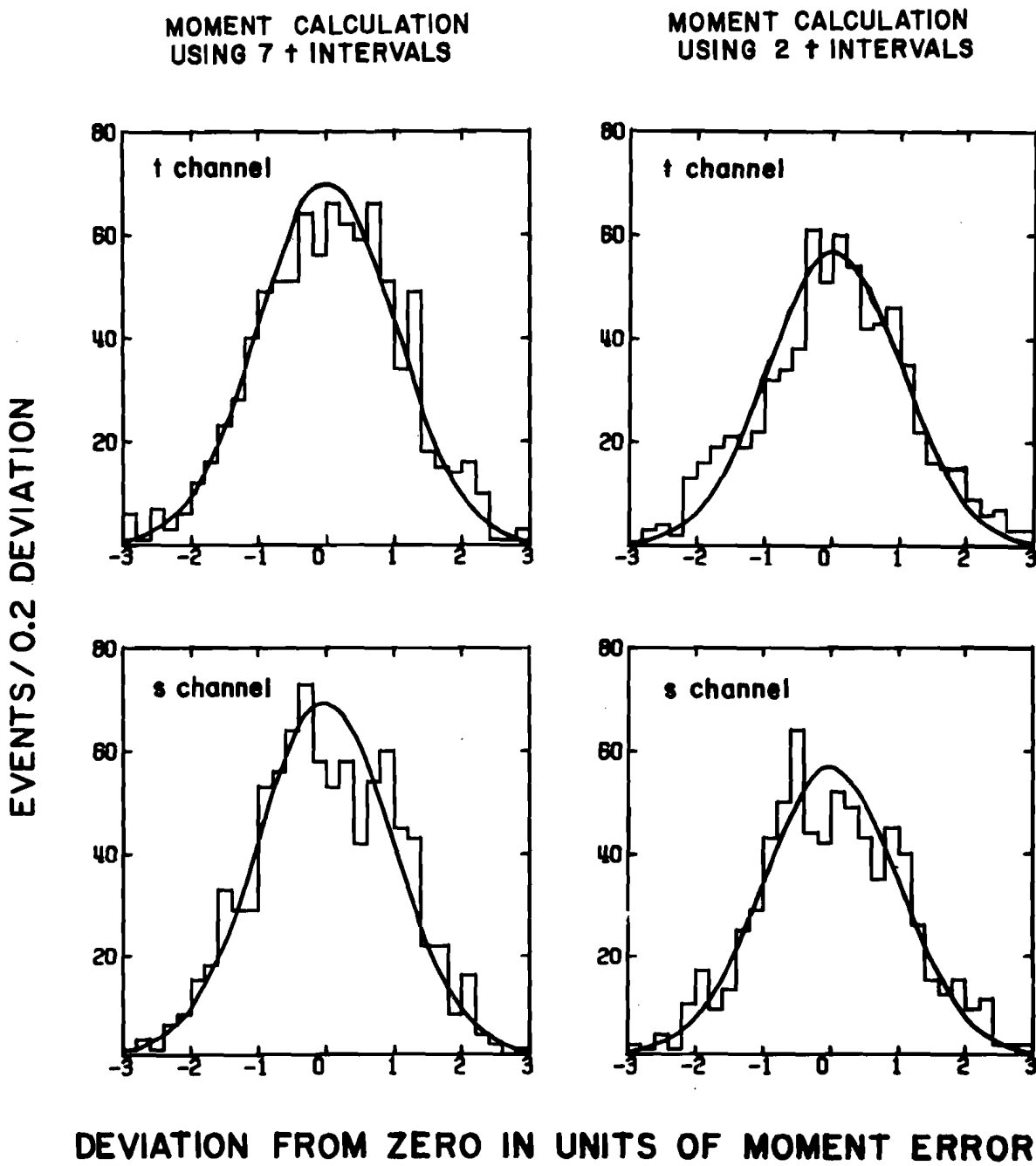
MOMENT CALCULATION
USING 7 t INTERVALS
MOMENT CALCULATION
USING 2 t INTERVALS
t channel
t channel
s channel
s channel
EVENTS / 0.2 DEVIATION
DEVIATION FROM ZERO IN UNITS OF MOMENT ERROR

Figure 38

distributions in Fig. 38 support the reliability of the various corrections that we have applied to the data.

The real parts to the moments are plotted in Figs. 39 through 42 and the corresponding values are listed in Tables VIIa through VIIf. Any reasonably complete understanding of all these data would necessarily require a detailed theoretical model, a task which is beyond the scope of the present thesis. One can, however, make several broad comments relating to t-channel moment values to previously presented distributions for $d\sigma/d\cos\theta_{GJ}$ and $d\sigma/d|\phi_{GJ}|$ (Figs. 35 and 36). First of all, the moments are in general quite small for $m > 2$. Since the real part of a $Y_{\ell m}$ is proportional to $\sin m\phi$, the lack of large contributions from $m > 2$ is a direct consequence of the slow variation of $d\sigma/d|\phi_{GJ}|$. The broad maxima observed for $d\sigma/d|\phi_{GJ}|$ at $|\phi| = 180°$ contrast sharply with the steep forward peaks observed in $d\sigma/d\cos\theta_{GJ}$. This asymmetry in $\cos\theta_{GJ}$ is reflected in the large values of the $\langle Y_{\ell o}\rangle$ at large mass and high t. This comes about as follows: The spherical harmonics are proportional to $(\cos\theta)^{\ell}$, hence all the m=0 moments will be large and positive at $\cos\theta=1$. Because even and odd ℓ-contributions will tend to cancel for negative $\cos\theta$, this will result in the observed forward-backward asymmetry.

The manner in which $\langle Y_{10}\rangle$ ($\sim\langle\cos\theta\rangle$) varies with mass at low t can be discerned from the nature of the $d\sigma/d\cos\theta_{GJ}$ distributions. For example, in the mass region between 1.3 and 1.4 GeV/c^2 there is a relatively large cross section in the backward direction.

t channel moments

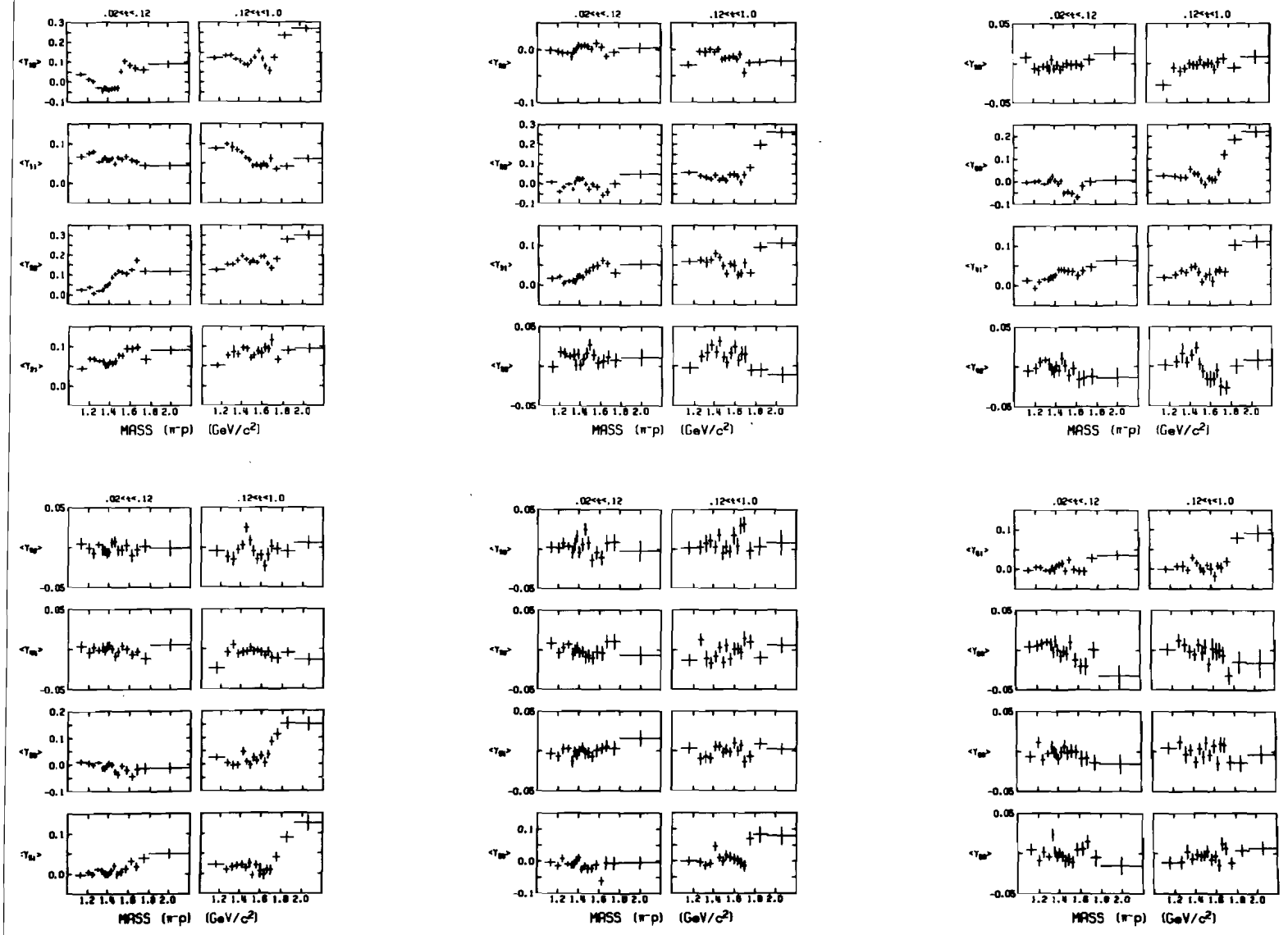

Figure 39

t channel moments

M < 1.25

1.25 < M < 1.35

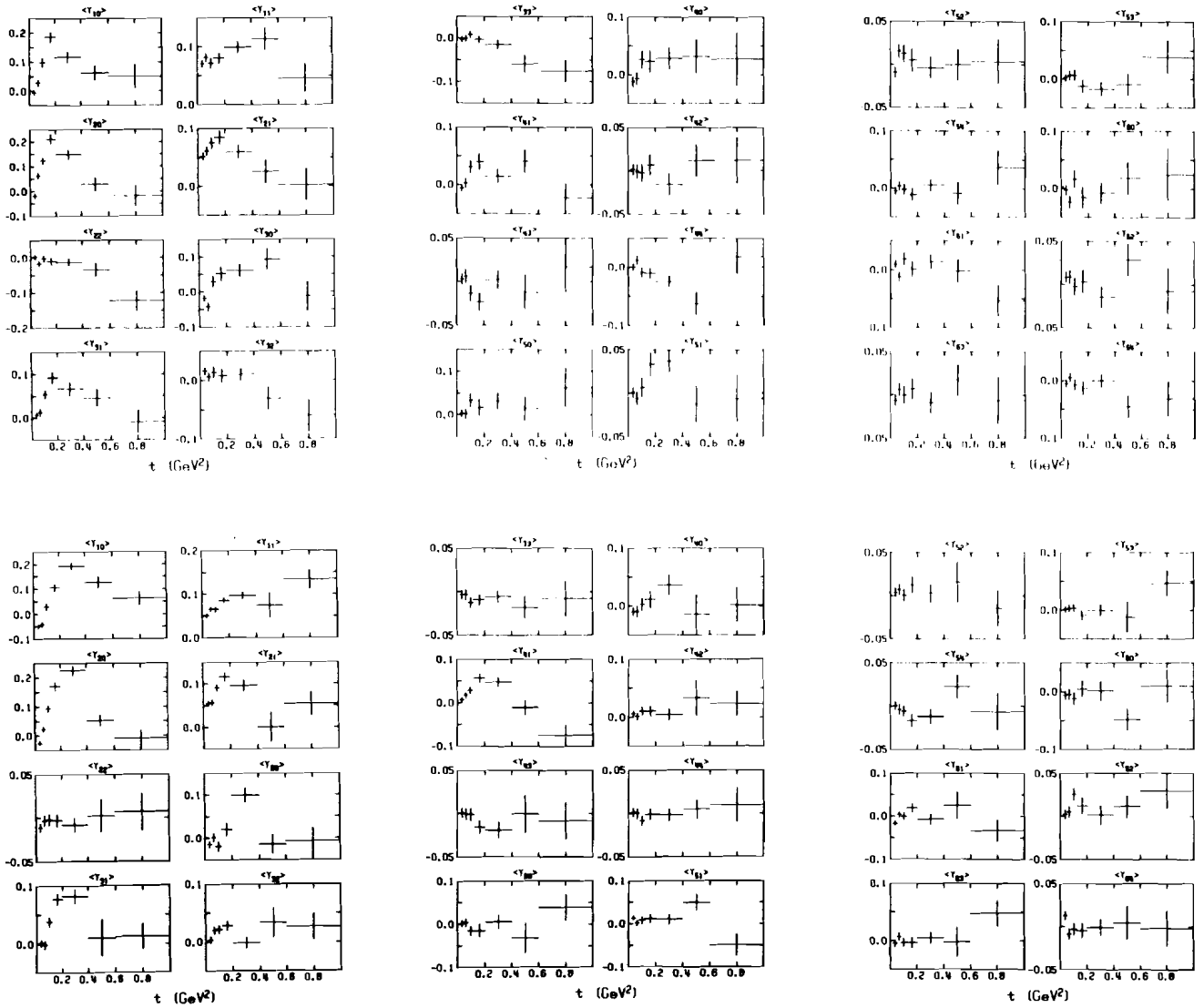

Figure 40 (a)

t channel moments

1.35<M<1.45

1.45<M<1.55

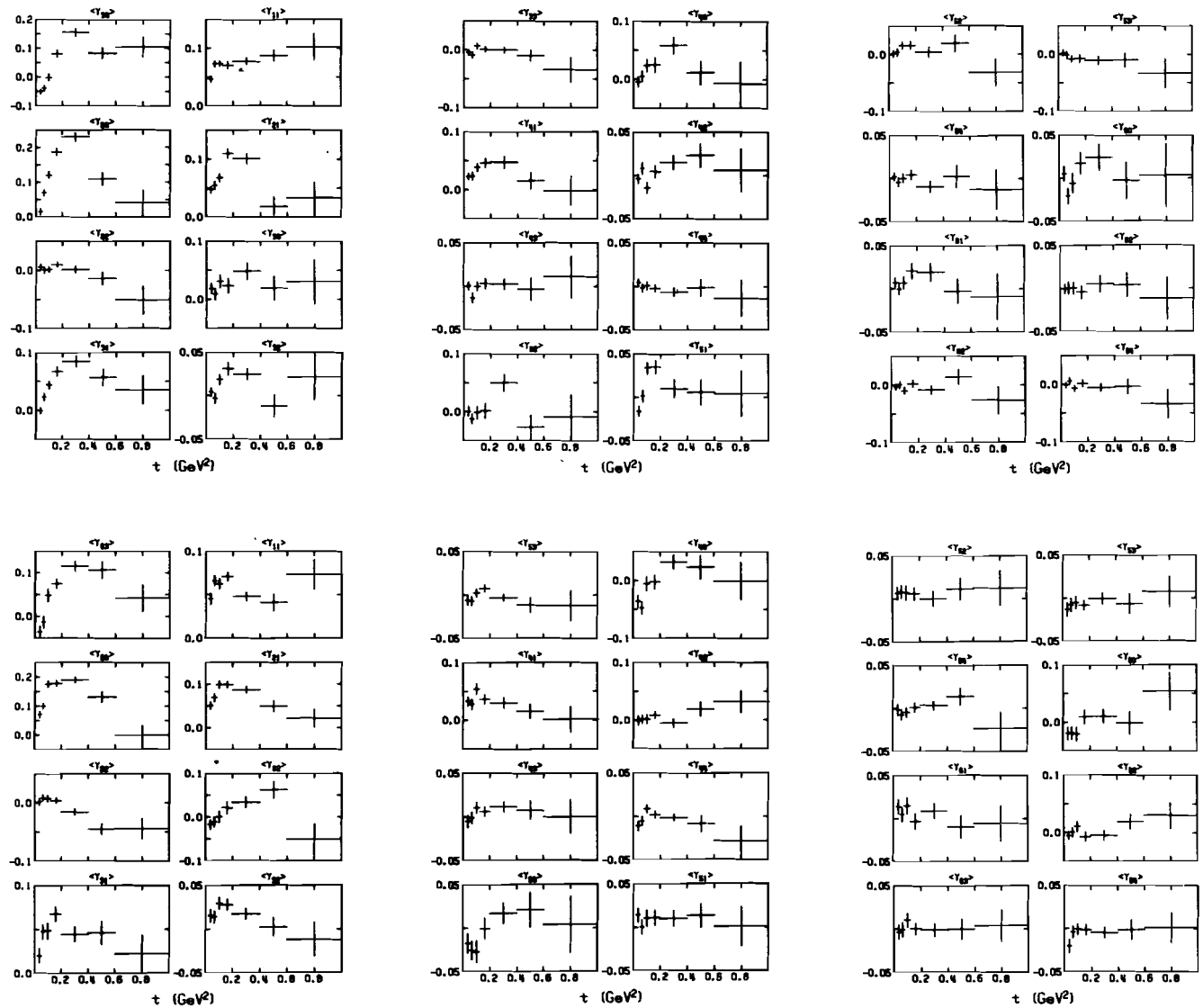

Figure 40 (b)

t channel moments

1.55 < M < 1.8

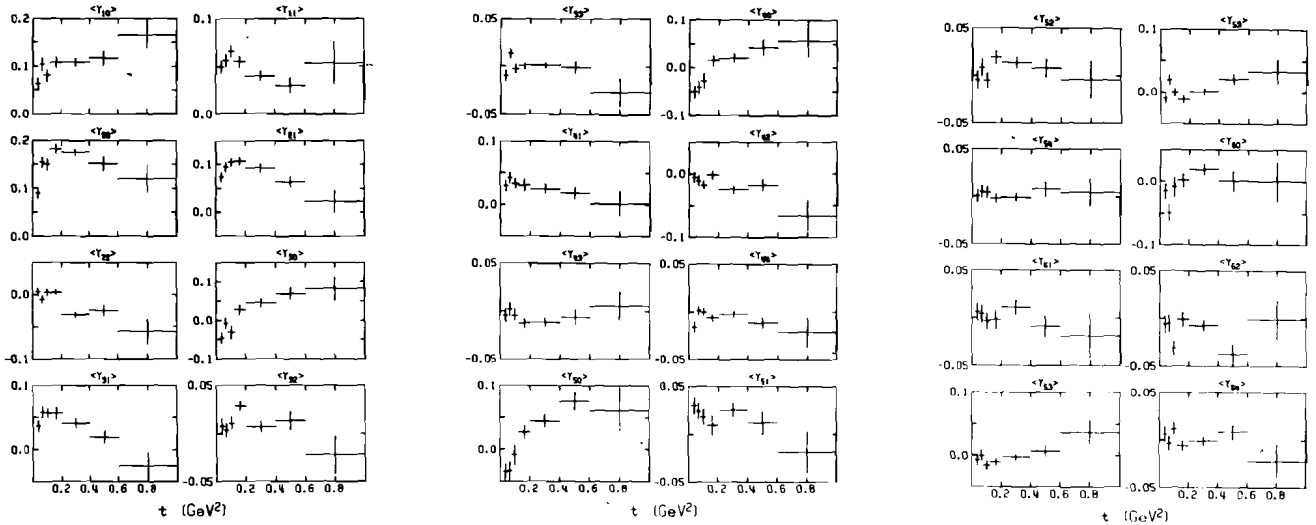

1.8 < M < 3

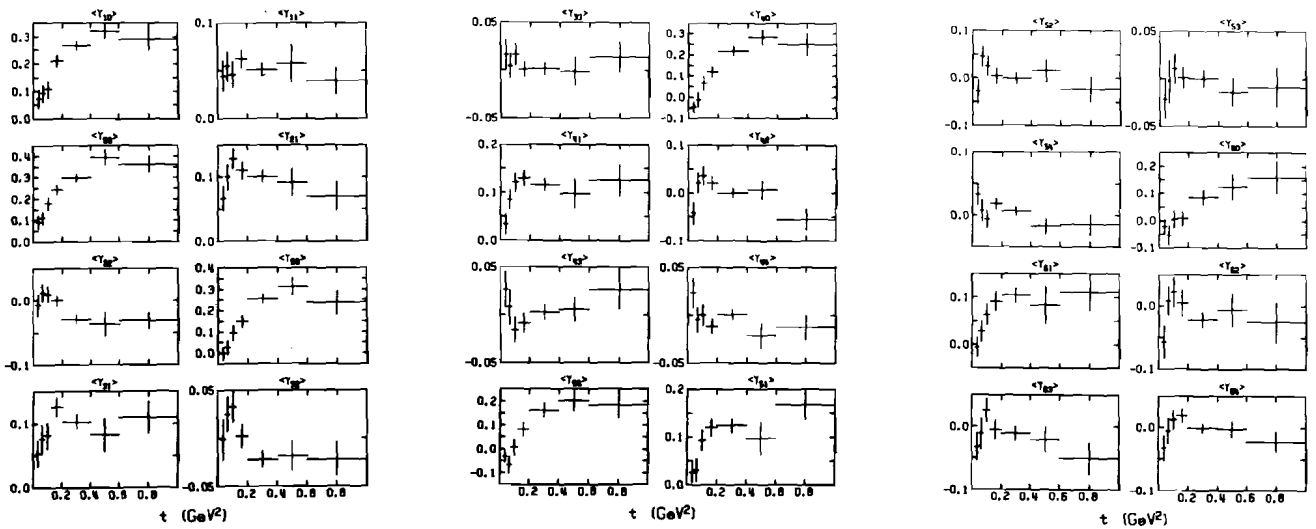

Figure 40 (c)

s channel moments

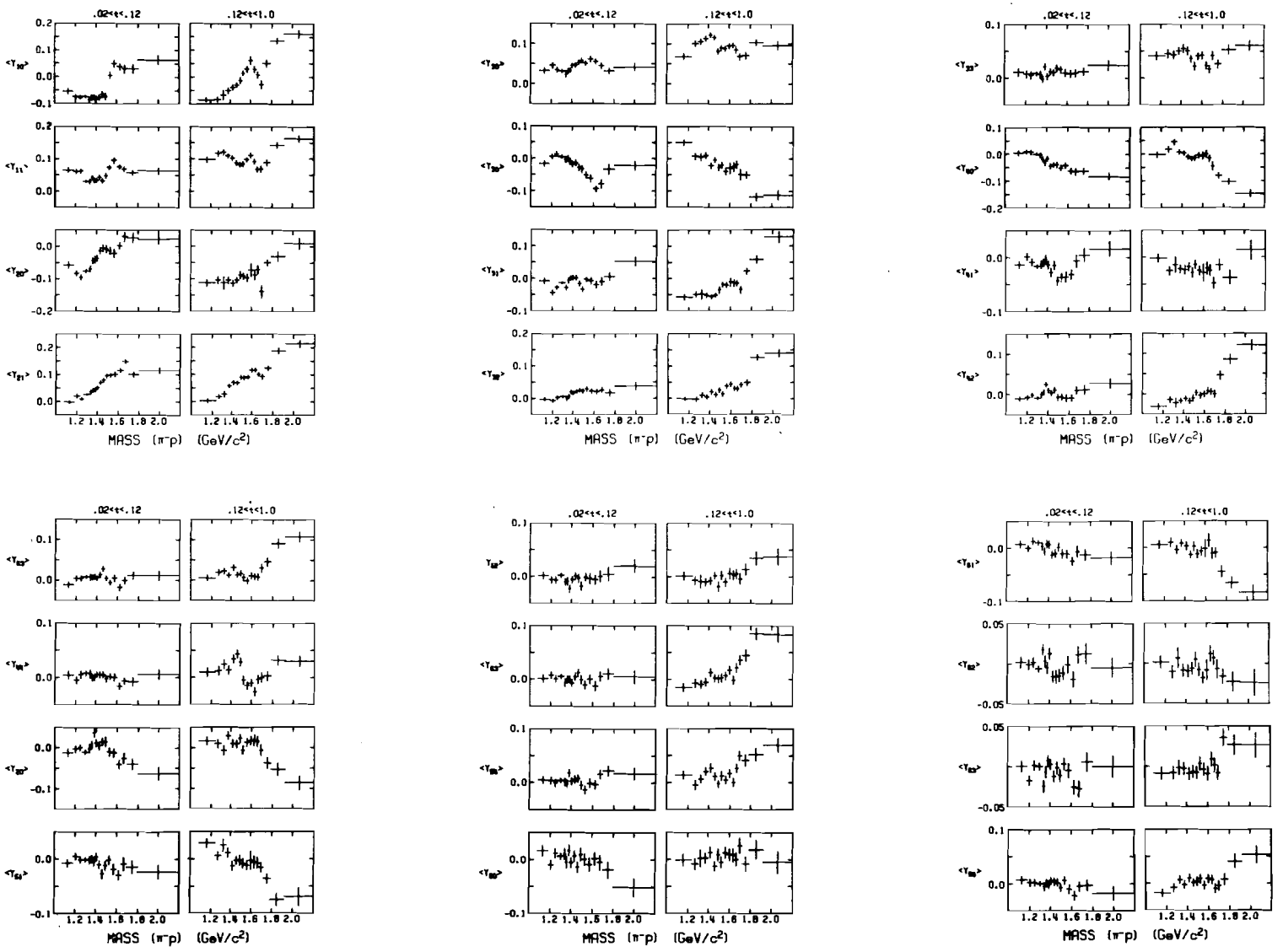

Figure 41

s channel moments

M < 1.25

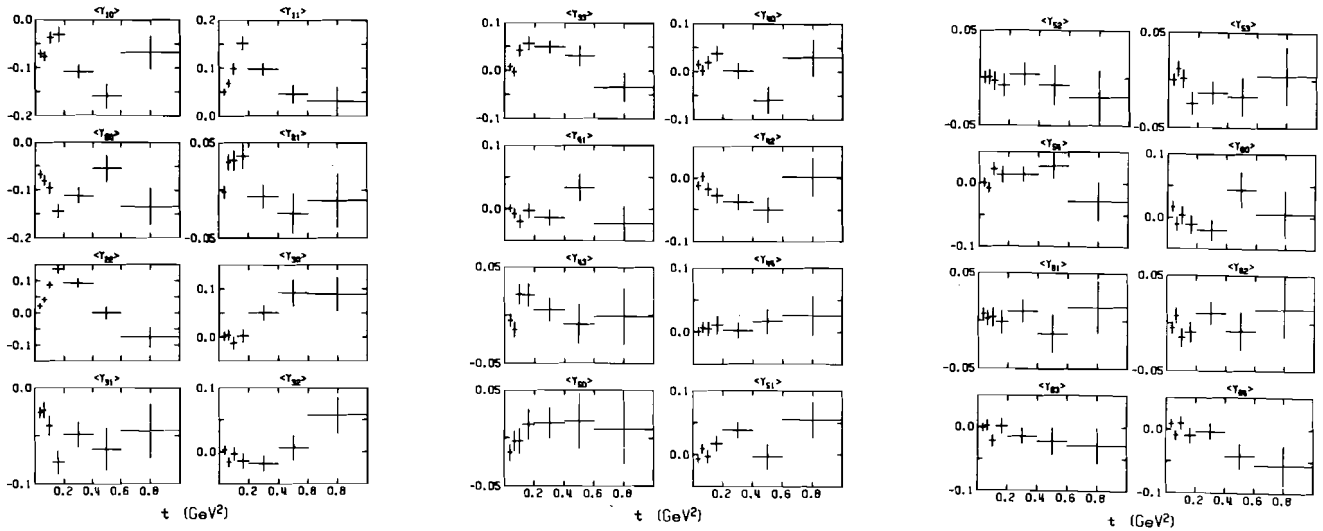

1.25 < M < 1.35

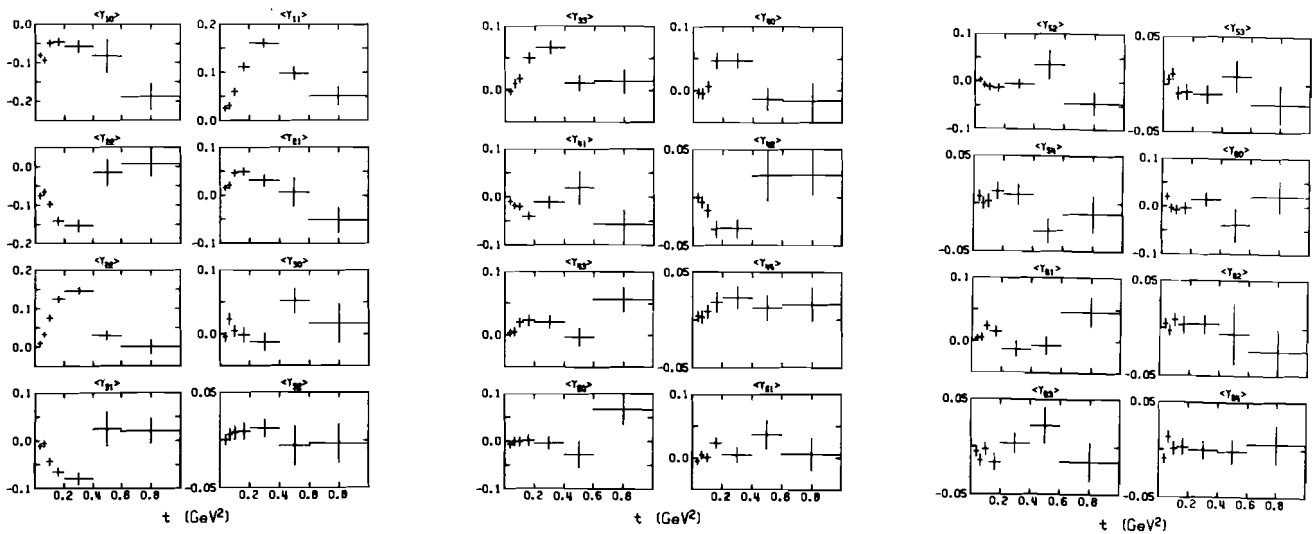

Figure 42 (a)

s channel moments

1.35<M<1.45

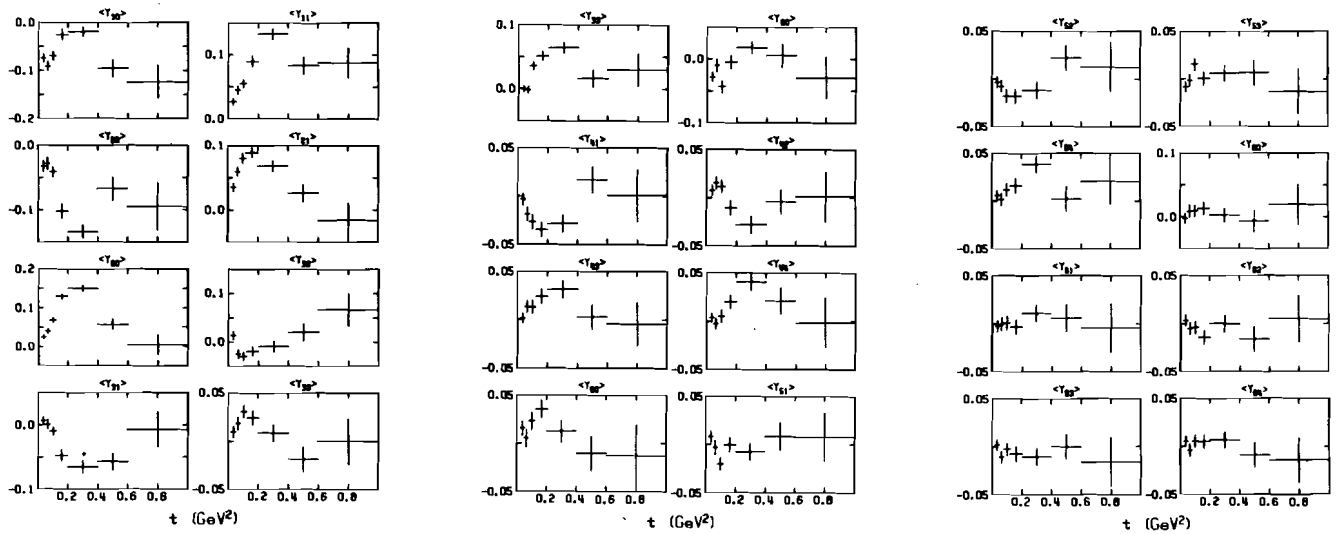

1.45<M<1.55

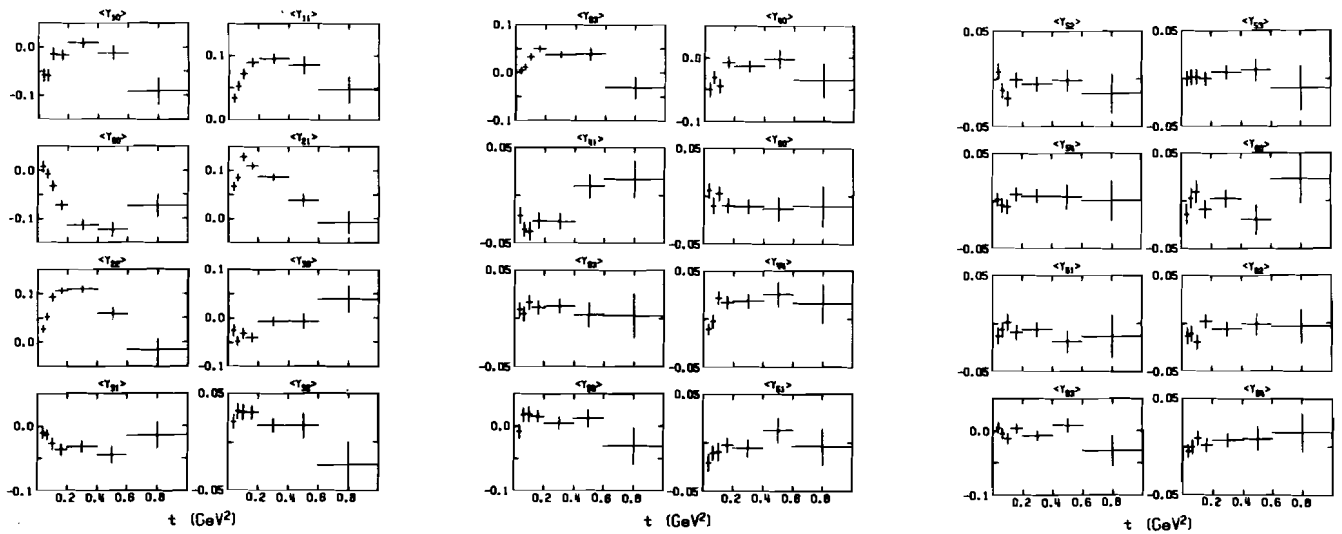

Figure 42 (b)

s channel moments

1.55 < M < 1.8

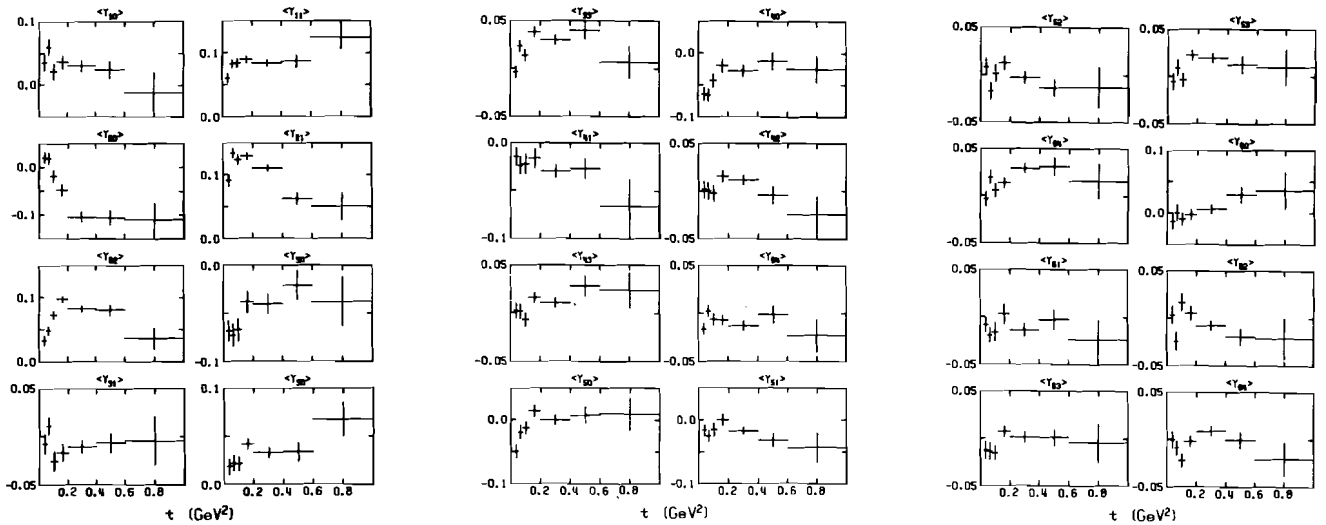

1.8 < M < 3

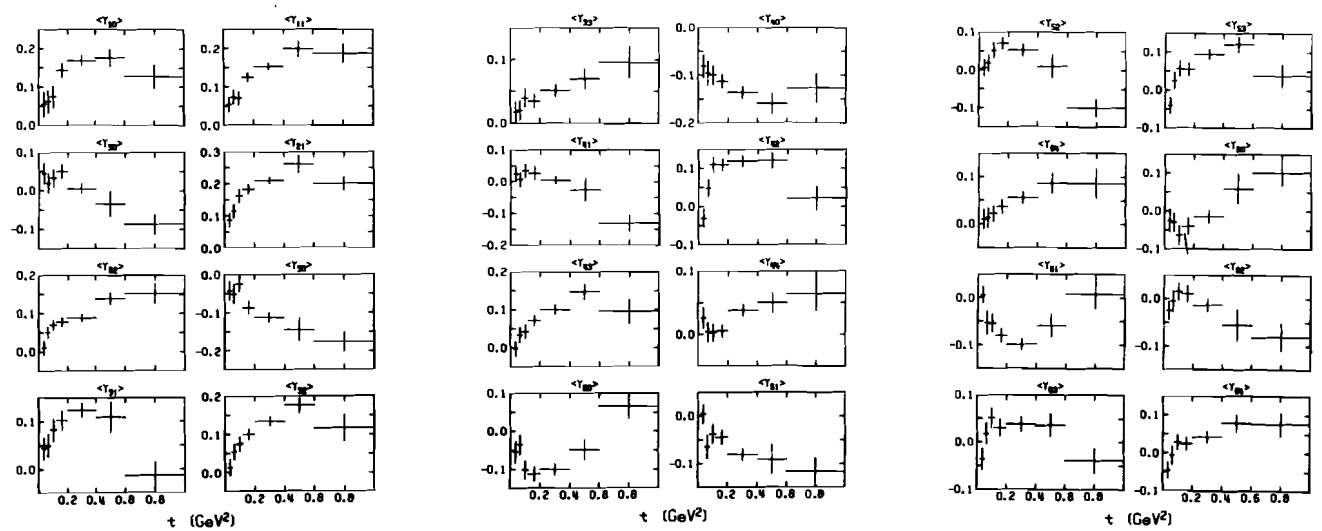

Figure 42 (c)

Table VII (a)

<Re(Y(L,M))> in the t channel helicity frame for .02<t<0.12

L M	1.00<m<1.18	1.18<m<1.23	1.23<m<1.27	1.27<m<1.33	1.33<m<1.35	1.35<m<1.37	1.37<m<1.39	1.39<m<1.42	1.42<m<1.45
1 0	0.039±.010	0.013±.010	0.002±.009	-.030±.007	-.044±.011	-.029±.011	-.034±.012	-.040±.011	-.032±.012
1 1	0.067±.008	0.076±.006	0.060±.006	0.053±.004	0.059±.007	0.066±.004	0.057±.006	0.057±.006	0.064±.006
2 0	0.025±.010	0.030±.010	0.006±.009	0.010±.006	0.023±.011	0.042±.011	0.042±.011	0.050±.011	0.067±.010
2 1	0.064±.007	0.068±.007	0.060±.007	0.063±.005	0.061±.007	0.050±.007	0.051±.007	0.060±.007	0.056±.007
2 2	-.001±.007	-.003±.006	-.006±.006	-.006±.004	-.013±.007	-.002±.004	-.008±.006	0.000±.006	0.000±.005
3 0	0.008±.010	-.040±.010	-.018±.009	-.002±.006	-.020±.011	0.005±.011	0.024±.012	0.021±.011	0.020±.011
3 1	0.017±.007	0.021±.007	0.005±.007	0.013±.005	0.010±.008	0.006±.007	0.021±.008	0.023±.007	0.019±.008
3 2	-.001±.007	0.018±.006	0.016±.006	0.013±.004	0.015±.008	0.001±.007	0.016±.007	0.001±.006	0.009±.007
3 3	0.000±.007	-.006±.006	-.009±.006	-.004±.004	-.004±.007	-.000±.004	0.005±.006	-.007±.005	-.001±.005
4 0	-.005±.010	-.001±.010	0.001±.009	-.013±.006	-.000±.010	0.006±.012	0.025±.012	0.004±.011	-.011±.011
4 1	0.012±.007	-.001±.007	0.009±.007	0.016±.005	0.016±.008	0.021±.007	0.021±.008	0.027±.007	0.039±.008
4 2	-.005±.007	-.003±.007	0.006±.006	0.009±.004	0.003±.008	-.004±.007	-.007±.007	0.001±.007	-.005±.007
4 3	0.005±.007	-.001±.006	-.006±.007	0.004±.004	-.003±.007	-.004±.008	-.000±.006	-.006±.006	0.000±.008
4 4	0.004±.007	-.005±.006	0.002±.006	-.001±.004	0.002±.007	-.002±.004	0.004±.006	0.005±.005	0.000±.005
5 0	0.010±.010	0.004±.010	-.002±.009	0.000±.006	-.013±.011	-.013±.012	-.005±.012	0.000±.011	0.000±.011
5 1	-.002±.007	0.004±.007	-.001±.007	0.011±.005	0.007±.008	0.002±.007	-.000±.008	-.003±.007	0.007±.008
5 2	0.003±.007	0.002±.007	0.000±.007	0.004±.004	-.004±.008	0.007±.007	0.017±.007	-.004±.007	0.000±.008
5 3	0.009±.007	-.004±.007	0.003±.006	0.007±.004	-.005±.008	-.001±.007	0.003±.006	-.004±.008	-.002±.007
5 4	-.003±.007	-.007±.007	0.003±.006	0.002±.004	-.014±.007	-.001±.006	-.005±.006	0.000±.006	0.005±.006
5 5	-.002±.007	0.003±.006	0.010±.006	0.004±.004	-.013±.007	0.007±.004	-.005±.008	-.007±.005	-.002±.005
6 0	-.003±.010	-.013±.010	0.000±.009	-.000±.006	-.012±.011	-.009±.012	0.003±.011	0.011±.011	-.025±.011
6 1	-.003±.007	0.004±.007	0.004±.007	-.005±.005	-.006±.007	0.005±.007	-.004±.008	0.006±.007	0.011±.008
6 2	0.004±.007	0.005±.007	0.000±.007	0.010±.004	0.007±.008	-.003±.007	0.011±.007	0.000±.008	-.000±.008
6 3	-.007±.007	0.011±.007	-.010±.007	-.003±.004	0.004±.008	-.001±.007	-.003±.007	-.010±.006	-.001±.007
6 4	0.005±.007	-.009±.007	0.001±.008	-.005±.004	0.026±.007	0.003±.008	-.004±.008	0.003±.006	-.000±.008
6 5	-.006±.007	-.006±.006	0.007±.007	0.006±.004	-.010±.007	-.004±.006	0.004±.004	0.000±.008	-.010±.008
6 6	0.003±.007	0.009±.009	0.004±.006	0.002±.004	-.000±.007	0.004±.008	-.001±.008	0.013±.008	0.007±.008

<Re(Y(L,M))> in the t channel helicity frame for .02<t<0.12

L M	1.45<m<1.48	1.48<m<1.51	1.51<m<1.55	1.55<m<1.60	1.60<m<1.65	1.65<m<1.70	1.70<m<1.80	1.80<m<2.30
1 0	-.031±.013	-.030±.014	0.054±.013	0.105±.013	0.082±.014	0.000±.017	0.060±.018	0.091±.019
1 1	0.040±.006	0.065±.006	0.060±.008	0.067±.008	0.057±.007	0.053±.006	0.040±.008	0.044±.009
2 0	0.104±.010	0.120±.011	0.112±.011	0.105±.012	0.126±.011	0.172±.014	0.110±.010	0.117±.019
2 1	0.062±.008	0.077±.009	0.076±.008	0.094±.010	0.094±.009	0.090±.009	0.067±.011	0.091±.011
2 2	0.009±.005	0.004±.006	0.001±.006	0.011±.006	0.005±.006	-.013±.006	-.005±.007	0.003±.009
3 0	-.001±.011	-.028±.013	-.003±.012	-.016±.014	-.055±.013	-.042±.020	-.001±.019	0.050±.020
3 1	0.033±.009	0.036±.009	0.044±.009	0.049±.009	0.062±.010	0.054±.009	0.030±.011	0.052±.012
3 2	0.017±.007	0.020±.007	0.014±.007	0.004±.008	0.006±.009	0.011±.009	0.007±.009	0.011±.011
3 3	-.000±.005	-.003±.005	0.000±.005	-.001±.006	-.001±.005	-.003±.005	0.005±.007	0.013±.008
4 0	0.003±.011	-.053±.013	-.046±.012	-.054±.014	-.069±.013	-.020±.020	-.001±.020	0.004±.020
4 1	0.040±.008	0.038±.009	0.035±.009	0.035±.010	0.025±.009	0.037±.010	0.007±.011	0.004±.012
4 2	0.011±.007	0.001±.008	-.011±.008	-.002±.009	-.016±.010	-.015±.010	-.012±.010	-.014±.012
4 3	0.000±.007	-.003±.007	-.003±.007	0.003±.008	-.010±.008	-.003±.008	0.002±.009	-.001±.010
4 4	-.009±.005	-.003±.005	0.004±.005	-.000±.006	-.007±.005	-.004±.009	-.012±.007	0.005±.008
5 0	-.026±.011	-.036±.013	-.006±.011	-.019±.014	-.045±.013	-.018±.020	-.015±.020	-.013±.020
5 1	0.021±.008	-.001±.009	0.006±.009	0.013±.009	0.032±.009	0.010±.011	0.039±.012	0.050±.013
5 2	0.025±.007	0.008±.008	-.015±.008	-.005±.009	-.011±.010	0.008±.010	0.009±.010	-.002±.013
5 3	-.009±.008	-.007±.008	-.010±.008	-.003±.008	-.005±.009	0.011±.009	0.010±.010	-.007±.012
5 4	-.003±.006	-.002±.007	-.007±.006	0.001±.008	0.003±.007	0.004±.007	0.003±.009	0.010±.010
5 5	-.006±.005	0.005±.005	-.004±.005	-.001±.006	-.002±.005	-.002±.005	-.000±.008	0.002±.008
6 0	-.014±.011	-.024±.013	-.022±.011	-.011±.014	-.061±.013	-.006±.019	-.007±.010	-.005±.019
6 1	0.016±.008	-.005±.009	0.024±.009	-.001±.009	-.005±.009	-.000±.011	0.029±.012	0.034±.013
6 2	-.002±.007	-.004±.008	0.010±.009	-.013±.009	-.021±.009	-.021±.010	0.001±.011	-.033±.014
6 3	0.006±.008	-.003±.008	0.000±.008	-.000±.009	-.009±.010	-.009±.009	-.010±.010	-.016±.012
6 4	-.010±.008	-.007±.007	-.011±.007	0.005±.008	0.006±.008	0.015±.008	-.005±.010	-.015±.011
6 5	0.001±.008	0.000±.008	-.007±.006	0.007±.006	0.002±.008	-.017±.007	-.007±.008	0.001±.008
6 6	0.001±.005	0.005±.005	0.005±.005	0.000±.005	0.003±.005	0.002±.006	-.000±.008	-.003±.008

<Re(Y(L,M))> in the t channel helicity frame for .12<t<1.00

L M	1.00<m<1.24	1.24<m<1.30	1.30<m<1.35	1.35<m<1.40	1.40<m<1.45	1.45<m<1.48	1.48<m<1.51	1.51<m<1.56	1.56<m<1.58
1 0	0.122±.012	0.133±.012	0.136±.015	0.116±.011	0.106±.013	0.087±.012	0.083±.013	0.108±.013	0.125±.012
1 1	0.007±.007	0.099±.007	0.001±.012	0.085±.006	0.078±.004	0.064±.006	0.050±.006	0.003±.008	0.006±.007
2 0	0.123±.012	0.151±.012	0.153±.011	0.170±.011	0.193±.012	0.176±.011	0.150±.012	0.170±.011	0.190±.011
2 1	0.051±.008	0.076±.009	0.087±.016	0.080±.009	0.096±.008	0.095±.008	0.070±.009	0.070±.008	0.080±.008
2 2	-.020±.007	-.003±.007	-.003±.008	0.001±.006	-.004±.006	0.002±.005	-.019±.006	-.017±.006	-.016±.006
3 0	0.058±.012	0.042±.013	0.035±.013	0.027±.012	0.048±.014	0.021±.012	0.031±.014	0.018±.014	0.004±.013
3 1	0.060±.008	0.064±.009	0.059±.014	0.065±.009	0.081±.008	0.071±.008	0.090±.010	0.080±.008	0.083±.008
3 2	-.002±.008	0.013±.008	0.018±.011	0.027±.007	0.010±.007	0.032±.008	0.012±.007	0.009±.008	0.017±.008
3 3	-.020±.007	-.006±.006	-.011±.007	-.007±.005	-.001±.005	-.002±.005	-.008±.009	0.004±.005	-.003±.005
4 0	0.023±.012	0.021±.013	0.015±.016	0.015±.012	0.052±.015	0.031±.012	0.029±.014	0.000±.014	-.017±.014
4 1	0.019±.008	0.026±.009	0.035±.009	0.031±.009	0.044±.009	0.040±.009	0.031±.010	0.007±.008	0.001±.009
4 2	0.002±.008	0.006±.008	0.017±.012	0.005±.008	0.015±.008	0.020±.007	0.002±.008	-.007±.008	-.016±.008
4 3	-.005±.008	-.012±.007	-.015±.009	-.003±.006	0.003±.007	0.025±.008	0.009±.008	-.008±.007	-.015±.007
4 4	-.020±.007	-.004±.006	0.005±.006	-.006±.005	-.004±.005	-.003±.005	0.001±.009	-.003±.005	-.002±.008
5 0	0.025±.012	0.003±.013	-.006±.015	-.004±.012	0.045±.015	0.009±.012	-.000±.013	0.023±.015	0.011±.013
5 1	0.022±.008	0.010±.009	0.016±.010	0.020±.009	0.022±.009	0.018±.009	0.029±.011	-.004±.009	0.031±.008
5 2	0.002±.008	0.003±.009	0.008±.010	0.011±.008	0.004±.008	0.019±.008	-.005±.009	0.003±.009	-.003±.008
5 3	-.013±.008	0.013±.008	-.011±.011	-.017±.007	-.008±.007	0.004±.007	-.010±.007	0.000±.008	-.012±.008
5 4	0.004±.008	-.009±.007	-.007±.007	-.009±.006	0.006±.006	0.007±.006	-.002±.006	0.002±.006	-.002±.006
5 5	-.012±.007	-.005±.006	0.000±.006	-.012±.005	0.002±.005	-.006±.005	0.010±.005	-.007±.005	0.001±.008
6 0	0.001±.013	-.002±.013	-.012±.012	-.006±.012	0.000±.015	0.010±.012	-.001±.013	0.010±.015	0.012±.013
6 1	-.001±.008	0.007±.009	0.006±.013	-.003±.009	0.029±.009	0.015±.008	0.001±.010	-.007±.008	0.000±.009
6 2	0.001±.008	0.012±.009	0.007±.008	-.002±.008	-.005±.008	0.000±.009	-.003±.010	0.004±.009	-.010±.009
6 3	0.004±.008	0.012±.008	-.004±.011	0.002±.007	-.014±.008	0.003±.007	-.007±.008	0.010±.008	-.000±.008
6 4	-.012±.008	-.011±.008	0.002±.009	-.007±.007	-.001±.007	-.000±.006	-.003±.007	0.003±.008	-.000±.007
6 5	0.007±.007	0.005±.007	-.004±.007	-.005±.006	0.005±.008	0.010±.005	-.001±.008	0.007±.006	-.000±.008
6 6	-.000±.007	-.010±.008	0.005±.006	-.006±.005	0.001±.005	0.001±.005	0.009±.005	0.003±.006	-.007±.008

<Re(Y(L,M))> in the t channel helicity frame for .12<t<1.00

L M	1.58<m<1.62	1.62<m<1.65	1.65<m<1.68	1.68<m<1.72	1.72<m<1.79	1.79<m<1.92	1.92<m<2.30
1 0	0.158±.014	0.117±.014	0.070±.014	0.095±.016	0.129±.017	0.234±.016	0.209±.017
1 1	0.042±.008	0.040±.007	0.042±.007	0.062±.010	0.036±.007	0.002±.007	0.002±.010
2 0	0.191±.014	0.193±.013	0.155±.013	0.133±.014	0.100±.016	0.276±.017	0.290±.022
2 1	0.083±.013	0.096±.010	0.094±.010	0.115±.015	0.005±.009	0.090±.016	0.095±.012
2 2	-.013±.008	-.010±.006	-.009±.006	-.049±.009	-.025±.008	-.030±.007	-.022±.009
3 0	0.067±.017	0.035±.017	0.008±.015	0.045±.017	0.000±.020	0.190±.021	0.250±.025
3 1	0.047±.015	0.025±.011	0.029±.010	0.055±.012	0.030±.010	0.096±.017	0.100±.014
3 2	0.024±.008	0.047±.007	0.016±.008	0.015±.010	-.009±.008	-.005±.009	-.011±.010
3 3	0.000±.006	-.000±.005	-.008±.006	0.001±.007	0.006±.006	-.006±.007	0.000±.008
4 0	0.011±.016	0.004±.016	0.006±.016	0.039±.018	0.117±.010	0.102±.021	0.210±.025
4 1	0.026±.017	0.008±.012	0.033±.010	0.038±.010	0.032±.011	0.100±.013	0.109±.016
4 2	-.016±.010	-.016±.009	-.005±.010	-.026±.011	-.027±.009	-.000±.010	0.000±.013
4 3	-.010±.007	-.024±.007	-.009±.008	0.002±.008	-.002±.008	-.005±.008	0.000±.008
4 4	-.004±.005	-.009±.005	-.004±.006	-.011±.006	-.012±.006	-.005±.006	-.010±.008
5 0	0.031±.015	0.004±.015	0.034±.016	0.085±.017	0.111±.020	0.152±.022	0.149±.026
5 1	0.007±.017	-.002±.013	0.010±.010	0.009±.012	0.048±.011	0.090±.014	0.120±.010
5 2	0.017±.011	0.004±.010	0.030±.010	0.032±.010	-.002±.010	0.000±.012	0.000±.010
5 3	0.001±.008	0.001±.008	-.003±.009	0.014±.009	0.010±.009	-.011±.008	0.006±.008
5 4	0.011±.006	-.000±.006	0.007±.007	-.013±.007	-.007±.007	0.009±.007	0.003±.007
5 5	-.003±.005	-.007±.005	-.002±.006	-.002±.006	-.004±.007	0.000±.006	0.002±.007
6 0	0.005±.016	0.001±.015	-.006±.016	-.015±.017	0.071±.021	0.003±.020	0.070±.020
6 1	0.000±.015	-.019±.013	0.000±.010	0.003±.012	0.019±.012	0.079±.016	0.091±.021
6 2	0.001±.014	-.002±.011	0.000±.010	-.007±.011	-.033±.011	-.019±.010	-.017±.010
6 3	0.007±.009	-.015±.006	0.009±.009	0.009±.009	-.010±.010	-.015±.010	-.002±.012
6 4	-.004±.008	-.015±.007	0.012±.008	0.006±.008	-.012±.007	0.000±.008	0.000±.008
6 5	0.001±.006	-.014±.008	0.000±.007	-.007±.007	0.002±.008	-.004±.007	-.000±.007
6 6	0.004±.005	0.001±.005	0.004±.005	0.006±.006	-.012±.008	0.006±.008	0.009±.007

Table VII (b)

<Re(T(L,M))> in the t channel helicity frame for .05<t<0.08

L M	1.08<m<1.25	1.25<m<1.35	1.35<m<1.45	1.45<m<1.55	1.55<m<1.80	1.80<m<3.00
1 0	0.029 ± .012	-.041 ± .009	-.039 ± .010	-.013 ± .013	0.105 ± .013	0.093 ± .031
1 1	0.082 ± .007	0.066 ± .006	0.073 ± .005	0.066 ± .006	0.056 ± .006	0.054 ± .015
2 0	0.062 ± .011	0.021 ± .009	0.069 ± .009	0.100 ± .010	0.155 ± .011	0.109 ± .030
2 1	0.062 ± .008	0.057 ± .006	0.055 ± .007	0.068 ± .008	0.093 ± .009	0.100 ± .020
2 2	-.017 ± .007	-.003 ± .006	0.000 ± .005	0.008 ± .005	-.007 ± .005	0.013 ± .013
3 0	-.002 ± .011	0.001 ± .009	0.009 ± .010	-.011 ± .011	-.008 ± .013	0.024 ± .032
3 1	0.013 ± .008	-.002 ± .006	0.024 ± .007	0.049 ± .008	0.059 ± .009	0.076 ± .023
3 2	0.006 ± .008	0.020 ± .006	-.003 ± .006	0.014 ± .007	0.003 ± .007	0.025 ± .018
3 3	-.001 ± .007	-.003 ± .006	-.009 ± .005	-.007 ± .005	0.014 ± .005	0.004 ± .013
4 0	-.007 ± .011	-.009 ± .009	0.005 ± .009	-.008 ± .011	-.041 ± .014	-.013 ± .034
4 1	0.003 ± .008	0.017 ± .006	0.023 ± .007	0.028 ± .009	0.043 ± .009	0.086 ± .022
4 2	-.001 ± .008	0.001 ± .006	0.008 ± .007	0.001 ± .007	-.011 ± .008	0.021 ± .021
4 3	0.006 ± .008	-.000 ± .006	-.013 ± .006	-.001 ± .007	0.002 ± .007	0.008 ± .018
4 4	0.012 ± .007	-.000 ± .006	-.002 ± .005	-.005 ± .005	0.002 ± .005	-.005 ± .013
5 0	0.002 ± .011	0.004 ± .009	-.012 ± .009	-.026 ± .011	-.033 ± .014	-.068 ± .036
5 1	-.006 ± .008	0.002 ± .006	0.001 ± .007	0.001 ± .008	0.028 ± .008	0.031 ± .023
5 2	0.015 ± .008	0.007 ± .006	0.004 ± .007	0.008 ± .008	0.008 ± .009	0.045 ± .022
5 3	0.006 ± .008	0.003 ± .006	-.001 ± .006	-.008 ± .008	0.020 ± .008	-.002 ± .023
5 4	0.004 ± .007	-.008 ± .006	-.004 ± .005	-.007 ± .006	0.005 ± .007	0.007 ± .017
5 5	0.018 ± .007	0.013 ± .006	-.002 ± .005	-.002 ± .005	0.000 ± .004	0.007 ± .011
6 0	-.023 ± .011	-.004 ± .009	-.021 ± .009	-.018 ± .011	-.049 ± .014	-.054 ± .037
6 1	-.012 ± .008	0.004 ± .006	0.000 ± .007	0.005 ± .008	0.004 ± .009	0.027 ± .022
6 2	0.009 ± .008	0.005 ± .006	0.001 ± .007	0.001 ± .008	-.005 ± .009	0.000 ± .023
6 3	0.006 ± .008	0.007 ± .006	0.000 ± .006	-.000 ± .008	0.000 ± .000	-.011 ± .025
6 4	0.005 ± .008	-.008 ± .006	0.006 ± .006	-.004 ± .007	-.003 ± .008	-.005 ± .020
6 5	0.011 ± .007	-.005 ± .006	0.004 ± .005	-.001 ± .006	0.004 ± .006	0.008 ± .014
6 6	0.004 ± .007	0.013 ± .006	0.007 ± .005	0.001 ± .005	0.001 ± .004	-.007 ± .013

<Re(T(L,M))> in the t channel helicity frame for .02<t<0.05

L M	1.08<m<1.25	1.25<m<1.35	1.35<m<1.45	1.45<m<1.55	1.55<m<1.80	1.80<m<3.00
1 0	-.007 ± .009	-.049 ± .007	-.050 ± .009	-.035 ± .013	0.062 ± .013	0.072 ± .033
1 1	0.071 ± .006	0.051 ± .005	0.047 ± .005	0.045 ± .007	0.049 ± .007	0.044 ± .016
2 0	-.019 ± .009	-.024 ± .007	0.015 ± .009	0.070 ± .010	0.090 ± .012	0.090 ± .031
2 1	0.052 ± .006	0.054 ± .005	0.047 ± .005	0.051 ± .009	0.074 ± .009	0.067 ± .019
2 2	0.002 ± .006	-.011 ± .005	0.006 ± .005	0.002 ± .008	0.004 ± .006	-.007 ± .017
3 0	-.016 ± .008	-.015 ± .007	0.019 ± .009	-.017 ± .011	-.047 ± .013	-.003 ± .030
3 1	0.006 ± .006	0.001 ± .005	0.000 ± .006	0.021 ± .008	0.036 ± .009	0.053 ± .020
3 2	0.016 ± .006	0.004 ± .005	0.004 ± .005	0.015 ± .007	0.007 ± .008	-.001 ± .021
3 3	-.003 ± .006	-.003 ± .005	-.008 ± .006	-.006 ± .006	-.010 ± .005	0.016 ± .015
4 0	-.012 ± .009	-.010 ± .007	-.005 ± .009	-.036 ± .011	-.051 ± .013	-.046 ± .027
4 1	-.006 ± .006	0.007 ± .005	0.023 ± .006	0.033 ± .008	0.030 ± .009	0.033 ± .021
4 2	0.001 ± .006	0.008 ± .005	-.004 ± .005	-.000 ± .008	-.005 ± .009	-.043 ± .023
4 3	0.003 ± .006	0.001 ± .005	0.001 ± .005	-.005 ± .007	-.004 ± .007	0.027 ± .018
4 4	0.000 ± .006	0.001 ± .005	0.004 ± .004	-.011 ± .005	-.016 ± .005	0.023 ± .015
5 0	0.003 ± .009	0.002 ± .007	0.001 ± .009	-.017 ± .011	-.035 ± .013	-.030 ± .025
5 1	0.001 ± .006	0.013 ± .005	-.016 ± .006	0.014 ± .008	0.030 ± .009	0.026 ± .021
5 2	-.010 ± .006	0.004 ± .005	0.002 ± .006	0.006 ± .007	-.004 ± .009	-.020 ± .025
5 3	0.002 ± .006	0.002 ± .005	0.003 ± .005	-.013 ± .008	-.009 ± .008	-.021 ± .021
5 4	-.004 ± .006	0.001 ± .005	0.002 ± .005	-.001 ± .007	0.000 ± .007	0.033 ± .017
5 5	-.002 ± .006	-.005 ± .005	-.009 ± .004	-.012 ± .005	-.001 ± .005	0.012 ± .014
6 0	-.003 ± .009	-.006 ± .007	0.005 ± .009	-.020 ± .011	-.015 ± .012	-.021 ± .027
6 1	0.010 ± .006	-.016 ± .005	0.007 ± .006	0.014 ± .008	0.006 ± .009	-.006 ± .020
6 2	0.009 ± .006	0.002 ± .005	-.008 ± .006	-.005 ± .007	-.006 ± .009	-.057 ± .025
6 3	-.006 ± .006	-.005 ± .005	-.003 ± .005	-.003 ± .008	-.007 ± .009	-.032 ± .022
6 4	-.005 ± .006	0.013 ± .005	-.001 ± .005	-.020 ± .008	0.007 ± .008	-.033 ± .020
6 5	-.006 ± .006	0.003 ± .005	-.004 ± .005	-.004 ± .006	-.004 ± .006	-.014 ± .017
6 6	0.005 ± .006	-.003 ± .005	0.007 ± .004	0.005 ± .005	0.002 ± .005	-.018 ± .015

<Re(T(L,M))> in the t channel helicity frame for .08<t<0.12

L M	1.08<m<1.25	1.25<m<1.35	1.35<m<1.45	1.45<m<1.55	1.55<m<1.80	1.80<m<3.00
1 0	0.099 ± .015	0.030 ± .011	-.001 ± .011	0.049 ± .014	0.080 ± .013	0.107 ± .031
1 1	0.072 ± .006	0.065 ± .006	0.074 ± .005	0.063 ± .006	0.066 ± .006	0.065 ± .016
2 0	0.123 ± .015	0.095 ± .010	0.121 ± .010	0.176 ± .011	0.189 ± .012	0.100 ± .028
2 1	0.075 ± .010	0.090 ± .007	0.068 ± .006	0.099 ± .008	0.104 ± .008	0.120 ± .016
2 2	-.003 ± .006	-.002 ± .006	0.002 ± .005	0.007 ± .005	0.003 ± .005	0.018 ± .012
3 0	0.029 ± .016	-.019 ± .011	0.031 ± .011	0.001 ± .013	-.032 ± .016	0.095 ± .034
3 1	0.053 ± .010	0.038 ± .008	0.044 ± .007	0.049 ± .009	0.058 ± .008	0.081 ± .021
3 2	0.014 ± .009	0.022 ± .007	0.019 ± .006	0.030 ± .007	0.010 ± .007	0.033 ± .016
3 3	0.009 ± .008	-.012 ± .006	0.006 ± .005	0.002 ± .005	-.002 ± .005	0.016 ± .011
4 0	0.026 ± .015	0.003 ± .011	0.024 ± .011	-.006 ± .013	-.020 ± .016	0.065 ± .033
4 1	0.032 ± .011	0.029 ± .008	0.038 ± .007	0.054 ± .010	0.034 ± .008	0.121 ± .020
4 2	-.002 ± .010	0.010 ± .007	-.014 ± .006	0.002 ± .008	-.017 ± .007	0.036 ± .019
4 3	-.013 ± .009	-.001 ± .007	0.000 ± .005	0.010 ± .006	-.008 ± .007	-.015 ± .019
4 4	-.010 ± .008	-.009 ± .006	0.001 ± .005	0.009 ± .004	0.000 ± .005	-.000 ± .011
5 0	0.034 ± .015	-.015 ± .011	-.001 ± .011	-.027 ± .013	-.008 ± .016	0.007 ± .033
5 1	0.007 ± .011	0.009 ± .008	0.034 ± .007	0.011 ± .010	0.018 ± .008	0.093 ± .022
5 2	0.013 ± .010	0.001 ± .007	0.016 ± .007	0.007 ± .009	-.005 ± .008	0.027 ± .021
5 3	0.007 ± .010	0.003 ± .007	-.009 ± .006	-.005 ± .007	0.000 ± .007	0.011 ± .016
5 4	-.002 ± .009	-.006 ± .006	0.000 ± .005	-.005 ± .006	0.004 ± .006	-.006 ± .013
5 5	-.002 ± .008	-.003 ± .006	0.006 ± .005	0.009 ± .004	-.008 ± .004	-.007 ± .011
6 0	0.017 ± .015	-.011 ± .011	-.006 ± .011	-.021 ± .012	-.008 ± .015	0.005 ± .031
6 1	0.020 ± .011	0.008 ± .008	0.007 ± .007	0.015 ± .009	-.003 ± .009	0.063 ± .023
6 2	-.002 ± .010	0.025 ± .007	0.000 ± .007	0.011 ± .009	-.031 ± .008	0.022 ± .023
6 3	0.008 ± .010	-.003 ± .007	-.010 ± .006	0.010 ± .008	-.015 ± .007	0.025 ± .019
6 4	-.007 ± .009	-.003 ± .007	-.007 ± .006	-.001 ± .007	0.012 ± .007	0.012 ± .015
6 5	0.011 ± .009	0.002 ± .006	-.004 ± .005	-.000 ± .005	-.007 ± .006	0.026 ± .012
6 6	0.005 ± .008	-.002 ± .006	0.004 ± .005	0.004 ± .005	0.001 ± .004	0.009 ± .011

<Re(T(L,M))> in the t channel helicity frame for .12<t<0.20

L M	1.08<m<1.25	1.25<m<1.35	1.35<m<1.45	1.45<m<1.55	1.55<m<1.80	1.80<m<3.00
1 0	0.187 ± .019	0.106 ± .014	0.081 ± .012	0.075 ± .012	0.108 ± .011	0.210 ± .027
1 1	0.081 ± .009	0.086 ± .006	0.070 ± .006	0.071 ± .005	0.055 ± .005	0.062 ± .009
2 0	0.212 ± .018	0.170 ± .013	0.188 ± .010	0.178 ± .010	0.182 ± .009	0.243 ± .022
2 1	0.085 ± .012	0.115 ± .009	0.109 ± .009	0.099 ± .007	0.107 ± .008	0.110 ± .013
2 2	-.010 ± .009	-.003 ± .006	0.010 ± .005	0.004 ± .005	0.003 ± .006	-.000 ± .008
3 0	0.053 ± .020	0.020 ± .015	0.023 ± .012	0.022 ± .013	0.027 ± .012	0.189 ± .027
3 1	0.092 ± .013	0.077 ± .009	0.068 ± .009	0.068 ± .006	0.057 ± .009	0.126 ± .018
3 2	0.008 ± .011	0.028 ± .008	0.031 ± .006	0.028 ± .006	0.028 ± .005	0.002 ± .012
3 3	-.002 ± .009	-.009 ± .006	0.000 ± .005	0.007 ± .006	0.001 ± .003	0.001 ± .008
4 0	0.023 ± .035	0.011 ± .015	0.025 ± .013	-.003 ± .013	0.015 ± .012	0.123 ± .027
4 1	0.060 ± .014	0.056 ± .010	0.066 ± .008	0.036 ± .008	0.031 ± .010	0.130 ± .016
4 2	0.007 ± .012	0.010 ± .009	0.008 ± .007	0.008 ± .007	-.002 ± .008	0.020 ± .016
4 3	-.023 ± .011	-.016 ± .007	0.003 ± .006	0.006 ± .006	-.013 ± .005	-.008 ± .010
4 4	-.010 ± .009	-.001 ± .006	-.002 ± .005	0.002 ± .004	-.006 ± .003	-.012 ± .008
5 0	0.017 ± .020	-.014 ± .015	0.012 ± .013	0.000 ± .012	0.028 ± .011	0.081 ± .026
5 1	0.033 ± .014	0.033 ± .010	0.035 ± .008	0.011 ± .009	0.009 ± .010	0.120 ± .018
5 2	0.005 ± .013	0.013 ± .010	0.016 ± .007	0.006 ± .007	0.019 ± .007	0.005 ± .017
5 3	-.012 ± .011	-.009 ± .008	-.008 ± .007	-.008 ± .006	-.012 ± .006	0.001 ± .011
5 4	-.011 ± .011	-.017 ± .007	0.004 ± .006	0.001 ± .005	-.002 ± .004	0.018 ± .009
5 5	-.008 ± .009	0.001 ± .006	-.009 ± .004	-.007 ± .004	-.003 ± .003	-.001 ± .008
6 0	-.016 ± .024	0.005 ± .015	0.017 ± .013	0.009 ± .012	0.002 ± .017	0.069 ± .026
6 1	0.062 ± .013	0.020 ± .009	0.021 ± .009	-.003 ± .009	-.002 ± .010	0.091 ± .020
6 2	0.004 ± .014	0.012 ± .010	-.004 ± .008	-.007 ± .008	-.001 ± .009	0.005 ± .020
6 3	0.007 ± .012	-.003 ± .009	0.003 ± .007	0.000 ± .007	-.010 ± .006	-.005 ± .013
6 4	-.013 ± .011	-.004 ± .008	0.002 ± .007	-.002 ± .006	-.006 ± .005	0.019 ± .010
6 5	0.004 ± .010	0.001 ± .007	-.001 ± .006	0.002 ± .005	-.002 ± .004	0.001 ± .009
6 6	-.019 ± .010	0.002 ± .006	-.002 ± .006	0.003 ± .004	-.003 ± .003	-.002 ± .007

Table VII (c)

<Re(T(L,M))> in the t channel helicity frame for .20<t<0.40

L M	1.08<m<1.25	1.25<m<1.35	1.35<m<1.45	1.45<m<1.55	1.55<m<1.80	1.80<m<3.00
1 0	0.117 ± .018	0.192 ± .014	0.155 ± .013	0.116 ± .011	0.109 ± .009	0.267 ± .016
1 1	0.100 ± .010	0.098 ± .009	0.077 ± .006	0.088 ± .006	0.080 ± .005	0.051 ± .007
2 0	0.148 ± .018	0.225 ± .015	0.231 ± .012	0.190 ± .011	0.175 ± .008	0.290 ± .018
2 1	0.059 ± .012	0.096 ± .012	0.107 ± .009	0.087 ± .008	0.092 ± .007	0.100 ± .009
2 2	-.012 ± .010	-.008 ± .008	0.002 ± .006	-.016 ± .005	-.031 ± .004	-.029 ± .007
3 0	0.061 ± .010	0.099 ± .017	0.048 ± .015	0.034 ± .012	0.045 ± .010	0.255 ± .023
3 1	0.067 ± .013	0.082 ± .012	0.085 ± .010	0.085 ± .009	0.081 ± .007	0.163 ± .012
3 2	0.011 ± .011	-.001 ± .010	0.025 ± .007	0.017 ± .006	0.007 ± .005	-.021 ± .009
3 3	-.015 ± .010	-.006 ± .007	-.001 ± .005	-.003 ± .005	0.001 ± .003	0.002 ± .007
4 0	0.029 ± .018	0.037 ± .017	0.058 ± .015	0.032 ± .012	0.021 ± .010	0.217 ± .025
4 1	0.015 ± .012	0.048 ± .011	0.048 ± .011	0.037 ± .009	0.025 ± .007	0.116 ± .013
4 2	-.015 ± .012	0.004 ± .011	0.015 ± .008	-.005 ± .008	-.025 ± .006	0.000 ± .011
4 3	0.002 ± .011	-.018 ± .009	0.003 ± .007	0.011 ± .006	-.012 ± .005	0.003 ± .008
4 4	-.024 ± .010	-.001 ± .007	-.007 ± .005	-.001 ± .004	-.002 ± .003	0.000 ± .006
5 0	0.033 ± .019	0.006 ± .017	0.050 ± .015	0.037 ± .012	0.045 ± .010	0.160 ± .027
5 1	0.036 ± .012	0.011 ± .012	0.010 ± .011	0.010 ± .009	0.025 ± .007	0.124 ± .016
5 2	-.004 ± .012	0.003 ± .011	0.004 ± .009	-.000 ± .008	0.018 ± .006	-.001 ± .013
5 3	-.017 ± .012	-.001 ± .010	-.011 ± .007	-.003 ± .007	0.001 ± .005	0.000 ± .009
5 4	0.005 ± .011	-.012 ± .008	-.009 ± .006	0.008 ± .005	-.001 ± .004	0.007 ± .006
5 5	-.010 ± .010	-.002 ± .007	-.010 ± .005	0.003 ± .004	-.003 ± .003	0.004 ± .006
6 0	-.008 ± .019	0.001 ± .017	0.024 ± .015	0.011 ± .012	0.019 ± .010	0.086 ± .030
6 1	0.014 ± .012	-.006 ± .012	0.019 ± .011	0.009 ± .009	0.011 ± .007	0.105 ± .015
6 2	-.015 ± .012	0.002 ± .011	0.006 ± .010	-.005 ± .009	-.008 ± .006	-.022 ± .015
6 3	-.009 ± .012	0.005 ± .010	-.009 ± .008	-.001 ± .009	-.003 ± .005	-.011 ± .011
6 4	-.000 ± .011	-.003 ± .009	-.006 ± .007	-.004 ± .006	-.001 ± .005	-.001 ± .008
6 5	0.006 ± .010	-.009 ± .008	-.004 ± .006	0.004 ± .005	-.002 ± .004	-.008 ± .007
6 6	-.004 ± .010	0.006 ± .007	0.005 ± .005	0.006 ± .004	0.003 ± .003	0.006 ± .006

<Re(T(L,M))> in the t channel helicity frame for .40<t<0.60

L M	1.08<m<1.25	1.25<m<1.35	1.35<m<1.45	1.45<m<1.55	1.55<m<1.80	1.80<m<3.00
1 0	0.062 ± .026	0.125 ± .025	0.083 ± .020	0.107 ± .019	0.116 ± .015	0.322 ± .027
1 1	0.114 ± .018	0.075 ± .020	0.087 ± .011	0.041 ± .010	0.030 ± .009	0.057 ± .019
2 0	0.028 ± .028	0.053 ± .021	0.108 ± .019	0.132 ± .019	0.151 ± .015	0.395 ± .036
2 1	0.026 ± .024	0.001 ± .034	0.019 ± .015	0.049 ± .013	0.063 ± .011	0.092 ± .021
2 2	-.034 ± .019	0.003 ± .018	-.018 ± .011	-.045 ± .009	-.028 ± .008	-.036 ± .017
3 0	0.092 ± .031	-.014 ± .022	0.019 ± .021	0.063 ± .020	0.068 ± .017	0.313 ± .042
3 1	0.096 ± .019	0.010 ± .031	0.058 ± .015	0.046 ± .013	0.019 ± .010	0.083 ± .026
3 2	-.031 ± .019	0.033 ± .026	-.012 ± .013	0.002 ± .011	0.018 ± .010	-.018 ± .016
3 3	-.058 ± .020	-.018 ± .013	-.010 ± .011	-.012 ± .009	-.001 ± .007	-.001 ± .015
4 0	0.032 ± .029	-.014 ± .033	0.011 ± .021	0.024 ± .020	0.044 ± .017	0.284 ± .038
4 1	0.081 ± .021	-.010 ± .016	0.016 ± .015	0.015 ± .013	0.078 ± .010	0.098 ± .031
4 2	0.012 ± .018	0.033 ± .035	0.023 ± .014	0.019 ± .012	-.017 ± .010	0.007 ± .019
4 3	-.012 ± .020	-.003 ± .022	-.004 ± .013	0.008 ± .010	-.006 ± .009	0.004 ± .012
4 4	-.062 ± .020	0.005 ± .011	-.002 ± .010	-.008 ± .009	-.012 ± .006	-.022 ± .013
5 0	0.014 ± .028	-.031 ± .032	-.020 ± .021	0.021 ± .020	0.076 ± .015	0.202 ± .044
5 1	-.013 ± .021	0.049 ± .018	0.006 ± .015	0.013 ± .014	0.012 ± .012	0.096 ± .035
5 2	0.000 ± .018	0.016 ± .023	0.019 ± .014	0.011 ± .013	0.008 ± .010	0.016 ± .025
5 3	-.010 ± .019	-.011 ± .027	-.010 ± .013	-.007 ± .011	0.021 ± .009	-.014 ± .015
5 4	-.008 ± .020	0.023 ± .014	-.012 ± .012	0.014 ± .011	0.008 ± .007	-.017 ± .012
5 5	-.011 ± .020	0.004 ± .011	-.008 ± .010	0.005 ± .009	-.002 ± .006	0.008 ± .010
6 0	0.019 ± .028	-.048 ± .039	-.033 ± .022	-.001 ± .021	0.001 ± .016	0.125 ± .040
6 1	-.002 ± .020	0.025 ± .031	-.003 ± .014	-.010 ± .014	-.009 ± .011	0.083 ± .040
6 2	0.029 ± .019	0.012 ± .013	0.004 ± .014	0.019 ± .013	-.038 ± .011	-.006 ± .027
6 3	0.018 ± .019	-.002 ± .026	0.014 ± .013	0.009 ± .012	0.007 ± .009	-.021 ± .021
6 4	-.005 ± .019	0.005 ± .019	-.014 ± .013	-.001 ± .012	0.009 ± .008	-.003 ± .012
6 5	0.023 ± .021	0.010 ± .012	-.001 ± .012	0.011 ± .010	0.001 ± .007	-.008 ± .009
6 6	0.006 ± .020	-.024 ± .013	-.017 ± .010	-.002 ± .010	0.001 ± .006	0.004 ± .009

<Re(T(L,M))> in the t channel helicity frame for .60<t<1.00

L M	1.08<m<1.25	1.25<m<1.35	1.35<m<1.45	1.45<m<1.55	1.55<m<1.80	1.80<m<3.00
1 0	0.051 ± .040	0.063 ± .027	0.105 ± .035	0.042 ± .031	0.164 ± .026	0.291 ± .042
1 1	0.046 ± .024	0.134 ± .023	0.102 ± .023	0.073 ± .017	0.053 ± .022	0.039 ± .014
2 0	-.018 ± .043	-.009 ± .027	0.041 ± .036	-.002 ± .033	0.120 ± .020	0.363 ± .030
2 1	0.003 ± .026	0.055 ± .027	0.033 ± .027	0.023 ± .021	0.023 ± .020	0.070 ± .023
2 2	-.123 ± .028	0.007 ± .022	-.051 ± .024	-.044 ± .017	-.057 ± .019	-.031 ± .012
3 0	-.013 ± .043	-.037 ± .030	0.031 ± .038	-.051 ± .035	0.082 ± .031	0.237 ± .056
3 1	-.009 ± .027	0.012 ± .022	0.035 ± .025	0.022 ± .022	-.026 ± .022	0.110 ± .025
3 2	-.060 ± .027	0.027 ± .023	0.022 ± .024	-.012 ± .019	-.022 ± .020	-.021 ± .018
3 3	-.076 ± .025	-.008 ± .021	-.034 ± .022	-.012 ± .018	-.027 ± .015	0.014 ± .016
4 0	0.027 ± .045	0.002 ± .030	-.047 ± .038	-.001 ± .033	0.056 ± .034	0.249 ± .054
4 1	-.023 ± .026	-.024 ± .023	-.001 ± .025	0.002 ± .023	0.002 ± .019	0.125 ± .033
4 2	0.012 ± .027	0.023 ± .021	0.006 ± .025	0.031 ± .019	-.065 ± .023	-.055 ± .022
4 3	0.016 ± .025	-.008 ± .022	0.011 ± .024	0.000 ± .019	0.005 ± .015	0.026 ± .020
4 4	0.018 ± .029	0.010 ± .020	-.014 ± .021	-.028 ± .017	-.021 ± .015	-.013 ± .013
5 0	0.063 ± .045	0.038 ± .030	-.008 ± .038	0.009 ± .032	0.061 ± .033	0.184 ± .057
5 1	-.006 ± .027	-.049 ± .025	0.005 ± .026	0.001 ± .022	-.019 ± .022	0.160 ± .032
5 2	0.003 ± .026	-.014 ± .021	-.032 ± .024	0.012 ± .021	-.008 ± .020	-.023 ± .027
5 3	0.038 ± .029	0.047 ± .022	-.034 ± .025	0.008 ± .016	0.033 ± .019	-.009 ± .021
5 4	0.037 ± .031	-.007 ± .021	-.013 ± .023	-.024 ± .019	0.005 ± .015	-.014 ± .016
5 5	0.005 ± .027	-.001 ± .019	-.008 ± .021	0.017 ± .018	-.007 ± .016	0.002 ± .012
6 0	0.025 ± .045	0.010 ± .028	0.004 ± .037	0.054 ± .033	-.009 ± .031	0.159 ± .060
6 1	-.053 ± .027	-.034 ± .025	-.009 ± .026	-.006 ± .021	-.019 ± .023	0.109 ± .037
6 2	-.008 ± .027	0.030 ± .020	-.012 ± .024	0.030 ± .023	-.001 ± .020	-.028 ± .032
6 3	-.006 ± .027	0.048 ± .022	-.027 ± .024	0.004 ± .019	0.037 ± .018	-.050 ± .025
6 4	-.031 ± .030	-.002 ± .020	-.034 ± .026	0.001 ± .018	-.022 ± .010	-.022 ± .016
6 5	0.021 ± .026	-.006 ± .020	0.001 ± .023	0.014 ± .020	-.015 ± .017	-.009 ± .014
6 6	-.005 ± .029	-.001 ± .019	0.010 ± .021	0.022 ± .017	-.004 ± .017	0.020 ± .013

Table VII (d)

<Re(Y(L,B))> in the a channel helicity frame for .02<t<0.12

L B	1.08<m<1.16	1.18<m<1.23	1.23<m<1.27	1.27<m<1.33	1.33<m<1.35	1.35<m<1.37	1.37<m<1.39	1.39<m<1.42	1.42<m<1.45
1 0	-.054±.009	-.073±.006	-.076±.008	-.033±.006	-.085±.010	-.077±.010	-.075±.011	-.081±.011	-.076±.011
1 1	0.066±.007	0.061±.008	0.062±.007	0.031±.005	0.033±.008	0.062±.007	0.034±.007	0.033±.007	0.043±.007
2 0	-.059±.039	-.083±.009	-.096±.009	-.076±.006	-.079±.015	-.065±.010	-.043±.011	-.037±.010	-.016±.010
2 1	-.002±.007	0.021±.007	0.011±.007	0.027±.005	0.036±.008	0.043±.007	0.065±.008	0.057±.007	0.070±.007
2 2	0.033±.007	0.046±.007	0.036±.007	0.032±.004	0.025±.007	0.033±.006	0.036±.006	0.046±.006	0.047±.006
3 0	-.016±.010	-.007±.009	0.016±.009	0.006±.006	-.013±.010	0.003±.009	-.009±.010	-.016±.009	-.012±.010
3 1	-.007±.007	-.003±.007	-.027±.006	-.012±.004	-.028±.008	-.005±.008	0.002±.008	0.003±.008	0.003±.008
3 2	-.003±.007	-.008±.007	0.002±.007	0.006±.004	0.007±.007	0.007±.007	0.020±.007	0.017±.007	0.023±.007
3 3	0.011±.008	0.007±.007	0.055±.007	0.008±.005	0.007±.008	-.002±.006	0.022±.006	0.004±.006	0.012±.006
4 0	0.005±.010	0.015±.009	0.008±.009	0.000±.006	-.033±.010	-.018±.010	-.032±.010	-.016±.009	-.044±.010
4 1	-.013±.007	0.002±.007	-.008±.006	-.016±.004	-.013±.007	-.009±.008	-.003±.008	-.018±.008	-.027±.008
4 2	-.011±.007	-.007±.007	-.016±.006	-.009±.004	-.009±.007	0.006±.007	0.025±.007	0.010±.007	0.004±.007
4 3	-.013±.007	0.004±.007	0.005±.007	0.003±.004	0.007±.007	0.006±.007	0.006±.007	0.005±.006	0.013±.007
4 4	0.008±.008	-.005±.007	0.005±.007	0.007±.005	0.006±.008	-.001±.006	0.001±.006	0.005±.006	0.005±.006
5 0	-.012±.010	-.003±.009	0.012±.009	-.010±.006	-.001±.010	0.007±.010	0.037±.010	0.012±.009	0.006±.010
5 1	-.008±.007	0.005±.007	-.002±.006	-.001±.004	-.003±.007	0.000±.007	-.004±.008	0.004±.008	-.010±.007
5 2	0.002±.007	-.006±.006	-.007±.006	0.003±.004	-.009±.007	-.009±.007	-.022±.007	-.005±.007	0.007±.007
5 3	0.002±.007	0.008±.007	0.001±.006	0.006±.004	-.006±.007	-.000±.007	0.000±.007	-.006±.007	0.005±.007
5 4	0.005±.007	0.004±.007	-.000±.007	0.005±.004	0.002±.008	-.002±.007	0.019±.007	0.003±.006	0.007±.007
5 5	0.004±.007	-.004±.007	0.014±.007	0.009±.005	-.019±.008	0.005±.006	-.002±.006	-.008±.006	0.001±.006
6 0	0.017±.010	-.009±.009	0.012±.009	0.007±.006	0.011±.010	-.006±.010	0.018±.010	-.005±.009	0.007±.010
6 1	0.007±.007	-.000±.006	0.013±.006	0.010±.004	0.003±.008	-.006±.007	0.008±.006	0.007±.008	-.012±.007
6 2	0.002±.007	-.001±.006	0.002±.006	-.006±.004	0.018±.007	0.004±.007	-.005±.007	0.013±.007	-.016±.007
6 3	0.001±.007	-.017±.007	0.002±.006	0.000±.004	-.024±.007	-.007±.007	0.007±.007	0.003±.007	-.012±.007
6 4	0.007±.007	0.003±.007	0.002±.007	0.000±.004	-.005±.008	0.002±.007	-.001±.007	0.006±.007	0.005±.007
6 5	-.006±.007	0.002±.007	-.002±.007	-.001±.004	0.022±.008	-.001±.006	0.000±.007	-.010±.006	-.011±.006
6 6	-.004±.008	0.004±.007	0.006±.007	0.005±.005	0.002±.007	-.001±.006	0.003±.006	0.006±.006	-.004±.006

<Re(Y(L,B))> in the a channel helicity frame for .02<t<0.12

L B	1.45<m<1.48	1.48<m<1.51	1.51<m<1.55	1.55<m<1.60	1.60<m<1.65	1.65<m<1.70	1.70<m<1.80	1.80<m<2.20
1 0	-.064±.012	-.073±.013	0.005±.012	0.049±.013	0.038±.013	0.029±.016	0.030±.017	0.068±.018
1 1	0.031±.007	0.048±.008	0.073±.007	0.095±.008	0.076±.008	0.068±.008	0.057±.009	0.083±.011
2 0	-.004±.011	-.009±.012	-.016±.011	-.022±.013	0.002±.011	0.030±.014	0.026±.015	0.023±.016
2 1	0.079±.008	0.095±.008	0.097±.007	0.108±.009	0.115±.009	0.148±.008	0.099±.011	0.115±.012
2 2	0.058±.006	0.058±.006	0.052±.006	0.063±.007	0.056±.007	0.045±.007	0.032±.008	0.042±.010
3 0	-.027±.010	-.033±.012	-.050±.010	-.060±.012	-.094±.010	-.076±.014	-.033±.014	-.023±.014
3 1	-.015±.008	-.032±.009	-.011±.008	-.005±.010	-.019±.010	-.010±.013	0.006±.013	0.053±.014
3 2	0.027±.007	0.023±.007	0.031±.008	0.022±.009	0.021±.009	0.025±.009	0.017±.010	0.038±.012
3 3	0.011±.006	0.016±.006	0.016±.006	0.010±.007	0.009±.007	0.010±.007	0.013±.007	0.026±.009
4 0	-.039±.009	-.038±.012	-.051±.011	-.062±.011	-.082±.011	-.065±.013	-.066±.013	-.083±.014
4 1	-.014±.009	-.043±.008	-.037±.008	-.036±.010	-.031±.009	-.006±.013	0.006±.013	0.016±.014
4 2	0.012±.007	-.007±.008	-.006±.008	-.008±.009	-.008±.009	0.010±.010	0.011±.012	0.027±.013
4 3	0.028±.007	0.008±.007	-.006±.007	0.005±.008	-.018±.009	0.008±.009	0.012±.009	0.012±.011
4 4	0.005±.006	-.002±.007	0.002±.006	0.009±.007	-.016±.007	-.006±.006	-.008±.008	0.006±.009
5 0	0.016±.009	0.015±.012	-.008±.011	-.012±.011	-.040±.011	-.025±.013	-.039±.013	-.043±.015
5 1	-.027±.009	-.012±.008	-.001±.008	-.018±.009	-.029±.009	-.009±.012	-.015±.012	-.024±.013
5 2	-.003±.008	-.017±.008	-.001±.008	-.003±.010	-.005±.009	0.000±.011	0.006±.013	0.020±.013
5 3	0.012±.007	-.001±.008	-.010±.008	0.001±.009	-.013±.009	0.005±.010	0.009±.011	0.005±.013
5 4	0.009±.007	-.008±.007	-.012±.007	-.000±.008	-.003±.008	0.015±.008	0.021±.009	0.017±.011
5 5	-.008±.006	-.001±.006	-.014±.006	-.002±.007	-.000±.006	0.005±.007	0.001±.007	0.008±.009
6 0	-.014±.010	0.010±.012	0.001±.010	-.009±.012	0.001±.012	-.006±.014	-.020±.015	-.052±.017
6 1	-.010±.006	0.002±.008	-.011±.009	-.011±.008	-.025±.009	-.007±.012	-.013±.011	-.019±.012
6 2	-.016±.009	-.015±.008	-.012±.009	-.001±.011	-.019±.009	0.012±.011	0.013±.013	-.005±.012
6 3	-.001±.007	-.011±.008	0.004±.008	-.005±.009	-.025±.009	-.027±.010	0.004±.012	0.000±.014
6 4	0.003±.007	-.007±.007	0.006±.008	-.010±.008	-.022±.009	-.004±.009	-.003±.010	-.018±.013
6 5	0.002±.006	-.008±.007	-.011±.007	-.001±.007	-.010±.007	-.009±.008	-.006±.008	-.013±.011
6 6	0.001±.006	0.000±.006	-.001±.006	0.008±.007	0.002±.006	-.005±.006	-.010±.007	-.005±.009

<Re(Y(L,B))> in the a channel helicity frame for .12<t<1.00

L B	1.08<m<1.24	1.24<m<1.30	1.30<m<1.35	1.35<m<1.40	1.40<m<1.44	1.44<m<1.48	1.48<m<1.51	1.51<m<1.54	1.54<m<1.58
1 0	-.084±.010	-.083±.010	-.066±.017	-.050±.011	-.038±.010	-.030±.009	-.010±.011	0.015±.010	0.030±.011
1 1	0.098±.008	0.117±.008	0.121±.008	0.109±.007	0.103±.008	0.080±.008	0.002±.008	0.005±.008	0.099±.007
2 0	-.113±.010	-.104±.011	-.113±.018	-.104±.011	-.114±.010	-.103±.009	-.087±.012	-.091±.010	-.095±.012
2 1	0.003±.038	0.018±.069	0.028±.012	0.058±.006	0.071±.008	0.070±.007	0.090±.008	0.099±.008	0.002±.007
2 2	0.068±.008	0.101±.008	0.105±.007	0.113±.007	0.122±.007	0.116±.007	0.082±.007	0.090±.007	0.080±.007
3 0	0.050±.010	0.058±.011	0.006±.011	0.010±.010	-.021±.010	-.006±.009	-.024±.010	-.028±.010	-.008±.012
3 1	-.057±.008	-.048±.009	-.048±.016	-.051±.008	-.055±.008	-.051±.008	-.035±.010	-.017±.009	-.019±.009
3 2	-.002±.008	-.003±.008	0.010±.009	0.005±.007	0.019±.006	0.012±.007	0.026±.008	0.013±.008	0.038±.008
3 3	0.042±.009	0.045±.008	0.042±.008	0.050±.007	0.054±.008	0.050±.007	0.035±.007	0.023±.008	0.041±.007
4 0	-.002±.011	0.017±.010	0.004±.010	0.007±.009	0.003±.010	-.010±.009	-.016±.010	-.013±.010	-.004±.011
4 1	-.002±.008	-.025±.009	-.014±.010	-.022±.008	-.023±.008	-.018±.008	-.028±.010	-.013±.009	-.024±.009
4 2	-.031±.008	-.018±.008	-.022±.012	-.017±.008	-.012±.008	-.018±.007	-.011±.009	0.002±.008	-.004±.008
4 3	0.006±.008	0.020±.008	0.023±.007	0.013±.007	0.031±.008	0.018±.007	0.017±.007	0.008±.008	-.001±.008
4 4	0.010±.009	0.012±.008	0.024±.006	0.018±.008	0.036±.008	0.043±.007	0.020±.007	-.005±.008	-.015±.007
5 0	0.017±.015	0.010±.010	-.006±.013	0.028±.009	0.010±.010	0.008±.009	0.022±.010	-.008±.011	0.012±.011
5 1	0.029±.008	0.006±.009	0.026±.011	0.011±.008	-.013±.008	-.003±.008	-.003±.010	-.009±.009	-.013±.008
5 2	0.001±.008	-.007±.008	-.009±.013	-.010±.008	-.007±.008	0.002±.007	-.019±.009	0.002±.008	-.010±.008
5 3	-.015±.008	-.007±.008	-.009±.008	-.005±.007	0.012±.008	0.002±.007	0.001±.009	0.003±.008	0.000±.008
5 4	0.014±.008	-.005±.008	0.007±.007	0.020±.007	0.027±.008	0.011±.007	-.002±.007	0.018±.008	0.009±.008
5 5	0.018±.009	0.001±.009	-.001±.008	-.005±.008	0.014±.008	0.014±.007	-.003±.008	0.007±.008	-.000±.007
6 0	-.001±.010	-.009±.010	0.003±.016	0.003±.010	0.013±.010	-.013±.009	0.009±.011	-.005±.010	0.013±.010
6 1	0.006±.008	0.010±.008	-.003±.008	0.007±.008	0.003±.008	-.013±.007	0.002±.009	-.012±.009	-.007±.008
6 2	0.002±.008	-.010±.008	0.007±.012	-.009±.008	-.010±.008	-.006±.007	0.005±.009	-.006±.008	-.010±.008
6 3	-.009±.008	-.008±.008	-.001±.009	-.003±.008	-.009±.008	-.008±.007	-.008±.008	0.003±.008	-.004±.008
6 4	-.018±.008	-.008±.008	0.007±.007	-.002±.007	0.010±.008	0.002±.007	0.006±.008	0.009±.009	-.003±.007
6 5	-.002±.008	-.005±.008	0.005±.007	0.007±.007	0.015±.008	0.009±.007	-.004±.007	-.003±.008	-.003±.008
6 6	0.000±.009	0.004±.008	-.006±.008	-.008±.008	0.007±.008	0.012±.007	-.005±.007	0.010±.008	-.011±.007

<Re(Y(L,B))> in the a channel helicity frame for .12<t<1.00

L B	1.58<m<1.62	1.62<m<1.65	1.65<m<1.68	1.68<m<1.72	1.72<m<1.79	1.79<m<1.92	1.92<m<2.20
1 0	0.063±.016	0.030±.013	0.009±.013	-.027±.017	0.052±.013	0.135±.013	0.169±.016
1 1	0.112±.008	0.092±.008	0.068±.009	0.069±.009	0.089±.010	0.162±.010	0.163±.011
2 0	-.072±.020	-.087±.016	-.071±.013	-.139±.020	-.050±.012	-.030±.014	0.009±.010
2 1	0.117±.009	0.117±.008	0.101±.008	0.093±.009	0.123±.010	0.187±.011	0.219±.014
2 2	0.094±.007	0.094±.007	0.084±.008	0.066±.009	0.068±.009	0.102±.009	0.096±.010
3 0	-.031±.018	-.027±.014	-.019±.013	-.050±.017	-.051±.011	-.119±.012	-.112±.016
3 1	-.012±.014	-.018±.011	-.015±.010	-.035±.011	0.023±.011	0.059±.014	0.127±.010
3 2	0.043±.008	0.029±.008	0.026±.008	0.040±.010	0.047±.011	0.125±.011	0.180±.013
3 3	0.042±.007	0.024±.007	0.016±.008	0.042±.009	0.026±.009	0.054±.009	0.061±.010
4 0	-.006±.015	0.002±.018	-.015±.013	-.045±.016	-.079±.013	-.101±.013	-.186±.018
4 1	-.028±.017	-.020±.012	-.024±.010	-.047±.011	-.014±.010	-.030±.013	0.014±.010
4 2	-.000±.009	0.008±.009	0.006±.009	-.008±.010	0.047±.011	0.085±.012	0.121±.014
4 3	0.012±.008	0.009±.008	0.008±.008	0.030±.009	0.045±.010	0.091±.011	0.108±.013
4 4	-.010±.007	-.026±.008	-.008±.008	-.011±.009	0.002±.009	0.032±.009	0.030±.010
5 0	0.017±.011	0.018±.013	0.015±.013	-.007±.015	-.037±.014	-.052±.015	-.086±.017
5 1	-.003±.017	-.006±.012	-.007±.010	-.016±.009	-.036±.009	-.075±.012	-.069±.017
5 2	0.005±.011	0.002±.009	0.005±.009	-.005±.010	0.013±.011	0.025±.012	0.038±.016
5 3	0.017±.008	-.002±.008	0.021±.008	0.035±.009	0.043±.011	0.005±.012	0.003±.015
5 4	0.018±.008	0.001±.008	0.026±.008	0.049±.009	0.040±.010	0.051±.012	0.069±.013
5 5	0.013±.007	-.001±.008	0.019±.008	0.023±.009	0.016±.009	0.029±.009	0.020±.009
6 0	0.009±.011	0.038±.013	0.000±.012	0.024±.014	-.009±.013	0.017±.017	-.009±.021
6 1	-.001±.016	0.013±.013	-.011±.011	-.009±.009	-.045±.011	-.044±.011	-.084±.015
6 2	-.008±.013	0.012±.010	0.007±.009	-.007±.011	-.016±.009	-.023±.012	-.024±.017
6 3	-.009±.009	0.009±.009	0.002±.009	-.008±.009	0.036±.011	0.027±.012	0.027±.015
6 4	0.009±.008	0.007±.008	-.009±.008	-.008±.009	0.008±.011	0.041±.013	0.053±.016
6 5	0.001±.008	-.013±.008	-.002±.008	-.004±.009	0.001±.010	0.019±.012	0.023±.013
6 6	0.002±.007	-.027±.008	0.013±.008	0.000±.008	-.012±.009	0.005±.008	0.007±.009

Table VII (e)

<Re(T(L,M))> in the s channel helicity frame for .02<t<0.05

L M	1.00<m<1.25	1.25<m<1.35	1.35<m<1.45	1.45<m<1.55	1.55<m<1.80	1.80<m<3.00
1 0	-.071 ± .008	-.000 ± .007	-.074 ± .008	-.057 ± .012	0.035 ± .013	0.055 ± .032
1 1	0.050 ± .006	0.026 ± .005	0.026 ± .005	0.032 ± .007	0.041 ± .007	0.054 ± .018
2 0	-.067 ± .008	-.076 ± .007	-.033 ± .008	0.000 ± .011	0.020 ± .011	0.045 ± .027
2 1	-.002 ± .006	0.017 ± .005	0.024 ± .006	0.066 ± .008	0.091 ± .009	0.007 ± .020
2 2	0.022 ± .007	0.010 ± .005	0.026 ± .005	0.027 ± .006	0.033 ± .006	0.011 ± .019
3 0	0.002 ± .009	-.008 ± .007	0.012 ± .008	-.026 ± .011	-.060 ± .010	-.043 ± .026
3 1	-.026 ± .006	-.011 ± .005	0.007 ± .006	-.010 ± .008	-.008 ± .010	0.064 ± .023
3 2	0.003 ± .006	0.000 ± .005	0.009 ± .005	0.021 ± .007	0.039 ± .008	0.012 ± .022
3 3	0.007 ± .007	-.002 ± .005	-.000 ± .005	0.004 ± .006	-.004 ± .006	0.017 ± .016
4 0	0.014 ± .008	-.004 ± .007	-.028 ± .007	-.050 ± .011	-.064 ± .011	-.007 ± .023
4 1	0.001 ± .006	-.010 ± .005	-.003 ± .006	-.021 ± .008	-.014 ± .009	0.023 ± .022
4 2	-.012 ± .006	0.000 ± .005	0.008 ± .006	0.006 ± .008	0.002 ± .009	-.030 ± .023
4 3	-.005 ± .006	0.003 ± .005	0.002 ± .005	0.009 ± .007	0.002 ± .008	-.003 ± .019
4 4	0.001 ± .007	0.008 ± .005	0.009 ± .005	-.010 ± .006	-.017 ± .006	0.026 ± .016
5 0	-.015 ± .006	-.007 ± .007	0.016 ± .008	-.009 ± .010	-.049 ± .011	-.055 ± .028
5 1	-.006 ± .006	-.005 ± .005	0.008 ± .006	-.020 ± .009	-.016 ± .009	0.004 ± .019
5 2	-.000 ± .006	0.003 ± .005	-.003 ± .006	0.000 ± .008	0.008 ± .009	0.005 ± .032
5 3	-.000 ± .006	0.005 ± .005	-.008 ± .005	0.000 ± .007	-.006 ± .009	-.008 ± .021
5 4	0.000 ± .006	0.007 ± .005	0.006 ± .005	0.002 ± .006	-.006 ± .007	0.010 ± .020
5 5	-.006 ± .007	-.001 ± .005	-.005 ± .005	-.013 ± .006	-.002 ± .008	0.010 ± .016
6 0	0.016 ± .009	0.020 ± .007	-.003 ± .008	-.014 ± .010	-.014 ± .012	-.025 ± .031
6 1	0.007 ± .006	0.004 ± .005	-.002 ± .006	-.013 ± .009	-.000 ± .009	0.006 ± .018
6 2	-.005 ± .006	0.004 ± .005	0.003 ± .006	-.013 ± .009	0.004 ± .009	-.024 ± .015
6 3	-.001 ± .006	-.005 ± .005	0.002 ± .005	0.005 ± .000	-.012 ± .009	-.036 ± .022
6 4	0.009 ± .006	-.009 ± .005	0.005 ± .005	-.004 ± .007	-.001 ± .008	-.006 ± .022
6 5	0.000 ± .006	0.005 ± .005	-.007 ± .005	-.015 ± .006	-.003 ± .007	-.030 ± .019
6 6	-.002 ± .007	0.003 ± .005	0.002 ± .005	-.004 ± .006	0.000 ± .006	-.029 ± .016

<Re(T(L,M))> in the s channel helicity frame for .05<t<0.08

L M	1.00<m<1.25	1.25<m<1.35	1.35<m<1.45	1.45<m<1.55	1.55<m<1.80	1.80<m<3.00
1 0	-.076 ± .010	-.093 ± .008	-.091 ± .010	-.059 ± .012	0.060 ± .012	0.062 ± .029
1 1	0.060 ± .008	0.031 ± .007	0.048 ± .006	0.052 ± .007	0.084 ± .007	0.074 ± .018
2 0	-.080 ± .010	-.065 ± .008	-.028 ± .009	-.008 ± .010	0.019 ± .012	0.019 ± .025
2 1	0.029 ± .008	0.021 ± .006	0.059 ± .007	0.084 ± .007	0.135 ± .007	0.114 ± .022
2 2	0.041 ± .008	0.032 ± .006	0.040 ± .006	0.053 ± .006	0.088 ± .006	0.058 ± .015
3 0	0.005 ± .010	0.028 ± .008	-.026 ± .009	-.050 ± .011	-.073 ± .011	-.051 ± .025
3 1	-.023 ± .008	-.007 ± .006	0.061 ± .007	-.013 ± .008	0.011 ± .009	0.050 ± .024
3 2	-.016 ± .008	0.006 ± .006	0.010 ± .006	0.031 ± .008	0.023 ± .008	0.054 ± .021
3 3	-.003 ± .008	0.010 ± .006	-.001 ± .006	0.011 ± .006	0.023 ± .006	0.020 ± .015
4 0	0.002 ± .010	-.005 ± .008	-.010 ± .009	-.031 ± .010	-.066 ± .010	-.096 ± .025
4 1	-.008 ± .008	-.018 ± .006	-.019 ± .007	-.036 ± .007	-.024 ± .009	0.006 ± .023
4 2	0.002 ± .008	-.005 ± .006	0.016 ± .006	-.010 ± .008	0.000 ± .009	0.009 ± .022
4 3	-.014 ± .008	0.005 ± .006	0.014 ± .006	0.004 ± .007	0.002 ± .008	0.034 ± .020
4 4	0.007 ± .008	0.003 ± .006	-.002 ± .006	-.002 ± .006	0.002 ± .006	0.004 ± .015
5 0	-.003 ± .010	-.000 ± .008	0.005 ± .009	0.018 ± .010	-.020 ± .011	-.035 ± .024
5 1	0.009 ± .008	0.005 ± .006	-.003 ± .007	-.011 ± .007	-.025 ± .008	-.045 ± .024
5 2	0.000 ± .007	-.008 ± .006	-.008 ± .006	-.012 ± .008	-.017 ± .009	0.010 ± .023
5 3	0.012 ± .008	0.010 ± .006	-.002 ± .006	0.002 ± .008	0.009 ± .009	0.025 ± .023
5 4	-.008 ± .008	-.000 ± .006	0.002 ± .006	-.004 ± .007	0.020 ± .007	0.013 ± .021
5 5	0.018 ± .008	0.008 ± .006	-.003 ± .006	-.007 ± .006	0.009 ± .006	0.010 ± .016
6 0	-.011 ± .011	-.004 ± .008	0.009 ± .009	0.003 ± .010	0.001 ± .012	-.030 ± .025
6 1	0.002 ± .006	0.005 ± .006	-.000 ± .007	-.006 ± .008	-.019 ± .007	-.054 ± .035
6 2	0.008 ± .007	-.003 ± .006	-.005 ± .006	-.011 ± .008	-.024 ± .010	-.005 ± .022
6 3	0.003 ± .008	-.015 ± .006	-.010 ± .006	-.004 ± .008	-.014 ± .009	0.010 ± .022
6 4	-.009 ± .006	0.013 ± .006	-.004 ± .006	-.000 ± .007	-.009 ± .008	-.006 ± .024
6 5	-.010 ± .006	-.001 ± .006	-.004 ± .006	-.004 ± .007	-.003 ± .007	-.008 ± .019
6 6	0.013 ± .006	0.002 ± .006	0.008 ± .006	-.002 ± .006	0.002 ± .006	-.006 ± .014

<Re(T(L,M))> in the s channel helicity frame for .08<t<0.12

L M	1.00<m<1.25	1.25<m<1.35	1.35<m<1.45	1.45<m<1.55	1.55<m<1.80	1.80<m<3.00
1 0	-.037 ± .012	-.050 ± .009	-.070 ± .009	-.014 ± .012	0.021 ± .012	0.075 ± .028
1 1	0.099 ± .010	0.060 ± .008	0.056 ± .007	0.071 ± .008	0.085 ± .007	0.071 ± .018
2 0	-.095 ± .012	-.098 ± .009	-.042 ± .008	-.033 ± .011	-.020 ± .012	0.033 ± .023
2 1	0.031 ± .010	0.046 ± .007	0.080 ± .007	0.127 ± .007	0.125 ± .007	0.166 ± .019
2 2	0.080 ± .010	0.076 ± .007	0.068 ± .006	0.092 ± .006	0.072 ± .006	0.070 ± .014
3 0	-.012 ± .013	0.004 ± .009	-.031 ± .008	-.033 ± .011	-.066 ± .011	-.025 ± .026
3 1	-.039 ± .010	-.044 ± .007	-.010 ± .007	-.026 ± .009	-.025 ± .010	0.083 ± .024
3 2	-.002 ± .010	0.008 ± .007	0.030 ± .007	0.031 ± .008	0.022 ± .007	0.076 ± .019
3 3	0.042 ± .011	0.017 ± .007	0.036 ± .006	0.034 ± .007	0.013 ± .006	0.040 ± .014
4 0	0.019 ± .013	0.006 ± .009	-.043 ± .008	-.043 ± .011	-.042 ± .010	-.099 ± .020
4 1	-.020 ± .010	-.020 ± .007	-.027 ± .007	-.038 ± .009	-.022 ± .011	0.033 ± .022
4 2	-.018 ± .010	-.014 ± .007	0.012 ± .007	0.003 ± .008	-.002 ± .008	0.110 ± .019
4 3	0.022 ± .010	0.020 ± .007	0.014 ± .006	0.014 ± .007	-.007 ± .007	0.003 ± .018
4 4	0.005 ± .011	0.008 ± .007	0.005 ± .006	0.022 ± .007	-.006 ± .006	0.002 ± .013
5 0	-.003 ± .013	-.000 ± .009	0.023 ± .009	0.016 ± .011	-.013 ± .009	-.102 ± .023
5 1	-.003 ± .010	0.001 ± .007	-.020 ± .007	-.009 ± .009	-.015 ± .010	-.038 ± .018
5 2	-.003 ± .009	-.012 ± .007	-.018 ± .007	-.020 ± .008	0.002 ± .009	0.052 ± .026
5 3	0.001 ± .010	-.010 ± .007	0.015 ± .006	0.002 ± .008	-.003 ± .007	0.057 ± .020
5 4	0.022 ± .010	0.002 ± .007	0.012 ± .006	-.006 ± .007	0.006 ± .007	0.022 ± .017
5 5	0.017 ± .011	-.002 ± .007	0.009 ± .006	0.002 ± .007	-.003 ± .006	-.003 ± .013
6 0	0.004 ± .013	-.007 ± .009	0.009 ± .009	0.010 ± .011	-.009 ± .010	-.004 ± .026
6 1	0.004 ± .010	0.020 ± .007	0.001 ± .007	0.002 ± .009	-.016 ± .010	-.058 ± .018
6 2	-.015 ± .010	0.009 ± .007	-.004 ± .006	-.020 ± .008	0.017 ± .009	0.015 ± .018
6 3	-.022 ± .009	-.003 ± .007	-.002 ± .006	-.012 ± .008	-.015 ± .007	0.051 ± .021
6 4	0.010 ± .010	0.001 ± .007	0.006 ± .006	0.009 ± .008	-.022 ± .007	0.029 ± .020
6 5	0.006 ± .010	0.000 ± .007	-.007 ± .006	0.007 ± .007	-.014 ± .008	0.026 ± .017
6 6	0.005 ± .011	0.005 ± .007	-.007 ± .006	0.007 ± .007	-.005 ± .006	0.024 ± .013

<Re(T(L,M))> in the s channel helicity frame for .12<t<0.20

L M	1.00<m<1.25	1.25<m<1.35	1.35<m<1.45	1.45<m<1.55	1.55<m<1.80	1.80<m<3.00
1 0	-.031 ± .013	-.045 ± .010	-.025 ± .010	-.017 ± .010	0.036 ± .010	0.144 ± .019
1 1	0.152 ± .013	0.111 ± .009	0.089 ± .008	0.080 ± .007	0.091 ± .005	0.126 ± .011
2 0	-.145 ± .013	-.142 ± .010	-.102 ± .011	-.072 ± .009	-.040 ± .012	0.050 ± .018
2 1	0.036 ± .013	0.049 ± .009	0.089 ± .007	0.100 ± .007	0.138 ± .005	0.105 ± .015
2 2	0.136 ± .012	0.125 ± .008	0.129 ± .006	0.104 ± .006	0.097 ± .005	0.070 ± .010
3 0	0.002 ± .014	-.001 ± .011	-.021 ± .010	-.041 ± .008	-.037 ± .011	-.085 ± .016
3 1	-.077 ± .014	-.066 ± .009	-.048 ± .008	-.036 ± .009	-.016 ± .009	0.103 ± .015
3 2	-.010 ± .012	0.009 ± .009	0.024 ± .007	0.030 ± .007	0.043 ± .006	0.101 ± .014
3 3	0.057 ± .013	0.050 ± .009	0.051 ± .007	0.050 ± .006	0.039 ± .005	0.035 ± .010
4 0	0.030 ± .015	0.006 ± .011	-.005 ± .009	-.007 ± .009	-.020 ± .010	-.113 ± .016
4 1	-.003 ± .012	-.040 ± .009	-.035 ± .008	-.026 ± .008	-.014 ± .010	0.027 ± .019
4 2	-.020 ± .012	-.032 ± .008	-.010 ± .007	-.009 ± .007	0.015 ± .006	0.110 ± .015
4 3	0.021 ± .012	0.024 ± .009	0.024 ± .007	0.011 ± .007	0.014 ± .005	0.073 ± .014
4 4	0.011 ± .013	0.019 ± .010	0.020 ± .007	0.017 ± .008	-.007 ± .005	0.005 ± .010
5 0	0.014 ± .015	0.002 ± .011	0.025 ± .009	0.015 ± .009	0.014 ± .009	-.111 ± .019
5 1	0.017 ± .012	0.024 ± .009	0.000 ± .008	-.003 ± .008	0.001 ± .010	-.044 ± .016
5 2	-.000 ± .012	-.014 ± .008	-.018 ± .007	-.001 ± .008	0.012 ± .007	0.076 ± .016
5 3	-.024 ± .012	-.008 ± .006	0.000 ± .007	-.000 ± .007	0.023 ± .008	0.050 ± .017
5 4	0.013 ± .012	0.013 ± .009	0.014 ± .007	0.007 ± .007	0.013 ± .005	0.037 ± .014
5 5	0.010 ± .014	-.007 ± .010	0.012 ± .007	-.002 ± .007	-.001 ± .005	0.010 ± .010
6 0	-.012 ± .015	-.004 ± .011	0.013 ± .009	-.009 ± .009	-.001 ± .008	-.040 ± .023
6 1	-.001 ± .012	0.015 ± .006	-.003 ± .007	-.009 ± .007	0.003 ± .010	-.000 ± .013
6 2	-.009 ± .013	0.004 ± .009	-.015 ± .008	0.002 ± .007	0.008 ± .008	0.011 ± .016
6 3	0.001 ± .012	-.016 ± .006	-.007 ± .008	0.004 ± .007	0.007 ± .006	0.030 ± .016
6 4	-.010 ± .012	0.003 ± .006	0.005 ± .007	0.009 ± .007	-.002 ± .008	0.029 ± .016
6 5	-.001 ± .012	0.012 ± .009	0.012 ± .007	-.006 ± .007	-.004 ± .009	0.031 ± .013
6 6	-.009 ± .010	0.006 ± .010	0.004 ± .007	0.000 ± .007	-.003 ± .008	0.004 ± .009

Table VII (f)

<Re(F(L,M))> in the m channel helicity frame for .20<t<0.40

L M	1.08≤m≤1.25	1.25≤m≤1.35	1.35≤m≤1.45	1.45≤m≤1.55	1.55≤m≤1.80	1.80≤m≤3.00
1 0	-.707 ± .014	-.057 ± .014	-.020 ± .014	0.009 ± .013	0.031 ± .009	0.169 ± .014
1 1	0.098 ± .012	0.160 ± .009	0.133 ± .009	0.095 ± .007	0.088 ± .005	0.154 ± .009
2 0	-.111 ± .016	-.150 ± .016	-.134 ± .010	-.114 ± .010	-.104 ± .010	0.006 ± .014
2 1	-.006 ± .012	0.031 ± .010	0.068 ± .009	0.086 ± .007	0.112 ± .005	0.212 ± .011
2 2	0.094 ± .013	0.146 ± .009	0.151 ± .007	0.108 ± .006	0.083 ± .005	0.090 ± .010
3 0	0.050 ± .016	-.012 ± .014	-.009 ± .010	-.008 ± .009	-.040 ± .009	-.111 ± .012
3 1	-.048 ± .012	-.080 ± .012	-.065 ± .009	-.032 ± .008	-.011 ± .007	0.125 ± .014
3 2	-.018 ± .012	0.012 ± .010	0.009 ± .009	0.017 ± .007	0.033 ± .005	0.134 ± .013
3 3	0.049 ± .013	0.067 ± .010	0.064 ± .008	0.038 ± .007	0.030 ± .005	0.051 ± .009
4 0	0.062 ± .016	0.046 ± .013	0.017 ± .010	-.013 ± .009	-.027 ± .009	-.137 ± .013
4 1	-.014 ± .014	-.010 ± .012	-.029 ± .009	-.027 ± .009	-.030 ± .007	0.004 ± .015
4 2	-.038 ± .012	-.033 ± .009	-.028 ± .009	-.018 ± .007	0.012 ± .006	0.119 ± .014
4 3	0.006 ± .012	0.021 ± .010	0.031 ± .008	0.013 ± .007	0.011 ± .005	0.101 ± .012
4 4	0.002 ± .013	0.023 ± .011	0.040 ± .009	0.019 ± .007	-.013 ± .005	0.038 ± .009
5 0	0.016 ± .015	-.093 ± .013	0.013 ± .011	0.005 ± .009	0.000 ± .008	-.101 ± .016
5 1	0.038 ± .012	0.005 ± .012	-.007 ± .009	-.006 ± .008	-.017 ± .007	-.081 ± .013
5 2	0.004 ± .012	-.005 ± .010	-.012 ± .009	-.005 ± .008	-.003 ± .006	0.053 ± .010
5 3	-.013 ± .012	-.010 ± .009	0.006 ± .008	0.006 ± .007	0.020 ± .005	0.096 ± .014
5 4	0.014 ± .012	0.013 ± .010	0.038 ± .009	0.005 ± .007	0.029 ± .005	0.056 ± .012
5 5	0.011 ± .013	0.004 ± .011	0.006 ± .009	0.008 ± .007	0.014 ± .005	0.025 ± .009
6 0	-.021 ± .016	0.015 ± .014	0.002 ± .011	0.002 ± .009	0.007 ± .008	-.015 ± .018
6 1	0.010 ± .011	-.012 ± .011	0.011 ± .009	-.006 ± .008	-.018 ± .007	-.099 ± .012
6 2	0.010 ± .014	0.034 ± .010	-.001 ± .009	-.006 ± .008	-.008 ± .006	-.014 ± .014
6 3	-.014 ± .011	0.004 ± .010	-.010 ± .009	-.007 ± .007	0.002 ± .006	0.039 ± .015
6 4	-.004 ± .012	-.030 ± .010	0.007 ± .008	0.006 ± .007	0.009 ± .005	0.041 ± .015
6 5	-.002 ± .012	0.005 ± .010	0.017 ± .009	0.001 ± .007	0.004 ± .005	0.008 ± .012
6 6	-.014 ± .013	-.001 ± .011	0.002 ± .009	0.002 ± .007	-.001 ± .005	0.002 ± .008

<Re(F(L,M))> in the m channel helicity frame for .40<t<0.60

L M	1.08≤m≤1.25	1.25≤m≤1.35	1.35≤m≤1.45	1.45≤m≤1.55	1.55≤m≤1.80	1.80≤m≤3.00
1 0	-.159 ± .025	-.083 ± .040	-.095 ± .011	-.012 ± .015	0.024 ± .013	0.177 ± .024
1 1	0.046 ± .019	0.099 ± .014	0.083 ± .013	0.086 ± .013	0.086 ± .010	0.198 ± .020
2 0	-.055 ± .028	-.016 ± .036	-.067 ± .018	-.122 ± .015	-.104 ± .015	-.035 ± .032
2 1	-.024 ± .020	0.907 ± .030	0.026 ± .014	0.039 ± .012	0.062 ± .010	0.241 ± .026
2 2	-.001 ± .019	0.031 ± .013	0.057 ± .013	0.058 ± .013	0.081 ± .009	0.139 ± .015
3 0	0.082 ± .027	0.052 ± .020	0.021 ± .018	-.006 ± .015	-.021 ± .015	-.145 ± .029
3 1	-.068 ± .022	0.028 ± .035	-.057 ± .014	-.045 ± .012	-.001 ± .010	0.118 ± .032
3 2	0.006 ± .020	-.006 ± .021	-.018 ± .013	0.017 ± .012	0.034 ± .010	0.116 ± .019
3 3	0.031 ± .019	0.011 ± .012	0.015 ± .014	0.039 ± .013	0.040 ± .009	0.070 ± .015
4 0	-.059 ± .027	-.014 ± .018	0.084 ± .018	-.002 ± .015	-.012 ± .014	-.159 ± .021
4 1	0.034 ± .020	0.020 ± .033	0.016 ± .014	0.010 ± .012	-.027 ± .011	-.025 ± .034
4 2	-.050 ± .020	0.023 ± .026	-.004 ± .013	-.014 ± .012	-.004 ± .009	0.121 ± .021
4 3	-.009 ± .020	-.003 ± .014	0.003 ± .013	0.004 ± .012	0.029 ± .010	0.149 ± .020
4 4	0.017 ± .019	0.013 ± .012	0.021 ± .014	0.026 ± .013	-.001 ± .009	0.051 ± .015
5 0	0.018 ± .028	-.028 ± .028	-.011 ± .018	0.012 ± .015	0.008 ± .013	-.088 ± .026
5 1	-.003 ± .019	0.036 ± .022	0.008 ± .014	0.013 ± .012	-.031 ± .011	-.090 ± .029
5 2	-.007 ± .020	0.036 ± .030	0.022 ± .013	-.002 ± .012	-.013 ± .009	0.010 ± .030
5 3	-.017 ± .020	0.009 ± .016	0.006 ± .013	0.009 ± .012	0.012 ± .009	0.121 ± .021
5 4	0.028 ± .020	-.029 ± .013	0.002 ± .013	0.004 ± .012	0.031 ± .009	0.087 ± .021
5 5	0.006 ± .019	0.005 ± .012	-.002 ± .015	0.018 ± .014	0.036 ± .010	0.023 ± .015
6 0	0.044 ± .028	-.039 ± .035	-.007 ± .018	-.025 ± .016	0.029 ± .012	0.059 ± .026
6 1	-.013 ± .020	-.007 ± .013	0.006 ± .014	-.019 ± .011	-.003 ± .011	-.059 ± .022
6 2	-.008 ± .020	-.006 ± .032	-.016 ± .013	-.001 ± .012	-.020 ± .009	-.055 ± .034
6 3	-.023 ± .021	0.023 ± .019	0.000 ± .013	0.008 ± .012	0.001 ± .009	0.036 ± .024
6 4	-.043 ± .020	-.002 ± .013	-.009 ± .013	0.008 ± .012	-.001 ± .009	0.019 ± .023
6 5	-.009 ± .020	-.026 ± .012	0.002 ± .014	0.002 ± .013	-.023 ± .010	0.034 ± .022
6 6	0.022 ± .019	-.010 ± .012	0.001 ± .014	0.011 ± .014	-.013 ± .010	-.001 ± .016

<Re(F(L,M))> in the m channel helicity frame for .60<t<1.00

L M	1.08≤m≤1.25	1.25≤m≤1.35	1.35≤m≤1.45	1.45≤m≤1.55	1.55≤m≤1.80	1.80≤m≤3.00
1 0	-.060 ± .034	-.188 ± .034	-.124 ± .034	-.091 ± .027	-.012 ± .032	0.127 ± .031
1 1	0.032 ± .026	0.051 ± .019	0.087 ± .024	0.047 ± .020	0.124 ± .018	0.180 ± .034
2 0	-.138 ± .038	0.067 ± .032	-.095 ± .037	-.073 ± .024	-.110 ± .034	-.087 ± .029
2 1	-.011 ± .028	-.051 ± .026	-.016 ± .026	-.005 ± .023	0.051 ± .021	0.202 ± .032
2 2	-.076 ± .031	0.001 ± .019	0.015 ± .025	-.015 ± .022	0.036 ± .016	0.153 ± .025
3 0	0.089 ± .035	0.017 ± .030	0.067 ± .033	0.039 ± .027	-.038 ± .026	-.177 ± .025
3 1	-.045 ± .028	0.023 ± .026	-.007 ± .027	-.014 ± .020	-.004 ± .025	-.013 ± .028
3 2	0.057 ± .328	-.003 ± .020	-.000 ± .024	-.023 ± .023	0.068 ± .018	0.117 ± .035
3 3	-.034 ± .030	0.014 ± .018	0.030 ± .025	-.031 ± .022	0.057 ± .017	0.096 ± .025
4 0	0.030 ± .039	-.016 ± .029	-.030 ± .032	-.035 ± .026	-.025 ± .021	-.127 ± .030
4 1	-.022 ± .026	-.056 ± .029	0.001 ± .026	0.016 ± .019	-.066 ± .027	-.131 ± .026
4 2	0.001 ± .030	0.023 ± .020	0.001 ± .025	-.011 ± .021	-.025 ± .019	0.022 ± .031
4 3	-.001 ± .029	0.057 ± .019	-.004 ± .022	0.003 ± .023	0.024 ± .018	0.097 ± .039
4 4	0.025 ± .031	0.016 ± .018	-.002 ± .025	0.016 ± .020	-.023 ± .017	0.064 ± .026
5 0	0.310 ± .035	0.067 ± .032	-.013 ± .032	-.031 ± .028	0.009 ± .025	0.065 ± .032
5 1	0.355 ± .026	0.006 ± .025	0.000 ± .025	-.004 ± .019	-.083 ± .023	-.116 ± .020
5 2	-.020 ± .028	-.045 ± .023	0.012 ± .026	-.015 ± .020	-.013 ± .021	-.100 ± .023
5 3	0.005 ± .030	-.021 ± .020	-.013 ± .024	-.010 ± .023	0.010 ± .019	0.038 ± .030
5 4	-.029 ± .030	-.011 ± .019	0.020 ± .024	0.000 ± .021	0.015 ± .018	0.086 ± .031
5 5	0.041 ± .031	0.010 ± .018	-.034 ± .026	0.006 ± .019	0.026 ± .016	0.047 ± .027
6 0	0.065 ± .037	0.020 ± .333	0.019 ± .032	0.023 ± .025	0.036 ± .029	0.102 ± .025
6 1	0.014 ± .027	0.006 ± .023	-.004 ± .025	-.013 ± .022	-.024 ± .021	0.008 ± .029
6 2	0.015 ± .029	-.024 ± .023	0.005 ± .024	-.003 ± .017	-.021 ± .022	-.001 ± .029
6 3	-.029 ± .027	-.016 ± .020	-.016 ± .026	-.031 ± .023	-.005 ± .020	-.039 ± .027
6 4	-.057 ± .031	0.005 ± .020	-.015 ± .023	0.015 ± .020	-.021 ± .018	0.076 ± .031
6 5	0.011 ± .029	-.017 ± .020	0.026 ± .025	0.021 ± .021	0.005 ± .018	0.052 ± .031
6 6	0.005 ± .031	0.026 ± .017	-.021 ± .025	0.044 ± .021	-.005 ± .017	0.003 ± .026

Consequently, we would expect a large negative value for $\langle Y_{10} \rangle$, this is, in fact, observed in the data.

CHAPTER V

DISCUSSION AND CONCLUSIONS

In this chapter we explore our results in the light of those available from other diffraction dissociation experiments and present a comparison between our data and a theoretical calculation using a Deck-type model.

A. Comparison With Other Experiments

1. Other Results for the Reaction $n+p \rightarrow p\pi^- + p$

Data available from other investigations of the reaction $n+p \rightarrow p\pi^- + p$ are summarized in Table VIII. All but one of the listed experiments were performed in bubble chambers, the exception being the recent spark-chamber spectrometer work from Serpukhov[15]. Also, with the exception of the Serpukhov results, all the data are for neutron momenta below 30 GeV/c.

In most of the lower-energy experiments, deuterium was used as a source of neutrons necessitating a nuclear physics correction. There is also an important physics distinction which must be considered when comparing our experiment with the lower-energy data. As discussed in the introduction, at high energy we expect Reaction (1) to proceed primarily via the exchange of a Pomeronchukon (or alternatively the exchange of the quantum numbers of the vacuum)

Table VIII

Summary of previous measurements of $p+n \rightarrow p+(\pi^- p)$ for incident momenta in excess of 5 GeV/c.

(GeV/c) Momentum	Reference	Experimental Method	Number of Events	Total Cross Section (μb)
7	9	deuterium filled bubble chamber	1000	900 ± 40[16]
11.6	10	"	1000	680 ± 70[16]
12.7±3.5	11	neutron beam hydrogen bubble chamber	1300	459 ± 12
19.9±4	11	"	1800	391 ± 9
19	12	deuterium filled bubble chamber	600	580 ± 30
28	13	"	1000	590 ± 60[16]
12.5[16]	14	deuteron beam hydrogen B.C.	2000	660 ± 50[16]
40±5	15	neutron beam and spectrometer		385 ± 190
50±5	"		↑ 15000	290 ± 120
60±5	"		↓	285 ± 80

between the target proton and the incident neutron. At lower energy there is, of course, no reason why this should be the dominant production mechanism[18].

In general, there are three exchange amplitudes involved in any nucleon dissociation reaction. These can be described in terms of the isospin exchanged in the t-channel (I_t) and the resulting isospin of the dissociated nucleon (I). If we write the amplitude for a given value of I_t and I as $M_I^{I_t}$, then the cross section for a process such as Reaction (1) can be written as:

$$\sigma(pn \rightarrow p(\pi^- p)) = \frac{2}{3} \int \left| M^0_{1/2} + \frac{1}{3} M^1_{1/2} - \frac{1}{3} M^1_{3/2} \right|^2 dR$$

where the integration is over phase space. The I_t=0 amplitude is dominated at high energy by $\mathbb{P}$ exchange. The other amplitudes involve meson exchanges.

The momentum dependence of each of the three isospin amplitudes can be determined by using isospin relationships and comparing our reaction with other single-pion production reactions (e.g., $pn \rightarrow p(n\pi^0)$). Such analyses have been performed on low energy data[12] and have determined the exchange mechanisms involved. The results show that while Pomeronchukon-induced dissociation is clearly predominant at high energy, there is increasing competition from the other amplitudes as the energy is reduced. The contribution from non-diffractive processes ranges from ∿20% at a momentum of 30 GeV/c to more than 50% when the momentum is ∿5 GeV/c.

Despite the differences expected between our data and those obtained at lower energies, our data are remarkably similar to previous measurements. In particular, the general shape of the mass and $\cos\theta_{GJ}$ distributions, as well as the strong variation of $d\sigma/dt$ with mass, appear to be essentially energy independent. One possible disagreement between our results and previous measurements is an excess in the Serpukhov data of events in $d\sigma/d\cos\theta_{GJ}$ at large negative values of $\cos\theta_{GJ}$. We know of nothing in our data that would cause special difficulty in this region.

Figure 43 displays the integrated cross section for Reaction (1) as a function of momentum for both our data and that at lower energy. There is a marked reduction in the momentum dependence above 50 GeV/c. As we will see in the next section, this very weak momentum dependence is confirmed by recent data from a similar reaction measured at the Intersecting Storage Rings (ISR) at CERN.[8]

2. Results from Other Dissociation Reactions

(a) Final States Containing Two Nucleons and One Pion

As was mentioned in the previous section, single-pion production in nucleon-nucleon reactions ($pN \rightarrow NN\pi$, where N represents either a neutron or a proton) has been analyzed in terms of isospin exchange amplitudes. Of the three possible amplitudes, only the $\mathbb{P}$-part of the $I_t=0$ exchange is important at high energy. A number of experiments have been performed to study other $pN \rightarrow NN\pi$ reactions.[12] Most of the data are, however, from low energies, where the competing amplitudes are important making it difficult to

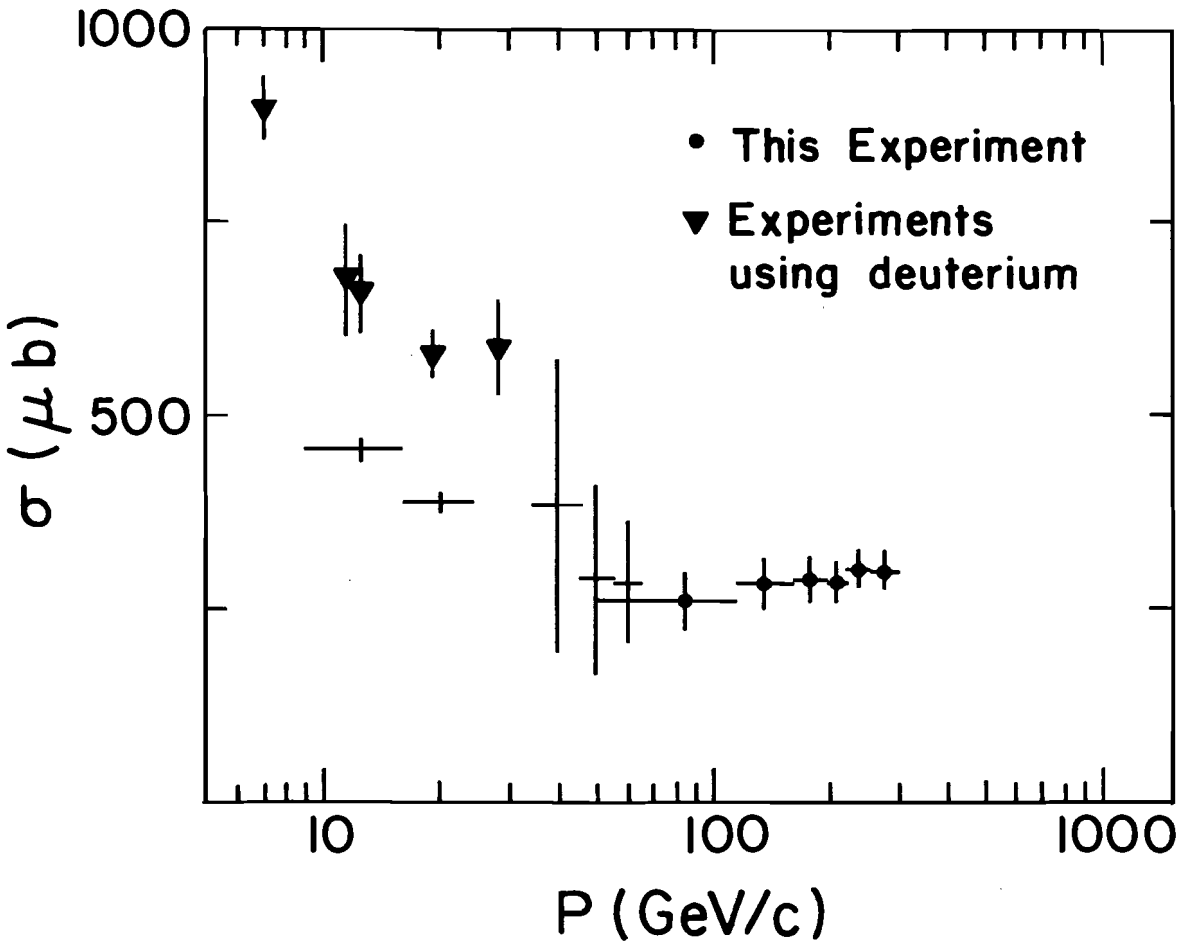
1000
500
σ (μb)
10
100
1000
P (GeV/c)
• This Experiment
▼ Experiments using deuterium

Figure 43

extract the $\mathbb{P}$ contribution.

A recent ultra high energy experiment performed at the CERN ISR[8] has reported data for the reaction $p+p \rightarrow (n\pi^+)+p$ at an equivalent laboratory momentum of over 1000 GeV/c. This reaction is charge symmetric to Reaction (1). The contribution from $I_t=0$ exchange for this experiment should be comparable to that in our reaction, so a direct comparison is appropriate.

Agreement between our results and those from the ISR is excellent. It is especially interesting that the ISR group reported the previously mentioned peak at a mass of 2.2 GeV/c^2. The two sets of data are completely consistent with each other on this point.

Figure 44 shows the cross section for single-pion production as a function of momentum for both our reaction and the $pp \rightarrow n\pi^+p$ reaction. (The pp data are for the break up of only a single proton. Namely, the total cross section for the reaction is a factor of two larger than indicated on the graph.) This plot confirms the expected convergence of the two cross sections with increasing momentum. The greatly extended momentum range provided by the addition of the ISR data gives further indication of the almost constant cross section for dissociation at momenta above 50 GeV/c.

(b) Final States Involving One Nucleon and Two Pions

Nucleon dissociation can also occur in interactions of a nucleon with a meson. As in the two-nucleon case, most of the data are from low energy bubble chamber experiments[19]. Again, we can

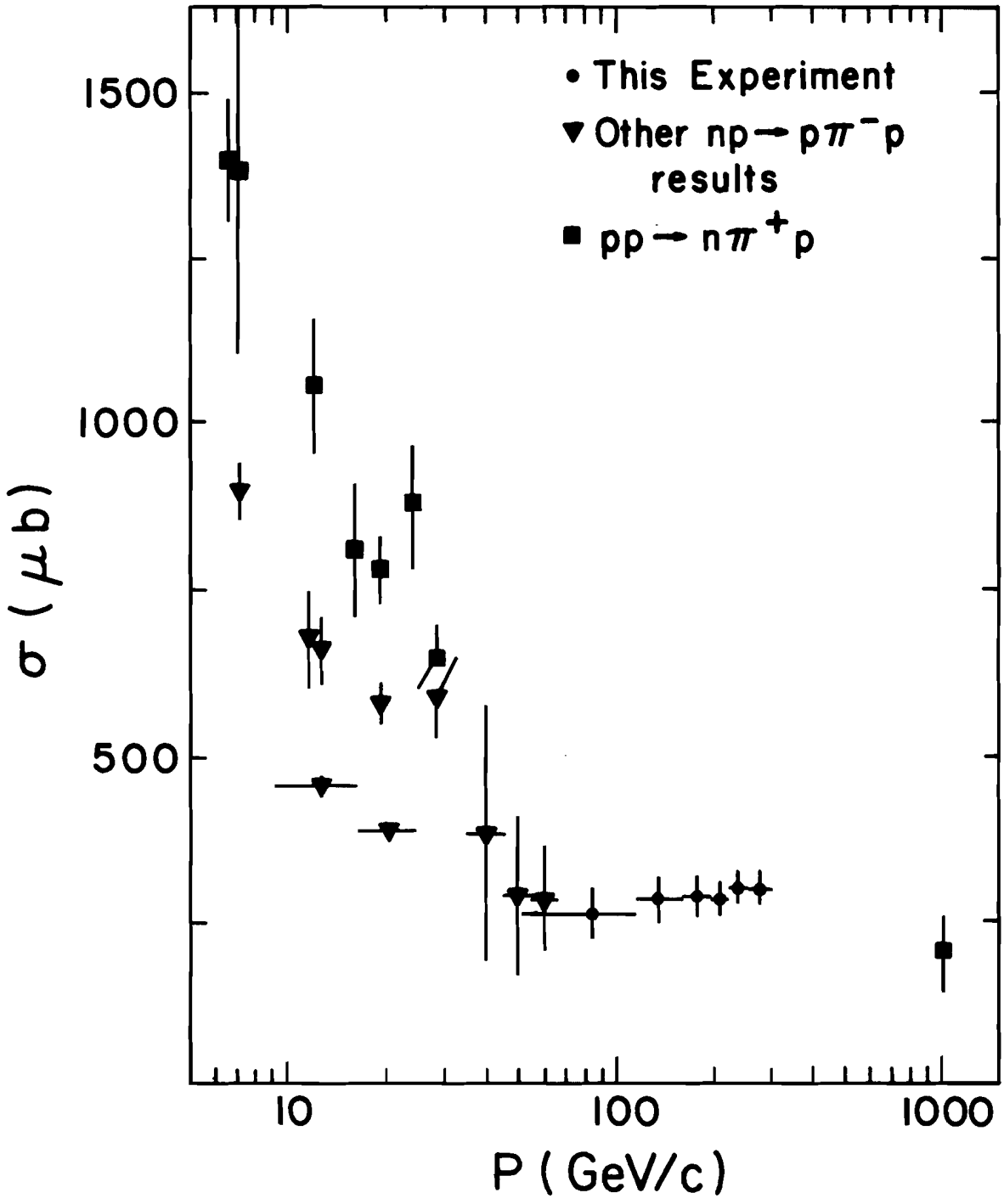
• This Experiment
▼ Other np → pπ⁻p results
■ pp → nπ⁺p
1500
1000
500
σ (μb)
10
100
1000
P (GeV/c)

Figure 44

discern the basic features of the dissociation process but detailed comparisons with our results are hampered by the low statistics and additional isospin exchange contributions involved.

A relatively large sample of events has become available recently from a dissociation experiment at SLAC[20]. Data were obtained using a hybrid bubble chamber system which served to limit the bubble chamber pictures taken to those likely to contain the desired interaction. The reactions studied were

$$\pi^{\pm}p \rightarrow \pi^{\pm}(p\pi^{o})$$

$$\pi^{\pm}p \rightarrow \pi^{\pm}(n\pi^{+})$$

$$\pi^{\pm}p \rightarrow \pi^{\pm}(\Delta^{++}\pi^{-})$$

The incident pion momentum was 14 GeV/c. The first two reactions represent dissociation of the target proton into a pion-nucleon pair, and these data exhibit behavior very similar to that of our results. Of particular interest in this regard are the results presented on the correlation between $d\sigma/dt$ and mass. When the t distribution is parameterized as e^{-bt}, the SLAC data at small t yield a dependence of b upon mass that decreases at first, becomes nearly constant for masses between approximately 1.2 and 1.4 GeV/c^2, and continues to decrease at still higher masses. This is essentially what we observe in our data (Fig. 24).

B. Comparison With a Model

We complete our discussion of the data by presenting a comparison between our results and the predictions of a theoretical model. Our calculation was a slightly simplified version of that used recently by Babaev et al.[21] In this model, the total dissociation amplitude was written as the sum of the amplitudes for the three processes shown in Fig. 45.

The first diagram represents the production via pion exchange followed by pion-proton elastic scattering at the lower vertex. This is the mechanism originally proposed by Deck[22] to provide a nonresonant explanation for the low-mass peak observed in the reaction $\pi+p \rightarrow (\pi\rho) + p$. In our case, two more diagrams have been included in the model.[23] The second diagram in Fig. 45 introduces a proton exchange contribution while the final diagram adds a term for direct nonresonant dissociation (a neutron-pole term).

There is some evidence in the data for resonant production hence we should not expect a nonresonant model to exactly reproduce the data. The concept of extended duality[24] gives us, however, reason to believe that a suitable nonresonant model should provide a good description of the data, at least on the average. Our calculation is very simple, it leaves out, for example, any consideration of absorptive effects, and we therefore present this model only as a first attempt to describe the data.

Comparisons between our data and the model are presented in Figs. 46 through 49. Figure 47 best illustrates the strengths and

(a) pion exchange Deck

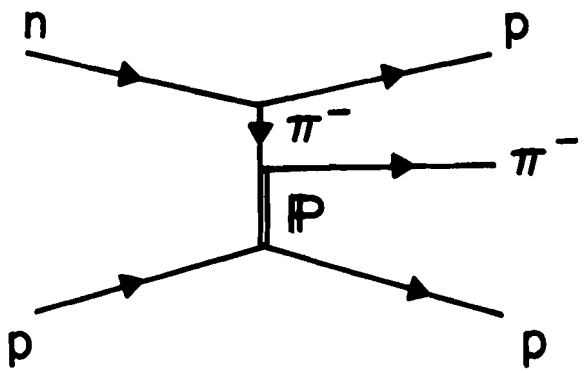

(b) proton exchange Deck

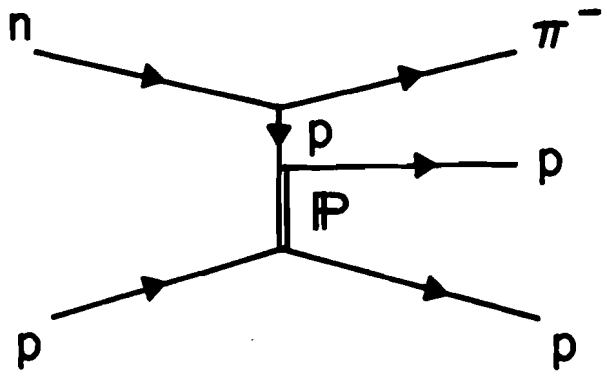

(c) direct production

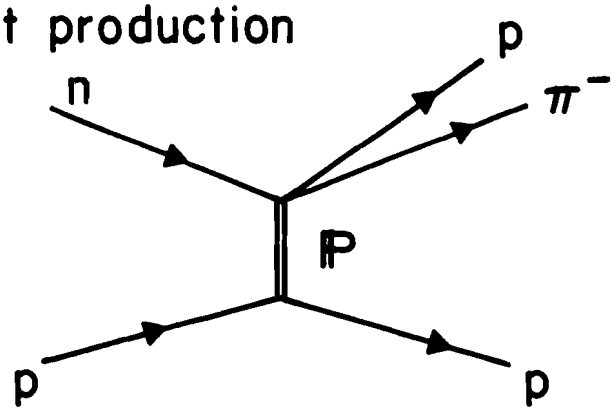

Figure 45

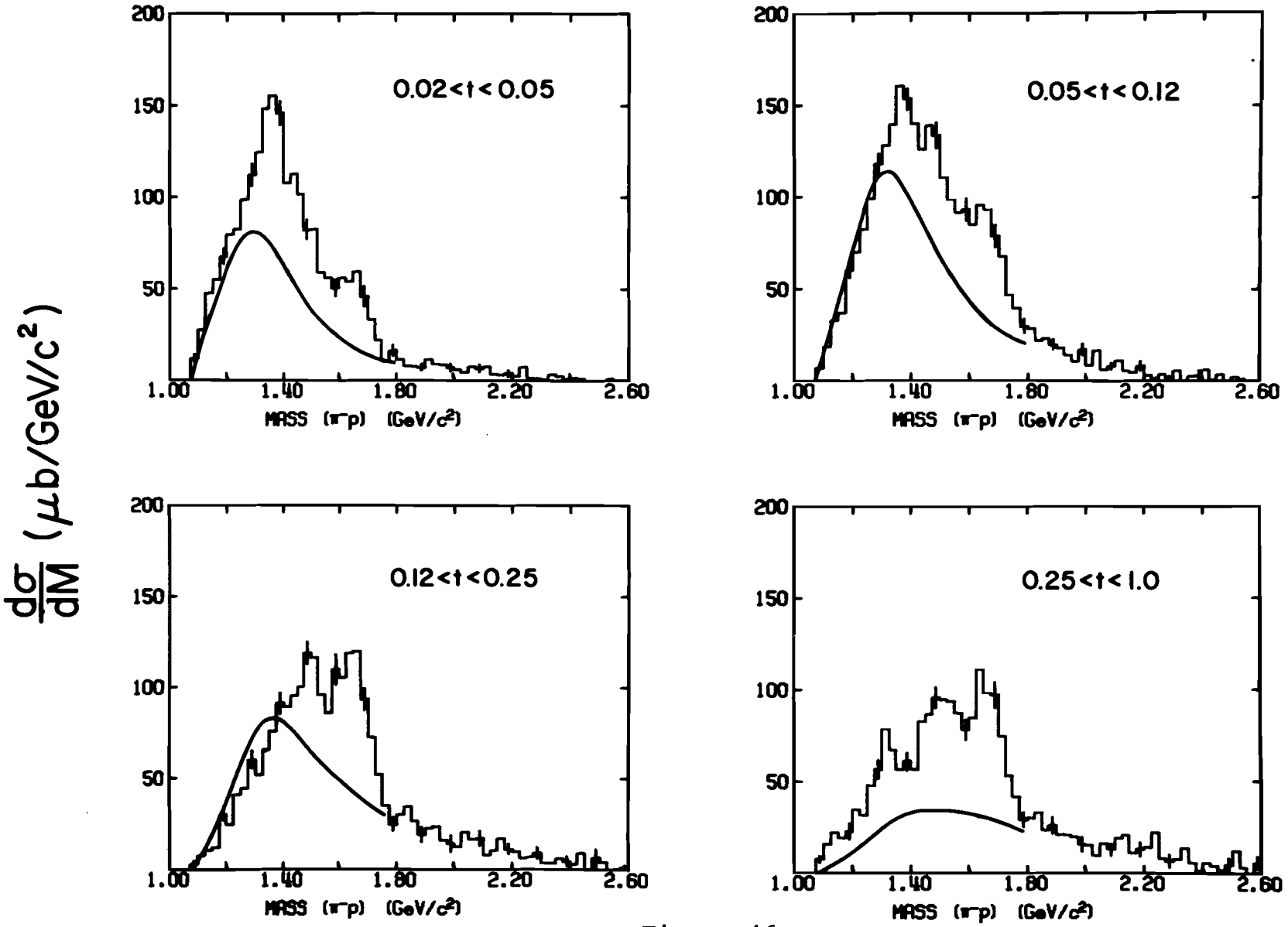
$\frac{d\sigma}{dM}$ (μb/GeV/c^2)
0.02<t<0.05
0.05<t<0.12
0.12<t<0.25
0.25<t<1.0
200
150
100
50
1
1.00
1.40
1.80
2.20
2.60
MASS (π^-p) (GeV/c^2)

Figure 46

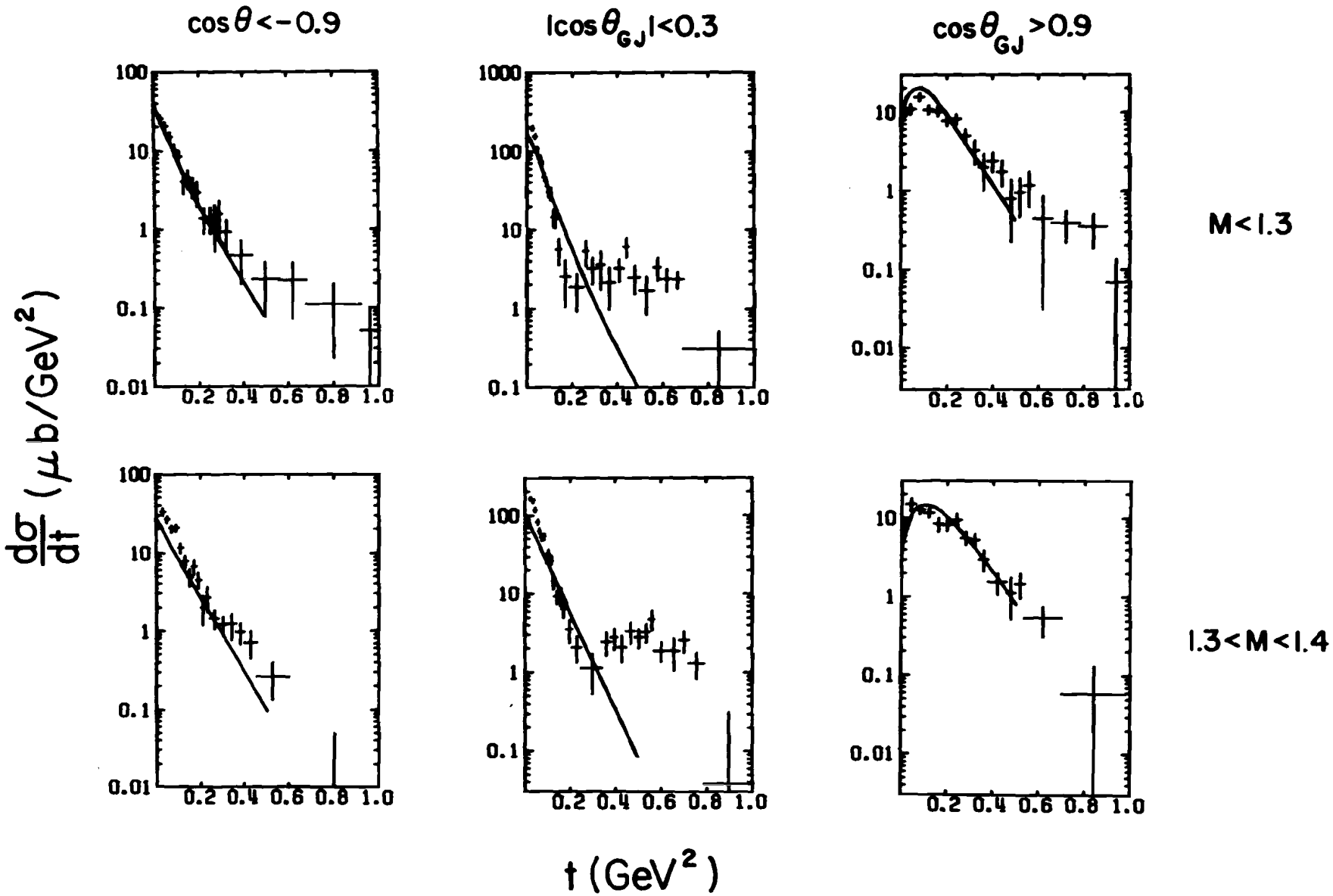

Figure 47 (a)

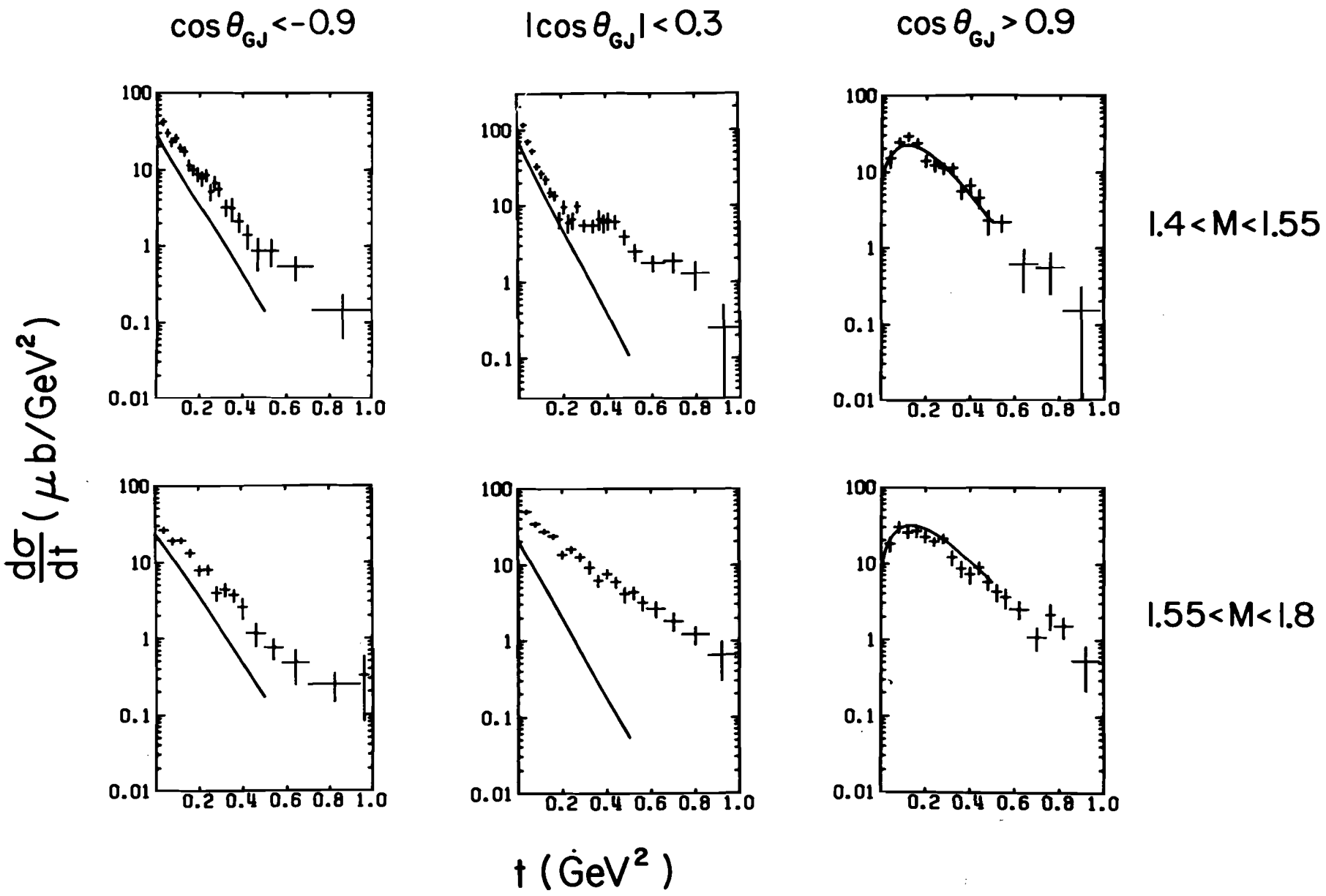
cos θGJ<-0.9
|cos θGJ|<0.3
cos θGJ>0.9
1.4<M<1.55
1.55<M<1.8
dσ/dt (μb/GeV²)
t (GeV²)
100
10
1
0.1
0.01
0.2 0.4 0.6 0.8 1.0

Figure 47 (b)

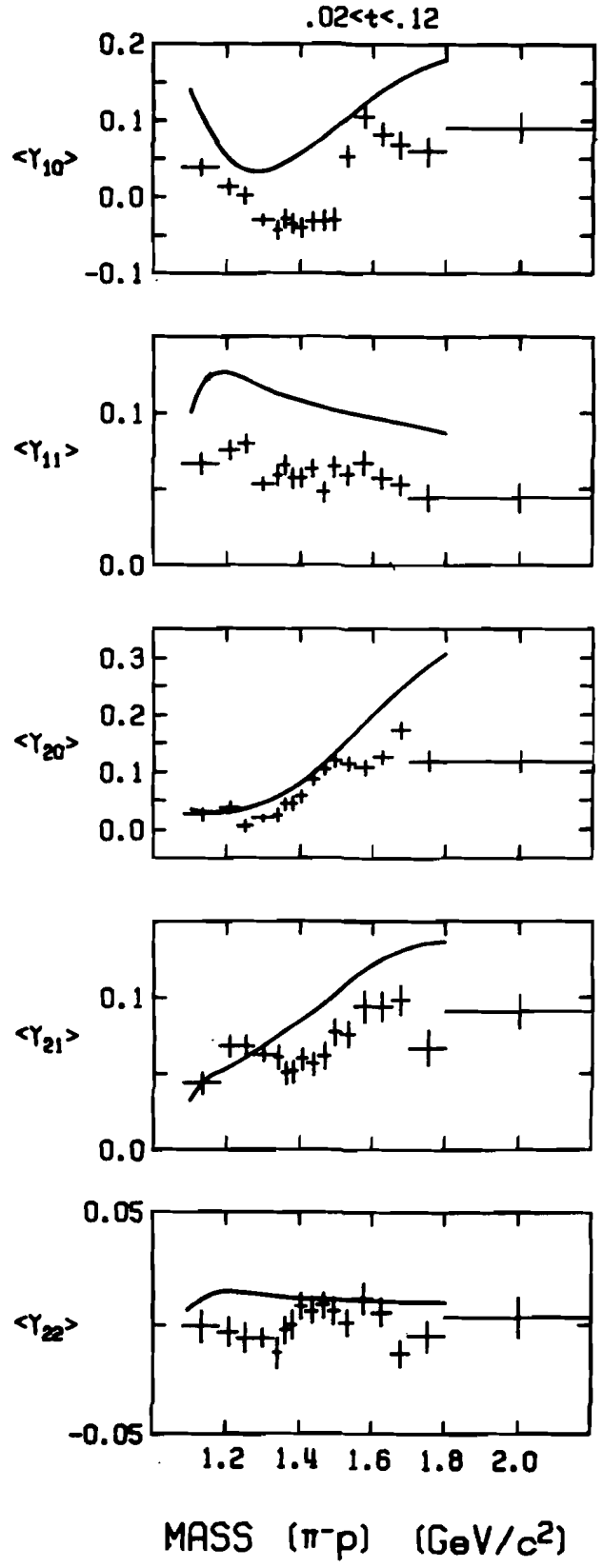
.02<t<.12
0.2
0.1
0.0
-0.1
<Y10>
0.1
0.0
<Y11>
0.3
0.2
0.1
0.0
<Y20>
0.1
0.0
<Y21>
0.05
-0.05
<Y22>
1.2
1.4
1.6
1.8
2.0
MASS (π⁻p) (GeV/c²)

Figure 48

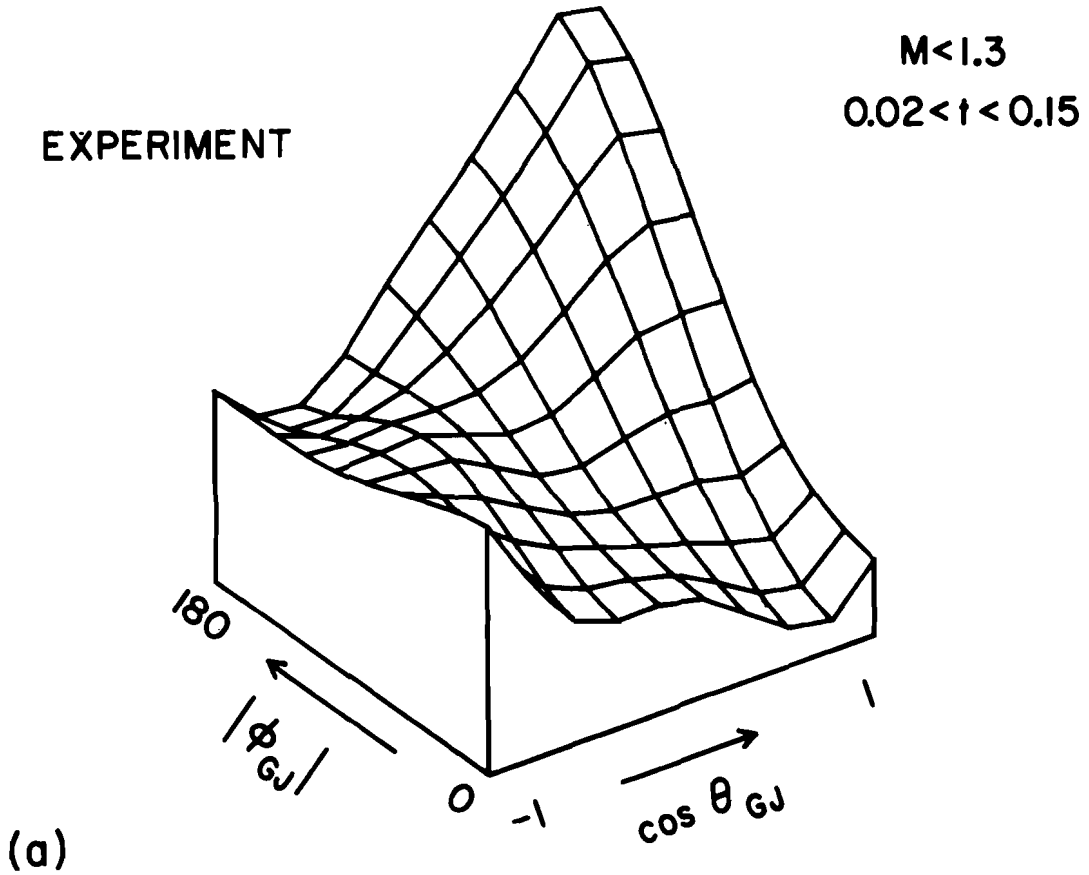
EXPERIMENT
M<1.3
0.02<t<0.15
180
$|\phi_{GJ}|$
0
-1
1
$\cos\theta_{GJ}$

(a)

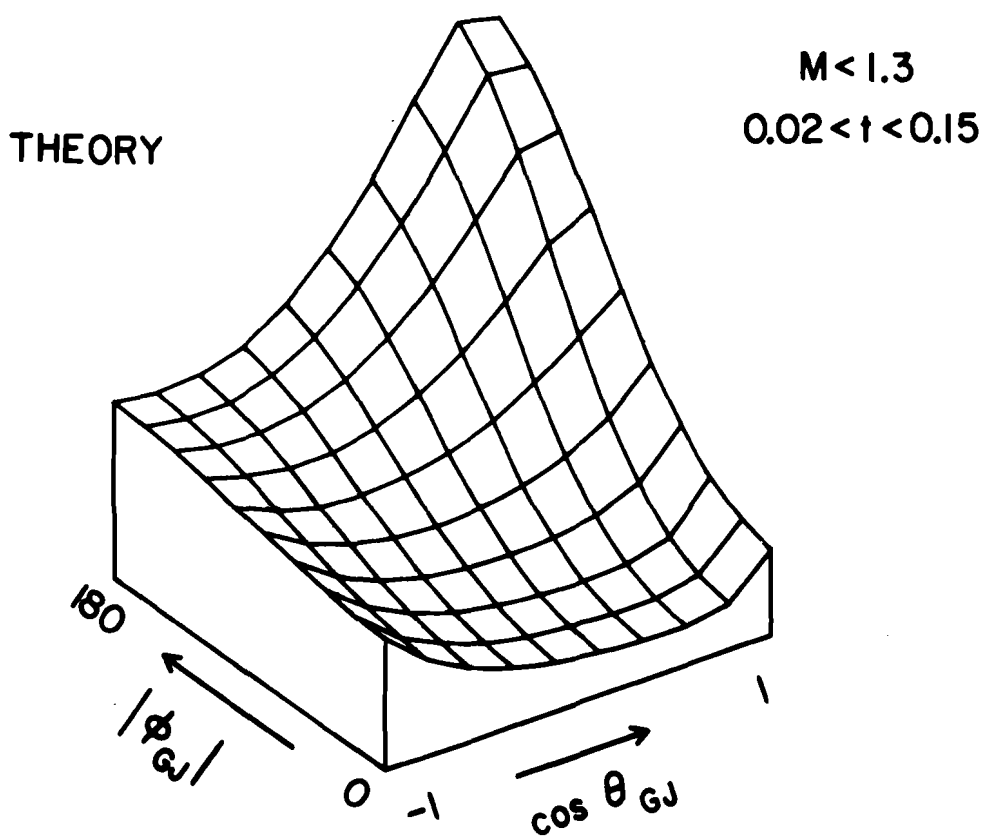
THEORY
M<1.3
0.02<t<0.15
180
$|\phi_{GJ}|$
0
-1
1
$\cos\theta_{GJ}$

(b)

Figure 49

weaknesses of the calculation. From these plots we can see that agreement between theory and experiment is excellent at large values of $\cos\theta_{GJ}$ for all masses. The contribution to the cross section in this range of angles is primarily from the pion-exchange diagram. Data for small values of $\cos\theta_{GJ}$ agree well at low mass but the theoretical cross section is too low when higher masses are selected. Central values of $\cos\theta_{GJ}$ are predicted least accurately and, although agreement seems to be better at low mass, the calculation completely fails to predict the experimentally observed break in the t distribution. Overall, the model is most accurate in the region of small mass and small t. This can also be seen by examining the $d\sigma/dM$ distributions shown in Fig. 46.

The decay-angle distributions[25] in the Gottfried-Jackson frame for events with low mass and small t are compared with the model in Fig. 49. As could be expected from the experience with t distributions, agreement is best at large values of $\cos\theta_{GJ}$. The predicted dependence on ϕ_{GJ} for $\cos\theta_{GJ} < 0$, however, is not correct. It should be pointed out that the rise of the cross section in the backward direction of $\cos\theta_{GJ}$ is evidence for the need of some process in addition to the originally proposed pion-exchange model. The pion exchange contribution falls too rapidly as $\cos\theta_{GJ}$ becomes negative to account for the observed behavior.

A more stringent test of the model is available in the predicted moments of the angular distributions. The results given in Fig. 48, qualitatively, display similar behavior for model and data,

for the ℓ=1 moments; a more quantitative agreement appears to hold for those with ℓ=2. In summary, the model has the ability to explain certain aspects of the data quite well but more detailed calculations are needed to attain a complete understanding of the dissociation process.

C. Conclusions

There is at present no fundamental understanding of the dissociation process. Nevertheless, we can draw a number of important conclusions from our work. The dissociation cross section which had been falling steadily with increasing momentum at momenta below 50 GeV/c has no significant momentum dependence over our range of incident momenta. In addition to our confirming the strong mass-t correlation characterizing our reaction, we have found a surprising dependence of the t distribution on the polar angle in the Gottfried-Jackson frame. A complicated mass spectrum, containing apparently both resonant states and a continuum component was observed and some evidence was found for a high mass state at 2.2 GeV/c^2. Moments of the decay-angle distributions have revealed a rich structure, suggesting contributions from many partial waves. Finally, a measure of success was achieved in explaining the data in terms of a Deck-like model. Although a model capable of explaining the details has yet to be worked out, it appears that we are beginning to understand the process of inelastic diffraction and the nature of the neutron.[26]

FOOTNOTES AND REFERENCES

1. An extensive literature exists on the subject of diffractive processes. Two important early references are:

   a) E. L. Feinberg and I.Pomeranchuk, Suppl. Nuovo Cimento 3 (1956) 652; and

   b) M. L. Good and W. D. Walker, Phys. Rev. 120 (1960) 1857.

   A number of useful review articles are listed below:

   c) D. W. G. S. Leith, Diffractive Processes, Lecture notes for the 1974 SLAC Summer Institute in Particle Physics, SLAC Report No. 179, Volume 1, p.3;

   d) S. V. Mukhin and V. A. Tsarev, AIP Conference Proceedings No. 23, Particles and Fields Subseries No. 10 (1974) 263;

   e) H. J. Lubatti, Acta Phys. Pol. B3 (1972) 721.

2. One could, for example, consider the case in which A is an incident deuteron and A* a dissociated p-n pair. This was, in fact, one of the earliest examples to which this line of reasoning was applied (see reference 1a).

3. W. S. C. Williams, An Introduction to Elementary Particles, second edition p.406. Academic Press, New York and London (1971).

4. D. R. O. Morrison, Phys. Letters 22 (1966) 528.

5. In the past, dissociation has often been described using the variable $t' \equiv t-t_{min}$ where t_{min} is the minimum four momentum transfer required to produce a final state with a given $\pi^- p$ rest mass. As indicated in the text, for the range of masses

and momenta covered in this work, t=t' to an excellent degree of approximation.

6. In determining the momentum dependence of the cross section, we used the incident neutron momentum spectrum measured in our previous study of dissociation on nuclear targets. See Appendix for further discussion.

7. A. C. Melissinos and S. L. Olsen, Phys. Rep. C17 (1975) 77.

8. H. de Kerret et.al., Phys. Letters 63B (1976) 477; H. de Kerret et.al., Phys. Letters 63B (1976) 483.

9. G. Yekutieli et.al., Nucl. Phys. B38 (1972) 605.

10. D. Hochman et.al., Nucl. Phys. B80 (1974) 45.

11. R. E. Ansorge et.al., Cavendish Laboratory Preprint (1975).

12. E. Dahl-Jensen et.al., Nucl. Phys. B87 (1975) 426.

13. W. Burdett et.al., Nucl. Phys. B48 (1972) 13.

14. J. W. Cooper et.al., Nucl. Phys. B79 (1974) 259.

15. A. Babaev et.al., CERN Preprint (June 1976) submitted to Nuclear Physics.

16. These cross sections were not taken directly from the cited references but have been obtained from the modified values given in reference 11.

17. Deuterium beam at 25 GeV/c.

18. For example, Δ production via π^o or ρ^o exchange is an important process.

19. One recent example is the work reported by R. Harris et.al., University of Washington preprint VTL-PUB-32 (May 1976).

20. V. Chaloupka, Study of Proton Difrraction in $\pi^{\pm}p$ Collisions at 14 GeV/c (Paper submitted to the Topical Conference on Baryon Resonances, Oxford 1976).

21. The original calculation is described in reference 15. We have made two simplifications in the calculation: the exchanged pion in Fig. 45 was considered to be an elementary pion rather than a Regge trajectory, and the spin flip component of πp elastic scattering in this same diagram was set equal to zero. Also, as was done by Babaev et.al., we have renormalized the absolute theoretical cross section to improve agreement with the data. The actual calculated cross sections are approximately a factor of two larger than those presented in the following discussion.

22. R. T. Deck, Phys. Rev. Letters 13 (1964) 169.

23. While the dissociation reaction $\pi p \rightarrow (\pi\rho)p \rightarrow (\pi\pi\pi)p$ has been successfully described using only a pion exchange model (G. Ascoli et.al., Phys. Rev. D9 (1974) 1963), calculations performed for nucleon dissociation reactions have been unsuccessful in describing the data without the addition of other processes. See, for example, E. L. Berger, A Critique of the Reggeized Deck Model, Argonne report ANL/HEP 7506 (1975).

24. G. F. Chew and A. Pignotti, Phys. Rev. Letts. 20 (1968) 1078.

25. The data presented here have been smoothed to reduce the effects of statistical fluctuations.

26. Much of the work which appears in this thesis has been

published in the literature. The latest papers include: J. Biel et.al., Phys. Rev. Lett. 36 (1976) 504; J. Biel et.al., Phys. Rev. Lett. 36 (1976) 507; J. Biel et.al., Phys. Lett. 65B (1976) 291.

27. G. Fäldt, Nucl. Phys. B43 (1972) 591.

APPENDIX

INCIDENT NEUTRON MOMENTUM SPECTRUM

The incident neutron momentum spectrum was obtained from our study of the reaction $n+Pb \rightarrow \pi^- p+Pb$ using essentially the same spectrometer described in Chapter II. For neutrons with momenta above 50 GeV/c this process occurs primarily through Coulomb dissociation (i.e., the exchange of a virtual photon) and has a small-t behavior determined essentially by the resolution of the apparatus. We used this strong t-dependence to extract a nearly pure Coulomb dissociation component of the data by selecting only those events with $t < .001$ GeV^2. The data were then corrected for geometric efficiency of the spectrometer and for losses of events at $t < .001$ GeV^2 due to resolution. The momentum dependence of Coulomb dissociation was next calculated from theory[27] and this momentum dependence was divided out of the data. The resulting momentum spectrum is shown in Fig. A-1.

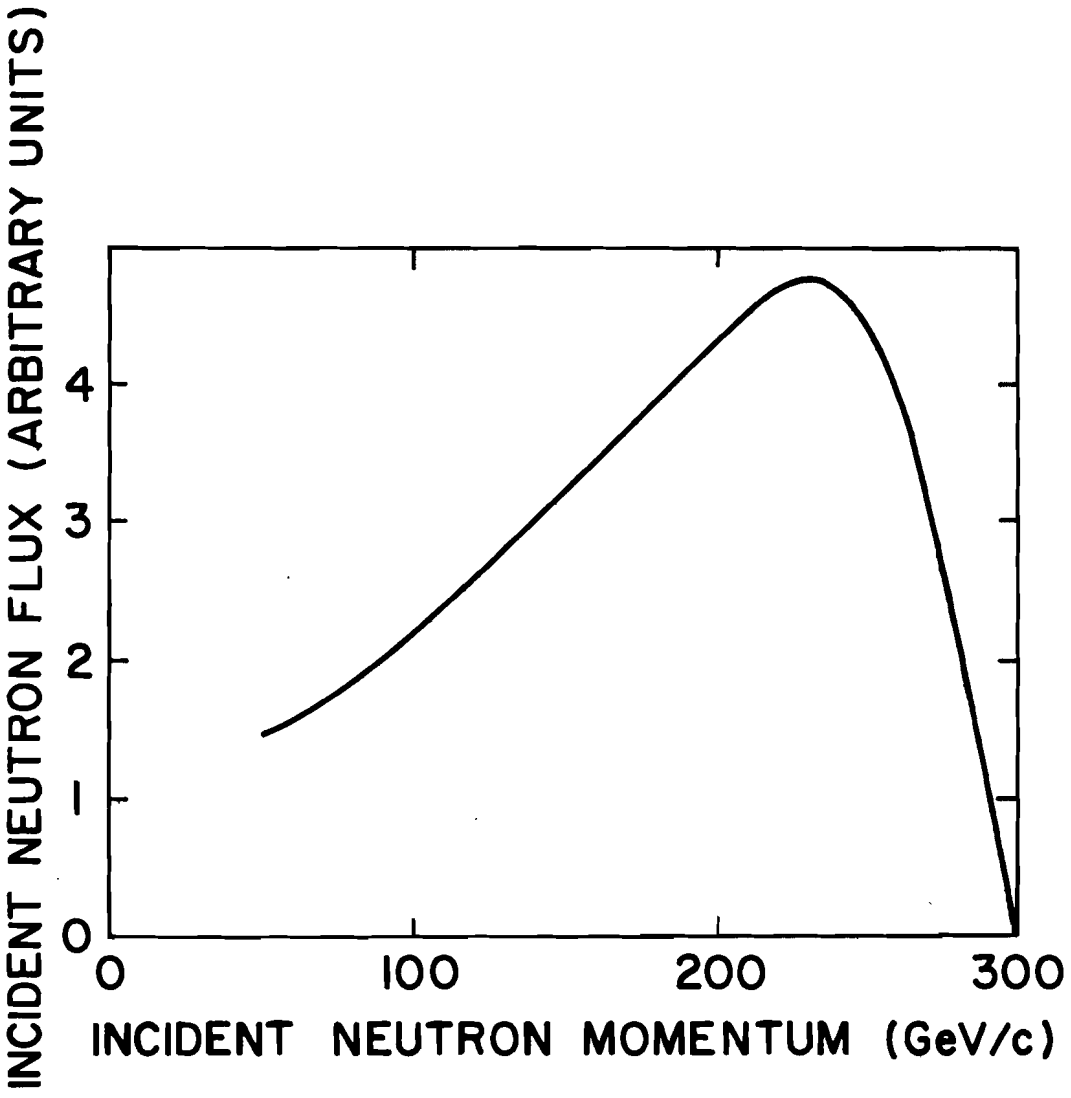
INCIDENT NEUTRON FLUX (ARBITRARY UNITS)
0
1
2
3
4
0
100
200
300
INCIDENT NEUTRON MOMENTUM (GeV/c)

Figure A.1